Distribution Category:
LMFBR—Physics: Base
Technology (UC-79d)

ANL--83-1

DE83 011019

ANL-83-1

ARGONNE NATIONAL LABORATORY
9700 South Cass Avenue
Argonne, Illinois 60439

THE DIF3D NODAL NEUTRONICS OPTION FOR TWO- AND THREE-DIMENSIONAL DIFFUSION-THEORY CALCULATIONS IN HEXAGONAL GEOMETRY

by

R. D. Lawrence

Applied Physics Division

DISCLAIMER

March 1983

TABLE OF CONTENTS

TABLE OF CONTENTS (Cont'd)

TABLE OF CONTENTS (Cont'd)

LIST OF FIGURES

LIST OF TABLES

The DIF3D Nodal Neutronics Option for Two- and Three-Dimensional Diffusion Theory Calculations in Hexagonal Geometry

by

R. D. Lawrence

Applied Physics Division
Argonne National Laboratory
Argonne, Illinois 60439

ABSTRACT

A nodal method is developed for the solution of the neutron-diffusion equation in two- and three-dimensional hexagonal geometries. The nodal scheme has been incorporated as an option in the finite-difference diffusion-theory code DIF3D, and is intended for use in the analysis of current LMFBR designs. The nodal equations are derived using higher-order polynomial approximations to the spatial dependence of the flux within the hexagonal-z node. The final equations, which are cast in the form of inhomogeneous response-matrix equations for each energy group, involve spatial moments of the node-interior flux distribution plus surface-averaged partial currents across the faces of the node. These equations are solved using a conventional fission source iteration accelerated by coarse-mesh rebalance and asymptotic source extrapolation.

Numerical calculations for models of heterogeneous-core LMFBR designs have shown the accuracy of the nodal scheme to be superior to that of the DIF3D finite difference option with six triangular mesh cells per hexagonal fuel assembly. The higher-order axial approximation in the nodal scheme permits the use of an axial mesh which is at least four times coarser than a typical finite difference mesh. Particular improvement is seen in the average fluxes in the internal-blanket regions and in the computed values for k-effective, thus leading to more accurate predictions of internal-blanket burnups, breeding ratios, and burnup reactivity swings. This enhanced accuracy is obtained with a potential order-of-magnitude reduction in the computational cost of a three-dimensional calculation.

This report describes the mathematical development and numerical solution of the nodal equations, as well as the use of the nodal option and details concerning its programming structure. This latter information is intended to supplement the information provided in the separate documentation of the DIF3D code.

1. INTRODUCTION

The physics and safety analysis of current Liquid Metal Fast Breeder Reactor (LMFBR) designs requires the capability to compute accurate numerical solutions to the neutron diffusion equation in three-dimensional hexagonal-z geometry. These neutronics calculations are generally performed within the U.S. fast reactor program using either standard mesh-centered finite difference codes[1-3] or flux synthesis methods such as the single-channel flux synthesis code SYN3D (Ref. 4). Due to the large number of unknowns involved, these calculations can be very expensive, particularly for fuel management studies which require repeated solution of the diffusion equation.

At Argonne National Laboratory, depletion calculations using the burnup code REBUS-3 (Ref. 5) are performed routinely in support of ongoing fast reactor design and analysis activities. The depletion calculation in REBUS-3 requires average group fluxes for burnup zones (over which the cross sections are taken to be spatially constant) defined such that each zone is composed of at least one hexagonal fuel assembly with an axial zone dimension of approximately 15 cm. A standard finite difference neutronics calculation requires six triangular mesh cells per hexagonal fuel assembly and an axial mesh spacing of approximately 5 cm in order to reduce spatial truncation errors to an acceptable level. Since only the zone-averaged fluxes are required for the actual depletion calculation, it is clear that a significant reduction in the overall computational expense can be achieved by reducing the number of mesh-points used to approximate the flux in each burnup zone. Thus there exists a strong motivation to develop a diffusion theory method which will compute accurate fluxes and eigenvalues when applied on a mesh defined by the dimensions of the hexagonal fuel assemblies and the axial zone boundaries. It is with this objective in mind that the nodal neutronics module described in this report was developed. This coarse-mesh neutronics capability is presently available as an option in the finite difference diffusion-theory code DIF3D (Ref. 3), which was developed by the Applied Physics Division at Argonne National Laboratory. The nodal option can also be used to provide the neutronics solutions required by REBUS-3.

Nodal methods comprise a class of coarse-mesh numerical methods which have demonstrated considerable potential for the analysis of light water reactors in Cartesian geometry. Many of the earlier nodal schemes[6] involved empirical coupling parameters which were determined from the results of detailed fine-mesh calculations or from actual operating data. Nodal schemes[7] developed in the past eight years have, for the most part, eliminated the need for empirical constants by computing the inter-node coupling relationships using higher-order approximations to the diffusion equation. Thus, unlike the earlier ad-hoc methods, these more recent nodal schemes can be viewed as coarse-mesh approximations to the neutron diffusion equation, and can thus be expected to converge to the exact solution of the diffusion equation in the limit as the mesh spacing goes to zero.

The success of these Cartesian-geometry schemes has prompted the more recent development of analogous techniques[8-11] for fast reactor calculations in hexagonal geometry. The nodal method[10-11] described in this report is based on a response matrix formulation in which the principal unknowns are the surface-averaged partial currents across the nodal interfaces. The response matrix equation is derived using an extension to hexagonal geometry of the transverse integration procedure[7] widely used in the development of Cartesian-geometry nodal schemes. Numerical calculations for typical heterogeneous-core LMFBR designs have shown that the accuracy of the nodal scheme is superior to that of a standard (6 mesh cells per hexagon, 5 cm axial mesh) finite difference calculation, and that this improved accuracy is obtained with a potential order-of-magnitude reduction in the computational cost of a three-dimensional calculation.

This report consists of two parts. The first part describes the mathematical development and numerical solution of the nodal equations. Specifically, Sections 2 and 3 discuss the derivations of the nodal equations in two and three dimensions, respectively, Section 4 describes the iterative procedures used to solve these equations, and Section 5 provides some numerical comparisons between the nodal and finite difference options in DIF3D. The second part of this report is intended as a user's manual for the nodal option in DIF3D. Section 6 includes specific information of interest to users of the code, while Section 7 provides additional information concerning the programming structure of the nodal option. Since much of the information provided in the documentation[3] of the finite difference option in DIF3D is pertinent to the nodal option, Sections 6 and 7 discuss only those additional features which are unique to the nodal option.

2. DERIVATION OF THE NODAL EQUATIONS IN TWO DIMENSIONS

2.1 The Neutron Diffusion Equation

As stated in the introduction, the objective of this work is to develop a capability to compute accurate numerical solutions to the neutron diffusion equation on a mesh defined by the dimensions of the hexagonal fuel assemblies and the boundaries of the axial burnup regions. Consistent with the present methodology in the reactor burnup code REBUS-3 (Ref. 5), the cross sections are assumed to be independent of position within the hexagonal-z mesh cell (node). The multigroup neutron diffusion equation[12] for a homogeneous node V^k can then be written in the form

$$-\underline{\nabla}\cdot D_g^k\,\underline{\nabla}\phi_g^k(\underline{r}) + \Sigma_g^{r,k}\,\phi_g^k(\underline{r}) = Q_g^k(\underline{r}),\quad \underline{r}\in V^k,\quad g=1,\ldots,G, \tag{2.1}$$

where

$$Q_g^k(\underline{r}) \equiv \frac{1}{\lambda}\chi_g \sum_{g'=1}^{G} \nu\Sigma_{g'}^{f,k}\,\phi_{g'}^k(\underline{r}) + \sum_{g'\neq g} \Sigma_{gg'}^{s,k}\,\phi_{g'}^k(\underline{r}), \tag{2.2}$$

λ denotes an eigenvalue, and the remaining notation is standard.[12] Although only the eigenvalue problem is considered here, the application of the nodal scheme to fixed-source problems is straightforward*. Equation (2.1) is solved subject to the boundary conditions that the flux and surface-normal component of the net current be continuous across the nodal interfaces, i.e.

$$\phi_g^k(r_s) = \phi_g^{\ell}(r_s) \tag{2.3}$$

$$\hat{n}\cdot D_g^k\,\underline{\nabla}\phi_g^k(r_s) = \hat{n}\cdot D_g^{\ell}\,\underline{\nabla}\phi_g^{\ell}(r_s), \tag{2.4}$$

where r_s denotes the surface shared by adjacent nodes k and ℓ. Boundary conditions of the general form

$$a_g\,\phi_g^k(r_s) + 2b_g\,\hat{n}\cdot D_g^k\,\underline{\nabla}\phi_g^k(r_s) = 0,\qquad r_s\in S, \tag{2.5}$$

*The capability to solve fixed source problems has not been implemented in the DIF3D nodal option.

are specified on nodal surfaces which form part of the outer boundary S of the solution domain. Standard boundary conditions (e.g. zero flux, zero incoming partial current) are obtained via appropriate specification of the constants a_g and b_g in Eq. (2.5).

As will be shown in Section 3, the three-dimensional nodal scheme employs somewhat different approximations to the spatial dependence of the flux in the radial (hex-plane) and axial directions. Thus, for the sake of clarity, we consider only the two-dimensional derivation in this section, and then use these two-dimensional results in combination with the additional axial approximations to derive the full three-dimensional nodal scheme in Section 3.

2.2 The Nodal Balance Equation

The starting point in the derivation of the nodal scheme is the nodal balance equation obtained by integrating the diffusion equation [Eq. (2.1)] over a homogeneous node V^k. Using the orientation shown in Fig. 2.1, with the origin (in local coordinates) taken as the center of the hexagon, the k-th node is defined by

$$V^k: \quad (x,y) \; x\epsilon[-h/2,+h/2], \; y\epsilon[-y_s(x),+y_s(x)],$$

where

$$y_s(x) \equiv \frac{1}{\sqrt{3}} (h - x), \tag{2.6}$$

and h is the lattice pitch. As shown in Fig. 2.1, the u and v directions are defined as perpendicular to the two sets of opposite faces not perpendicular to the x-direction.

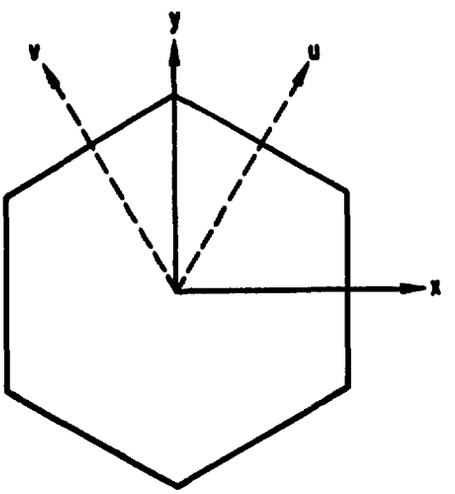

Fig. 2.1 Nodal Coordinate System

The nodal balance equation is obtained by operating on Eq. (2.1) with

$$\frac{1}{V^k} \int_{\underline{r}\epsilon V^k} d^3\underline{r}\ \cdot\ ,$$

where V^k is the volume of the hexagonal node, and then applying Gauss' theorem to the integrated leakage term:

$$\frac{1}{V^k} \int_{\underline{r}\epsilon V^k} d^3\underline{r}\ \underline{\nabla}\cdot D_g^k\ \underline{\nabla}\phi_g^k(\underline{r}) = \sum_{i=1}^{6} \frac{1}{V^k} \int_{\underline{r}_s \epsilon S_i^k} d^2\underline{r}_s\ \hat{n}_i \cdot D_g^k\ \underline{\nabla}\phi_g^k(r_s).$$

The summation shown here is over the six surfaces of the hexagonal node. Using the orientation shown in Fig. 2.1, the resulting balance equation can be written in the form

$$\frac{2h}{3}\left[\bar{L}_{gx}^k + \bar{L}_{gu}^k + \bar{L}_{gv}^k\right] + \Sigma_g^{r,k}\ \bar{\phi}_g^k = \bar{Q}_g^k, \tag{2.7}$$

where the node-averaged values of the flux and the multigroup source term are defined by

$$\bar{\phi}_g^k \equiv \frac{1}{V^k} \int_{-h/2}^{h/2} dx \int_{-y_s(x)}^{y_s(x)} dy\ \phi_g^k(x,y) \tag{2.8}$$

$$\bar{Q}_g^k \equiv \frac{1}{V^k} \int_{-h/2}^{h/2} dx \int_{-y_s(x)}^{y_s(x)} dy\ Q_g^k(x,y), \tag{2.9}$$

and

$$V^k \equiv \int_{-h/2}^{h/2} dx \int_{-y_s(x)}^{y_s(x)} dy$$

$$= \frac{\sqrt{3}}{2} h^2. \tag{2.10}$$

The terms $\bar{L}^k_{gx}$, $\bar{L}^k_{gu}$, and $\bar{L}^k_{gv}$ are average leakages in the three hex-plane directions, e.g.

$$\bar{L}^k_{gx} \equiv \bar{J}^k_{gx}(+h/2) - \bar{J}^k_{gx}(-h/2), \tag{2.11}$$

where $\bar{J}^k_{gx}(\pm h/2)$ are surface-averaged components of the net current in the x-direction:

$$\bar{J}^k_{gx}(\pm h/2) \equiv \left[\frac{1}{2y_s(x)} \int_{-y_s(x)}^{y_s(x)} dy \; -D^k_g \frac{\partial}{\partial x} \phi^k_g(x,y) \right]_{x=\pm h/2}. \tag{2.12}$$

The solution of Eq. (2.7) clearly requires additional relationships between the surface-averaged leakages and the nodal fluxes in the k-th node and its immediate neighbors. It is these additional relationships which characterize different nodal formulations. As a simple example, consider the standard mesh-centered finite difference equations which are derived under the assumption that the flux varies linearly from the center of the hexagon to the mid-points on any of the six surfaces. The resulting coupling relationships can be written in the form

$$\bar{J}^k_{gx}(h/2) = \gamma^{k,\ell}_{gx+} \bar{\phi}^k_g - \gamma^{\ell,k}_{gx-} \bar{\phi}^\ell_g, \tag{2.13}$$

where the coupling coefficients are

$$\gamma^{k,\ell}_{gx+} \equiv \gamma^{\ell,k}_{gx-} \equiv \frac{2}{h} \frac{D^k_g D^\ell_g}{D^k_g + D^\ell_g}. \tag{2.14}$$

Here, ℓ denotes the neighboring node in the positive x-direction such that the surface at $x = h/2$ is shared by nodes k and ℓ. Substitution of Eqs. (2.11) and (2.13) into Eq. (2.7) yields standard 7-point finite difference equations in two-dimensional hexagonal geometry. Thus the mesh-centered finite difference equations can be viewed as a simple nodal approximation in which coupling relationships of the form given in Eq. (2.13) are derived assuming a linear flux variation within the node.

The simple form of Eq. (2.13) and the resulting finite-difference-like form of the equations for the nodal fluxes suggest that Eq. (2.13) may provide an appropriate basis for more accurate approximations. Such improved approximations can be obtained by using higher-order polynomial approximations to the spatial variation of the flux within the node. Earlier unpublished work[13] along these lines resulted in a higher-order nodal formulation which utilizes coupling relationships of the form shown in Eq. (2.13). However, unlike Eq. (2.14), the expressions for the coupling coefficients involved ratios of surface-averaged fluxes to node-averaged fluxes as well as the higher-order coefficients of the polynomial approximation to the flux. This scheme thus requires non-linear updates of the coupling coefficients during the usual outer iteration procedure. Another potential drawback is that, unlike the finite difference matrix, the coefficient matrix obtained in the nodal scheme is not symmetric. This property, plus the need to update the coupling coefficients during the outer iteration procedure, raises additional questions concerning the applicability of the very efficient iterative solution methods[14] developed for finite difference equations to the nonlinear nodal equations. Furthermore, numerical studies[13] of the analogous slab geometry scheme demonstrated that convergence difficulties can arise if the coupling between the equations for the surface fluxes and higher order coefficients is not represented properly. Although this latter difficulty was eventually resolved, the uncertain iterative convergence behavior of the nonlinear scheme led to the development of an alternative formulation in which the inter-node leakages are calculated in terms of interface partial currents. This linear partial current scheme forms the basis of the DIF3D nodal option.

2.3 The Transverse Integration Procedure in Hexagonal Geometry

The equations for the partial currents required for the evaluation of the leakages in Eq. (2.7) are derived via an extension to hexagonal geometry of the transverse integration procedure[7] widely used in the development of Cartesian-geometry nodal schemes. In Cartesian geometry this technique involves spatially integrating the n-dimensional diffusion equation over the n-1 directions transverse to each coordinate direction. The resulting set of n coupled ordinary differential equations are approximated using techniques appropriate for the numerical solution of the one-dimensional diffusion equation. Additional approximations to the transverse leakage terms which couple the one-dimensional equations are also required.

Direct application of the analogous transverse integration procedure in hexagonal geometry yields three second-order ordinary differential equations in the x-, u-, and v-directions. However, a more straightforward procedure is to derive the P-1 forms of these equations using simple neutron balance arguments. For example, the one-dimensional equation in the x-direction is obtained by first introducing the partially-integrated quantities

$$\phi_{gx}^{k}(x) \equiv \int_{-y_s(x)}^{y_s(x)} dy\ \phi_g^k(x,y) \tag{2.15}$$

$$J_{gx}^{k}(x) \equiv \int_{-y_s(x)}^{y_s(x)} dy\ -D_g^k \frac{\partial}{\partial x} \phi_g^k(x,y) \tag{2.16}$$

$$Q_{gx}^{k}(x) \equiv \int_{-y_s(x)}^{y_s(x)} dy\ Q_g^k(x,y), \tag{2.17}$$

and then performing a simple neutron balance on the line defined by

$$\delta V^k: \quad (x,y) \quad x\varepsilon[x,x+dx], \quad y\varepsilon[-y_s(x),+y_s(x)], \quad x\neq 0.$$

The resulting balance equation can be written in the form

$$\frac{d}{dx} J_{gx}^{k}(x) + \Sigma_g^{r,k} \phi_{gx}^{k}(x) = Q_{gx}^{k}(x) - \frac{2}{\sqrt{3}} [J_g^k(x,y_s(x)) - J_g^k(x,-y_s(x))], \tag{2.18}$$

where $J_g^k(x,\pm y_s(x))$ are surface-normal components of the net current across the u- and v-directed surfaces:

$$J_g^k(x,+y_s(x)) \equiv -D_g^k\ \hat{n}_+ \cdot \underline{\nabla}\ \phi_g^k(x,y) \Big|_{y = y_s(x)} \tag{2.19a}$$

$$J_g^k(x,-y_s(x)) \equiv +D_g^k\ \hat{n}_- \cdot \underline{\nabla}\ \phi_g^k(x,y) \Big|_{y = -y_s(x)} . \tag{2.19b}$$

Here, $\hat{n}_{\pm}$ denotes unit vectors normal to the u- and v-directed surfaces

$$\hat{n}_{+} \equiv \begin{cases} \hat{n}_{v+} & -h/2 < x < 0 \\ \hat{n}_{u+} & 0 < x < h/2 \end{cases} \tag{2.20a}$$

$$\hat{n}_{-} \equiv \begin{cases} \hat{n}_{u-} & -h/2 < x < 0 \\ \hat{n}_{v-} & 0 < x < h/2 \end{cases} , \tag{2.20b}$$

where, for example, $\hat{n}_{u+}$ is the unit vector normal to the surface in the positive u-direction shown in Fig. 2.1. As shown in Section 2.5, integration of Eq. (2.18) over $x\varepsilon[-h/2, +h/2]$ yields the nodal balance equation, Eq. (2.7), as it should.

It is also convenient to introduce for later use the y-averaged quantities

$$\bar{\phi}^{k}_{gx}(x) \equiv \frac{1}{2y_s(x)} \int_{-y_s(x)}^{y_s(x)} dy\ \phi^{k}_{g}(x,y)$$

$$= \frac{1}{2y_s(x)}\ \phi^{k}_{gx}(x) \tag{2.21}$$

and

$$\bar{J}^{k}_{gx}(x) \equiv \frac{1}{2y_s(x)} \int_{-y_s(x)}^{y_s(x)} dy\ -D^{k}_{g}\ \frac{\partial}{\partial x}\ \phi^{k}_{g}(x,y)$$

$$= \frac{1}{2y_s(x)}\ J^{k}_{gx}(x). \tag{2.22}$$

Since Eq. (2.18) is written in P-1 form, we require an additional equation (analogous to Fick's Law) relating the partially-integrated flux $\phi^k_{gx}(x)$ and net current $J^k_{gx}(x)$. This relationship is obtained by applying Leibniz' rule for differentiating an integral with variable limits to Eq. (2.15):

$$-D^k_g \frac{d}{dx} \phi^k_{gx}(x) \equiv -D^k_g \frac{d}{dx} \int_{-y_s(x)}^{y_s(x)} dy\ \phi^k_g(x,y)$$

$$= -D^k_g \int_{-y_s(x)}^{y_s(x)} dy\ \frac{\partial}{\partial x} \phi^k_g(x,y)$$

$$- D^k_g\, y_s'(x)\, [\phi^k_g(x,y_s(x)) + \phi^k_g(x,-y_s(x))]. \qquad (2.24)$$

Since the first term on the right hand of this last equation is simply $J^k_{gx}(x)$, rearrangement yields

$$J^k_{gx}(x) = -D^k_g \frac{d}{dx} \phi^k_{gx}(x) + D^k_g\, y_s'(x)\, [\phi^k_g(x,y_s(x)) + \phi^k_g(x,-y_s(x))]. \qquad (2.25)$$

Similarly, the following relationship between $\bar{\phi}^k_{gx}(x)$ and $\bar{J}^k_{gx}(x)$ is obtained:

$$\bar{J}^k_{gx}(x) = -D^k_g \frac{d}{dx} \bar{\phi}^k_{gx}(x) + D^k_g \frac{y_s'(x)}{2y_s(x)} E^k_{gx}(x), \qquad (2.26)$$

where

$$E^k_{gx}(x) \equiv \phi^k_g(x,y_s(x)) + \phi^k_g(x,-y_s(x)) - 2\bar{\phi}^k_{gx}(x). \qquad (2.27)$$

The terms $\phi^k_g(x,\pm y_s(x))$ are fluxes evaluated on the u- and v-directed surfaces.

Equation (2.25) is similar to Fick's Law, but includes an additional term involving fluxes on the u- and v-directed surfaces. This additional term, which does not occur in Cartesian geometry, results from the variable integration limits inherent in hexagonal geometry. Differentiating Eq. (2.6) yields

$$y_s'(x) = -\frac{1}{\sqrt{3}} \operatorname{sgn}(x) \tag{2.28}$$

$$y_s''(x) = -\frac{2}{\sqrt{3}} \delta(x), \tag{2.29}$$

where $\delta(x)$ is the Dirac delta function. Since $y_s'(x)$ is discontinuous at x=0, the second term on the right hand side of Eq. (2.25) exhibits this same behavior. However, consistent with Eq. (2.4), the partially-integrated x-component of the net current must be continuous at x=0. Therefore, the partially-integrated flux must exhibit the following first-derivative discontinuity at x=0:

$$\lim_{\varepsilon \to 0} \left[-D_g^k \frac{d}{dx} \phi_{gx}^k(x)\right]_{x=-\varepsilon}^{x=\varepsilon} = \frac{2D_g^k}{\sqrt{3}} \left[\phi_g^k(x, y_s(x)) + \phi_g^k(x, -y_s(x))\right]_{x=0}. \tag{2.30a}$$

The y-averaged flux exhibits a similar discontinuity:

$$\lim_{\varepsilon \to 0} \left[-D_g^k \frac{d}{dx} \bar{\phi}_{gx}^k(x)\right]_{x=-\varepsilon}^{x=\varepsilon} = \frac{D_g^k}{h} E_{gx}^k(0). \tag{2.30b}$$

This behavior must be represented by any polynomial used to approximate the one-dimensional fluxes in hexagonal geometry.

The u- and v-direction counterparts to Eqs. (2.18) and (2.25) are derived in an analogous manner.

The approximation techniques developed in the following section are applied to the P-1 form of the one-dimensional equations given by Eqs. (2.18) and (2.25). However, in order to facilitate comparison with the usual second-order differential form of the one-dimensional Cartesian-geometry equations, it is convenient to cast Eqs. (2.18) and (2.25) in this same form. This result is obtained by substituting Eq. (2.25) into Eq. (2.18), and then using Eqs. (2.28) and (2.29):

$$-D_g^k \frac{d^2}{dx^2} \phi_{gx}^k(x) + \Sigma_g^{r,k} \phi_{gx}^k(x) = Q_{gx}^k(x) - S_{gx}^k(x), \tag{2.31}$$

where

$$S_{gx}^{k}(x) \equiv \frac{2}{\sqrt{3}} \left[J_g^k(x,y_s(x)) - J_g^k(x,-y_s(x))\right]$$

$$-\frac{D_g^k}{\sqrt{3}} \operatorname{sgn}(x) \left[\frac{d}{dx}\phi_g^k(x,y_s(x)) + \frac{d}{dx}\phi_g^k(x,-y_s(x))\right]$$

$$-\frac{2D_g^k}{\sqrt{3}} \delta(x) \left[\phi_g^k(x,y_s(x)) + \phi_g^k(x,-y_s(x))\right]. \qquad (2.32)$$

Although Eq. (2.31) is of the same general form as the Cartesian-geometry equations (i.e. a one-dimensional diffusion equation with a modified source term accounting for leakage in the transverse direction), the expression for the transverse-leakage term $S_{gx}^{k}(x)$ is considerably different. In particular, Eq. (2.32) includes two additional terms involving the Dirac delta function $\delta(x)$ as well the fluxes and their derivatives evaluated on the surfaces of the nodes. The impact of these additional terms on the choice of an approximation scheme is discussed in the following section.

2.4 Approximation of the One-Dimensional Hex-Plane Equations

2.4.1 On the Choice of a Method

A number of methods[15-20] have been developed for the approximate solution of Eq. (2.31) in Cartesian geometry. One possible classification of these methods is on the basis of whether information obtained from an analytic solution of the diffusion equation within the node is incorporated into the numerical scheme. In the first class, we include schemes in which the one-dimensional partially-integrated fluxes are approximated by a polynomial without the use of analytic information. Examples of these polynomial methods are the nodal expansion method[15] (NEM), the polynomial scheme developed by Sims,[16] and the NODLEG method due to Maeder.[17] Examples of the second class, the analytic methods, are the QUANDRY method,[18] the AN2D method,[19] and the nodal Green's function method[20] (NGFM).

The distinction between the polynomial and analytic approaches is particularly relevant to the solution of the transverse-integrated equations in hexagonal geometry. The QUANDRY and AN2D methods solve Eq. (2.31) (in Cartesian geometry) by first projecting $S_{gx}^{k}(x)$ onto a low-order polynomial, and then solving the resulting equation analytically. (The AN2D method also projects $Q_{gx}^{k}(x)$ onto a low-order polynomial). Hence the treatment of the delta function contribution in $S_{gx}^{k}(x)$ would appear to require rather extensive reformulations of these schemes. Since the NGFM

solves Eq. (2.31) via the use of a Green's function for the one-dimensional diffusion-removal operator on the left hand side of Eq. (2.31), the application of this scheme to the solution of Eq. (2.31) is relatively straightforward. Numerical results[18-20] have shown that the analytic methods are capable of very high accuracy when applied on a mesh corresponding to the dimensions of the (homogenized) fuel assemblies in a light water reactor (LWR). However, it should be noted that, measured in diffusion lengths, a typical LMFBR fuel element is smaller than a LWR fuel assembly; hence the high accuracy of the analytic methods may be unnecessary for the solution of Eq. (2.31) for LMFBR applications.

The expansion coefficients in the polynomial methods are calculated by requiring that the one-dimensional polynomial satisfy Eq. (2.31) in a weighted-integral sense. Thus the treatment of the delta function is straightforward, provided that the resulting first-derivative discontinuity in $\phi^k_{gx}(x)$ is represented properly by the approximating polynomial.

Since the high accuracy of the analytical methods is probably unnecessary for our application, and the delta function contribution is more easily accommodated by the polynomial methods, an approximation scheme based on a polynomial approach has been developed for the solution of the one-dimensional equations in hexagonal geometry. Although this scheme could be applied directly to Eq. (2.31), we choose instead to approximate the equivalent P-1 form [Eqs. (2.18) and (2.25)] since the resulting derivation is somewhat more straightforward.

2.4.2 The One-Dimensional Hex-Plane Polynomial Approximation

The polynomial approximation to the one-dimensional flux $\phi^k_{gx}(x)$ is given by

$$\phi^k_{gx}(x) \equiv \tilde{\phi}^k_{gx}(x) \equiv 2y_s(x)\,[\bar{\phi}^k_g + \sum_{n=1}^{N} a^k_{gxn}\, f_n(x)], \quad 2 \le N \le 4, \tag{2.33}$$

where

$$a^k_{gx1} \equiv \bar{\phi}^k_{gx}(+h/2) - \bar{\phi}^k_{gx}(-h/2) \tag{2.34a}$$

$$a^k_{gx2} \equiv \bar{\phi}^k_{gx}(+h/2) + \bar{\phi}^k_{gx}(-h/2) - 2\bar{\phi}^k_g \tag{2.34b}$$

$$f_1(x) \equiv \frac{x}{h} \equiv \xi \tag{2.35a}$$

$$f_2(x) \equiv \frac{36}{13}\xi^2 - \frac{5}{26} \tag{2.35b}$$

$$f_3(x) \equiv \frac{10}{13}\xi^2 - \frac{1}{2}|\xi| + \frac{3}{52} \tag{2.35c}$$

$$f_4(x) \equiv \xi(|\xi| - \tfrac{1}{2}). \tag{2.35d}$$

The polynomial approximation given in Eq. (2.33) is constructed such that the node-averaged flux $\bar{\phi}_g^k$ and the surface-averaged fluxes $\bar{\phi}_{gx}^k(\pm h/2)$ are preserved, i.e.

$$\frac{1}{V^k}\int_{-h/2}^{h/2} dx\, \tilde{\phi}_{gx}^k(x) \equiv \bar{\phi}_g^k \tag{2.37a}$$

$$\left[\frac{1}{2y_s(x)}\tilde{\phi}_{gx}^k(x)\right]_{x=\pm h/2} \equiv \bar{\phi}_{gx}^k(\pm h/2). \tag{2.37b}$$

Consistent with Eqs. (2.37), the basis functions defined in Eqs. (2.35) satisfy the constraints

$$\int_{-h/2}^{h/2} dx\, 2y_s(x)\, f_n(x) \equiv 0, \quad n=1,\ldots,4; \tag{2.38a}$$

$$f_n(\pm h/2) \equiv 0, \quad n=3,4. \tag{2.38b}$$

Note that Eq. (2.33), upon division by $2y_s(x)$, reduces for N=2 to a quadratic polynomial uniquely determined by the three constraints given in Eq. (2.37). This lowest-order approximation, which is equivalent to a quadratic approximation to the y-averaged one-dimensional flux defined in Eq. (2.21), is illustrated in Fig. 2.2.

Numerical studies[10] have shown that while the N=2 approximation is more accurate than the 1 point-per-hex finite difference approximation, the quadratic results are not as accurate as the standard 6 triangles-per-hex finite difference method. One reason for this relatively poor accuracy is that the N=2 approximation does not represent the first-derivative discontinuity [Eqs. (2.30)] at x=0. It can be shown that

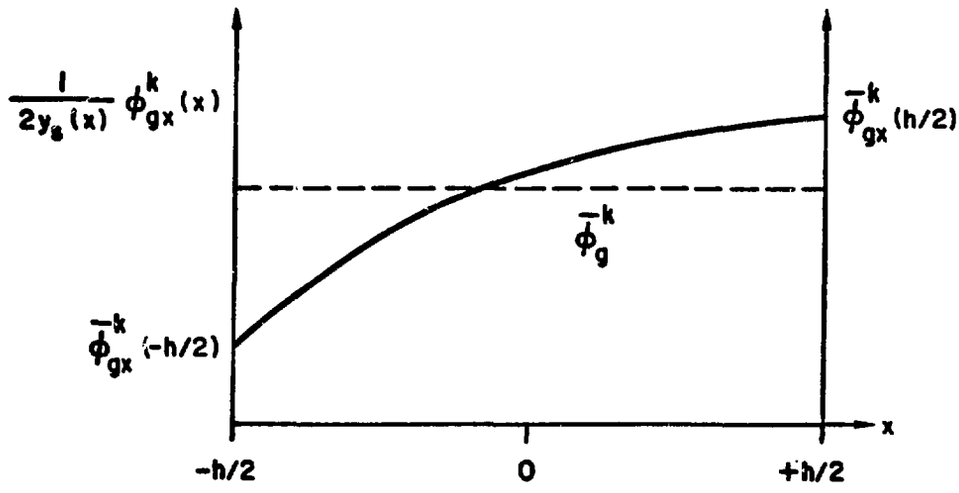

Fig. 2.2 Lowest-Order (Quadratic) Hex-Plane Polynomial Approximation

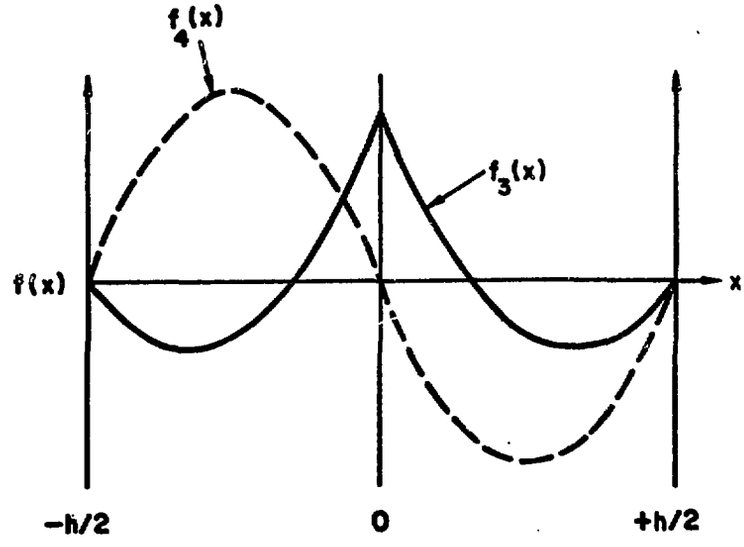

Fig. 2.3 Higher-Order Basis Functions in the Hex-Plane Polynomial Approximation

ignoring this behavior introduces an $O(h^2)$ error in the calculation; thus we should not expect the N=2 approximation to be significantly more accurate than the 1 point-per-hex finite difference scheme which also converges as $O(h^2)$. The higher-order basis functions $f_3(x)$ and $f_4(x)$ were thus added in order to provide an approximation to the first-derivative discontinuity, and to improve the overall accuracy of the nodal approximation. These basis functions are plotted in Fig. 2.3. From Fig. 2.3 it can be seen that $f_3(x)$ has a first-derivative discontinuity at x=0, and is thus intended to provide an approximation to the corresponding behavior in $\phi^k_{gx}(x)$. The basis function $f_4(x)$ provides a quadratic approximation within each of the half-intervals $x\varepsilon[-h/2,0]$ and $x\varepsilon[0,h/2]$, and thus offers improvement in the overall accuracy, provided that the expansion coefficient a^k_{gx4} is computed in an appropriate manner.

2.4.3 Calculation of the Expansion Coefficients a^k_{gx3}

The coefficient a^k_{gx3} in Eq. (2.33) is calculated by requiring that $\tilde{\phi}^k_{gx}(x)$ satisfy Eq. (2.30a), i.e.

$$\lim_{\varepsilon\to 0} \left[-D^k_g \frac{d}{dx} \tilde{\phi}^k_{gx}(x)\right]^{x=\varepsilon}_{x=-\varepsilon} \equiv \lim_{\varepsilon\to 0} \left[-D^k_g \frac{d}{dx} \phi^k_{gx}(x)\right]^{x=\varepsilon}_{x=-\varepsilon}$$

$$= \frac{2D^k_g}{\sqrt{3}} \left[\phi^k_g(x,y_s(x)) + \phi^k_g(x,-y_s(x))\right]_{x=0}. \tag{2.39}$$

This is equivalent to requiring that the partially-integrated net current $J^k_{gx}(x)$ be continuous at x=0. Differentiating Eq. (2.33) yields

$$\lim_{\varepsilon\to 0} \left[-D^k_g \frac{d}{dx} \tilde{\phi}^k_{gx}(x)\right]^{x=\varepsilon}_{x=-\varepsilon} = -D^k_g \left[2y_s(x)\, a^k_{gx3}\, f_3'(x) + \frac{2y_s'(x)}{2y_s(x)} \phi^k_{gx}(x)\right]^{x=\varepsilon}_{x=-\varepsilon}$$

$$= \frac{2D^k_g}{\sqrt{3}} \left[a^k_{gx3} + 2\, \bar{\phi}^k_{gx}(x)\right]_{x=0}, \tag{2.40}$$

where $\bar{\phi}^k_{gx}(x)$ is defined in Eq. (2.21). Substituting Eq. (2.40) into Eq. (2.39) and then solving for a^k_{gx3} yields

$$a^k_{gx3} \equiv E^k_{gx}(0), \tag{2.41}$$

where $E^k_{gx}(x)$ is defined in Eq. (2.27). Thus the calculation of a^k_{gx3} reduces to the development of an approximation to $E^k_{gx}(x)$.

At first glance, the approximation of $E^k_{gx}(x)$ does not appear straightforward due to its dependence upon the surface fluxes $\phi^k_g(x,\pm y_s(x))$. For example, $E^k_{gx}(0)$ involves the point fluxes at the intersections of the u- and v-directed surfaces in Fig. 2.1. However, we note that Eq. (2.27), upon division by $2y_s(x)$, is of the same form as the familiar finite difference approximation to the second derivative. This in turn suggests that $E^k_{gx}(x)$ can be related to the y-directed leakage defined by

$$f^k_{gy}(x) \equiv \frac{1}{2y_s(x)} \int_{-y_s(x)}^{y_s(x)} dy \; -D^k_g \frac{\partial^2}{\partial y^2} \phi^k_g(x,y)$$

$$= \frac{1}{2y_s(x)} \left[-D^k_g \frac{\partial}{\partial y} \phi^k_g(x,y) \right]_{y=-y_s(x)}^{y=y_s(x)}. \qquad (2.42)$$

Indeed, such a relationship does exist, and is given by

$$E^k_{gx}(x) = -\frac{1}{6D^k_g} [2y_s(x)]^2 f^k_{gy}(x) + O(h^4). \qquad (2.43)$$

This result, which is derived in Section A.1.1 of Appendix A, is particularly welcome since the approximation of the transverse leakage term $f^k_{gy}(x)$ is relatively straightforward.

A transverse leakage term analogous to Eq. (2.42) arises in the derivation of Cartesian-geometry nodal schemes. The simplest approximation to this term is to replace it by its average value over the node. In Cartesian geometry the average value of the y-directed leakage is given by the difference of the surface-averaged values of the net current on the two y-directed surfaces of the node. A more accurate (and thus more popular) approximation is obtained by replacing $f^k_{gy}(x)$ by a quadratic polynomial[15] written in terms of average leakages in the k-th node and its two immediate neighbors in the x-direction.

In hexagonal geometry, we replace $f^k_{gy}(x)$ by the "two-step" approximation

$$f^k_{gy}(x) \equiv \begin{cases} f^k_{gy-} & -h/2 < x < 0 \\ f^k_{gy+} & 0 < x < h/2 \end{cases}, \qquad (2.44)$$

where

$$f^k_{gy-} \equiv \frac{2}{V^k} \int_{-h/2}^{0} dx \int_{-y_s(x)}^{y_s(x)} dy \; -D^k_g \frac{\partial^2}{\partial y^2} \phi^k_g(x,y) \tag{2.45a}$$

$$f^k_{gy+} \equiv \frac{2}{V^k} \int_{0}^{h/2} dx \int_{-y_s(x)}^{y_s(x)} dy \; -D^k_g \frac{\partial^2}{\partial y^2} \phi^k_g(x,y). \tag{2.45b}$$

It is clear that f^k_{gy-} and f^k_{gy+} are simply average values of $f^k_{gy}(x)$ over the respective half-node intervals.

The half-node averages defined in Eqs. (2.45) are calculated in the following manner. Subtracting Eqs. (2.19) yields

$$J^k_g(x,y_s(x)) - J^k_g(x,-y_s(x)) = -D^k_g \left[\hat{n}_+ \cdot \underline{\nabla} \, \phi^k_g(x,y) \Big|_{y=y_s(x)} + \hat{n}_- \cdot \underline{\nabla} \, \phi^k_g(x,y) \Big|_{y=-y_s(x)} \right]. \tag{2.46}$$

Explicit evaluation of the $\hat{n} \cdot \underline{\nabla}$ terms yields

$$J^k_g(x,y_s(x)) - J^k_g(x,-y_s(x)) = -D^k_g \left\{ \frac{1}{2} \operatorname{sgn}(x) \left[\frac{\partial}{\partial x} \phi^k_g(x,y_s(x)) + \frac{\partial}{\partial x} \phi^k_g(x,-y_s(x)) \right] + \frac{\sqrt{3}}{2} \left[\frac{\partial}{\partial y} \phi^k_g(x,y) \right]_{y=-y_s(x)}^{y=y_s(x)} \right\}. \tag{2.47}$$

The total and partial derivatives are related by

$$\frac{d}{dx} \phi^k_g(x,\pm y_s(x)) = \frac{\partial}{\partial x} \phi^k_g(x,\pm y_s(x)) \pm y_s'(x) \frac{\partial}{\partial y} \phi^k_g(x,y) \Big|_{y=\pm y_s(x)}. \tag{2.48}$$

Substituting Eq. (2.48) into Eq. (2.47), and then using Eq. (2.28) yields

$$J_g^k(x,y_s(x)) - J_g^k(x,-y_s(x)) = -D_g^k \left\{ \frac{1}{2} \operatorname{sgn}(x) \left[\frac{d}{dx} \phi_g^k(x,y_s(x)) \right. \right.$$

$$\left. \left. + \frac{d}{dx} \phi_g^k(x,-y_s(x)) \right] + \frac{2}{\sqrt{3}} \left[\frac{\partial}{\partial y} \phi_g^k(x,y) \right]_{y=-y_s(x)}^{y=y_s(x)} \right\}. \qquad (2.49)$$

With reference to Fig. 2.1, we note that

$$\frac{2}{h} \int_{-h/2}^{0} dx \, [J_g^k(x,y_s(x)) - J_g^k(x,-y_s(x))] \equiv \bar{J}_{gv}^k(h/2) - \bar{J}_{gu}^k(-h/2) \qquad (2.50a)$$

$$\frac{2}{h} \int_{0}^{h/2} dx \, [J_g^k(x,y_s(x)) - J_g^k(x,-y_s(x))] \equiv \bar{J}_{gu}^k(+h/2) - \bar{J}_{gv}^k(-h/2), \qquad (2.50b)$$

where $\bar{J}_{gu}^k(\pm h/2)$ and $\bar{J}_{gv}^k(\pm h/2)$, the surface-averaged net currents across the u- and v-directed surfaces, are defined in analogy with Eq. (2.12). Performing the y-integration in Eqs. (2.45) yields

$$\int_{-h/2}^{0} dx \left[-D_g^k \frac{\partial}{\partial y} \phi_g^k(x,y) \right]_{y=-y_s(x)}^{y=y_s(x)} = \frac{1}{2} V^k \mathfrak{f}_{gy-}^k \qquad (2.51a)$$

$$\int_{0}^{h/2} dx \left[-D_g^k \frac{\partial}{\partial y} \phi_g^k(x,y) \right]_{y=-y_s(x)}^{y=y_s(x)} = \frac{1}{2} V^k \mathfrak{f}_{gy+}^k . \qquad (2.51b)$$

An equation for $\mathfrak{f}_{gy+}^k$ is obtained by substituting Eq. (2.49) into Eq. (2.50b), and then using Eq. (2.51b) to eliminate the final term in Eq. (2.49) in favor of $\mathfrak{f}_{gy+}^k$. An analogous procedure is used to obtain an equation for $\mathfrak{f}_{gy-}^k$. These results, plus details of the derivations, are given in Section A.1.2 of Appendix A.

With these results in hand, the final equation for the expansion coefficient a^k_{gx3} can now be derived. This final stage of the derivation proceeds as follows:

$$a^k_{gx3} = E^k_{gx}(0) \qquad \{\text{from Eq. (2.41)}\}$$

$$\cong \frac{1}{2}\left[E^k_{gx}(0^-) + E^k_{gx}(0^+)\right]$$

$$\cong -\frac{1}{12D^k_g}\left[2y_s(0)\right]^2\left[\mathfrak{L}^k_{gy-} + \mathfrak{L}^k_{gy+}\right] \qquad \{\text{using Eq. (2.43)}\}$$

$$= -\frac{h^2}{9D^k_g}\left[\mathfrak{L}^k_{gy-} + \mathfrak{L}^k_{gy+}\right]. \qquad (2.52)$$

Note that $E^k_{gx}(0)$ is obtained by averaging the values on either side of x=0 since $E^k_{gx}(x)$ is not continuous at x=0. [This is due to the two-step approximation of $\mathfrak{L}^k_{gy}(x)$ given by Eq. (2.44)]. The $O(h^4)$ term in Eq. (2.43) has been neglected, but this error is clearly small compared to that introduced by the two-step leakage approximation. As shown in Section A.1.3 of Appendix A, Eq. (2.52) leads to the following final form of the equation for a^k_{gx3}:

$$a^k_{gx3} = -\frac{26}{189}\frac{h}{D^k_g}\left[\bar{L}^k_{gu} + \bar{L}^k_{gv}\right] - \frac{8}{21}\left[\bar{\phi}^k_{gx}(+h/2) + \bar{\phi}^k_{gx}(-h/2) - 2\bar{\phi}^k_g\right]. \qquad (2.53)$$

As will be shown in Section 2.6, the fluxes and leakages on the right hand side of Eq. (2.53) are eliminated in favor of interface partial currents and spatial moments of the intra-node group source distribution. Thus the coefficient a^k_{gx3} does not appear in the final form of the nodal equations.

2.4.4 Calculation of the Expansion Coefficient a^k_{gx4}

The expansion coefficient a^k_{gx4} is calculated using a weighted residual (WR) approximation to the one-dimensional balance equation, Eq. (2.18). The WR equation is obtained by weighting Eq. (2.18)

with weight function w(x), and then requiring the result to be zero when integrated over the interval x ε[-h/2,+h/2], i.e.

$$\langle w(x), \frac{d}{dx} J^k_{gx}(x) + \Sigma^{r,k}_g \phi^k_{gx}(x) - Q^k_{gx}(x)$$

$$+ \frac{2}{\sqrt{3}} [J^k_g(x,y_s(x)) - J^k_g(x,-y_s(x))] \rangle \equiv 0, \tag{2.54}$$

where the inner product is defined by

$$\langle w(x), \phi^k_{gx}(x) \rangle \equiv \frac{1}{V^k} \int_{-h/2}^{h/2} dx\, w(x)\, \phi^k_{gx}(x).$$

Using Eqs. (2.50), it can be shown that unit weighting, i.e.

$$w(x) \equiv w_0(x) \equiv 1, \tag{2.55}$$

reduces Eq. (2.53) to the nodal balance equation, Eq. (2.7). Since the nodal balance equation insures a neutron balance over the hexagonal node, a logical choice for an additional weight function $w_1(x)$ is such that a neutron balance is preserved over each of the three pairs of <u>half-nodes</u> in the three hex-plane directions x, u, and v. This is accomplished in the x-direction by specifying

$$w(x) \equiv w_1(x) \equiv \mathrm{sgn}(x) \tag{2.56}$$

in Eq. (2.54). That this procedure is equivalent to preserving a neutron balance over each half-node can be verified by first writing Eq. (2.54) explicitly for $w(x) \equiv w_0(x)$ and $w(x) \equiv w_1(x)$,

$$\langle w_0(x), \ldots \rangle \equiv \frac{1}{V^k} \left[\int_{-h/2}^{0} dx \ldots + \int_{0}^{h/2} dx \ldots \right] \equiv 0$$

$$\langle w_1(x), \ldots \rangle \equiv \frac{1}{V^k} \left[-\int_{-h/2}^{0} dx \ldots + \int_{0}^{h/2} dx \ldots \right] \equiv 0,$$

and then separately adding and subtracting these results to obtain the half-node balance equations

$$\frac{2}{V^k} \int_{-h/2}^{0} dx \ \ldots \equiv 0 \tag{2.57a}$$

$$\frac{2}{V^k} \int_{0}^{h/2} dx \ \ldots \equiv 0. \tag{2.57b}$$

An analogous weighted residual procedure, applied to the u- and v-direction analogs of Eq. (2.54), insures a neutron balance over each of the half-nodes in the u- and v-directions.

An equation for a^k_{gx4} is derived by requiring the one-dimensional polynomial approximation [Eq. (2.33)] to $\phi^k_{gx}(x)$ satisfy Eq. (2.54) with w(x) given by Eq. (2.56). Introducing the x-direction spatial moment,

$$\phi^k_{gx1} \equiv \langle w_1(x), \phi^k_{gx}(x) \rangle$$

$$\equiv \frac{1}{V^k} \int_{-h/2}^{h/2} dx \ \mathrm{sgn}(x) \ \phi^k_{gx}(x) \tag{2.58a}$$

$$\equiv \frac{1}{V^k} \int_{-h/2}^{h/2} dx \ \mathrm{sgn}(x) \int_{-y_s(x)}^{y_s(x)} dy \ \phi^k_g(x,y), \tag{2.58b}$$

and then substituting Eq. (2.33) into Eq. (2.58a) and performing the necessary integrations yields

$$\phi^k_{gx1} = \frac{2}{9} a^k_{gx1} - \frac{1}{24} a^k_{gx4}, \tag{2.59a}$$

or, using Eq. (2.33a),

$$a^k_{gx4} = -24\ \phi^k_{gx1} + \frac{16}{3}\left[\bar{\phi}^k_{gx}(+h/2) - \bar{\phi}^k_{gx}(-h/2)\right]. \qquad (2.59b)$$

Using this result, a^k_{gx4} can be eliminated in favor of the flux moment ϕ^k_{gx1} which, along with the nodal flux $\bar{\phi}^k_g$ and the u- and v-direction moments ϕ^k_{gu1} and ϕ^k_{gv1}, comprise the flux moments which appear in the final form of the nodal equations. Equations for the flux moments are derived in Section 2.5.

2.4.5 Overview of the Approximation Procedure

It is appropriate at this point to provide a brief overview of the approximation procedure developed in this section. The partially-integrated flux is approximated by the polynomial given in Eq. (2.33). In its simplest form this approximation reduces to a quadratic polynomial derived such that the node-averaged flux and the two surface-averaged fluxes in the x-direction are preserved. [This quadratic approximation is analogous to the lowest-order approximation used in the Cartesian-geometry Nodal Expansion Method[15] (NEM)]. Higher-order approximations are obtained by first adding a basis function $f_3(x)$ which has a first derivative discontinuity at x=0, and then adding an additional basis function $f_4(x)$ which provides a quadratic approximation over the half-intervals $-h/2 < x < 0$ and $0 < x < h/2$. The coefficient of $f_3(x)$ is determined by requiring the y-integrated net current to be continuous at x=0, while the coefficient of $f_4(x)$ is calculated by applying a weighted residual procedure to the one-dimensional balance equation. This latter procedure is equivalent to enforcing a neutron balance over each of the half-nodes. The calculation of the coefficient a^k_{gx3} also requires an approximation [Eq. (2.44)] to the transverse-leakage term $\bar{\ell}^k_{gy}(x)$ introduced in Eq. (2.42).

The approximations introduced in this section can also be viewed in a more general context. The surface-averaged fluxes and leakages are eventually eliminated in favor of surface-averaged partial currents in the derivation of the response matrix equation given in Section 2.6. The partial currents are required during the global solution procedure to be continuous across the nodal interfaces. This is equivalent to requiring that the surface integrals of the flux and the surface-normal component of the net current be continuous across the interface. Furthermore, the nodal balance equation (which is obtained by integrating the diffusion equation over a node) insures a neutron balance over the hexagonal node. Thus the following constraints are satisfied over the hexagon: (i) node-integrated neutron balance, (ii) continuity of the surface-integrated flux, and (iii) continuity of the surface-integrated surface-normal component of the net current. These constraints, which are satisfied by both the quadratic and the higher-order approximations, are equivalent to requiring that Eqs. (2.1), (2.3), and (2.4) be satisfied in an integral sense. As discussed in the preceeding paragraph, the higher-order expansion coefficients are calculated such that the partially-integrated net current is continuous across the interface shared by the two half-nodes and

such that a neutron balance is preserved over each half-node. Since the partially-integrated flux is continuous across the half-node interface (Eq. (2.33) is continuous at x=0), the above constraints are also satisfied over each pair of half-nodes in the three hex-plane directions. In other words, if the hexagon is divided into six equilateral triangles (by drawing connecting lines between the three pairs of opposite vertices), the three constraints are satisfied over the six regions defined by the union of two adjacent triangles sharing a common surface. (It should be noted, however, that these constraints are not necessarily satisfied over each of the six triangles). Thus, in summary, the approximations introduced in this section result in the diffusion equation [Eq. (2.1)] and the usual continuity conditions [Eqs. (2.3) and (2.4)] being satisfied in an integral sense over each of the three pairs of half-hexagons as well as over the hexagonal node itself.

2.5 The Flux Moments Equations

The flux moments equations are derived from Eq. (2.54), which we write in the form

$$\langle w_n(x), \frac{d}{dx} J^k_{gx}(x)\rangle + \Sigma^{r,k}_g \phi^k_{gxn} = Q^k_{gxn}$$

$$- \langle w_n(x), \frac{2}{\sqrt{3}} [J^k_g(x,y_s(x)) - J^k_g(x,-y_s(x))]\rangle, \quad n=0,1, \qquad (2.60)$$

where

$$\phi^k_{gx0} \equiv \bar{\phi}^k_g$$

$$Q^k_{gx0} \equiv \bar{Q}^k_g,$$

and $w_0(x)$, $w_1(x)$, and ϕ^k_{gx1} are defined by Eqs. (2.55), (2.56), and (2.58), respectively. Integrating the first term in Eq. (2.60) by parts yields

$$\langle w_n(x), \frac{d}{dx} J^k_{gx}(x)\rangle = \frac{2}{3h} [w_n(h/2)\ \bar{J}^k_{gx}(h/2) - w_n(-h/2)\ \bar{J}^k_{gx}(-h/2)]$$

$$+ \frac{4}{3h} \bar{J}^k_{gx}(0)\ [w_n(0^+) - w_n(0^-)]. \qquad (2.61)$$

Substitution of Eqs. (2.55) and (2.56) into this result yields

$$\langle w_0(x), \frac{d}{dx} J^k_{gx}(x)\rangle = \frac{2h}{3} \bar{L}^k_{gx} \tag{2.62}$$

and

$$\langle w_1(x), \frac{d}{dx} J^k_{gx}(x)\rangle = \frac{2h}{3} \bar{T}^k_{gx} - \frac{8}{3h} \bar{J}^k_{gx}(0), \tag{2.63}$$

respectively, where $\bar{L}^k_{gx}$ is the x-directed leakage defined in Eq. (2.11), i.e.

$$\bar{L}^k_{gx} \equiv \bar{J}^k_{gx}(+h/2) - \bar{J}^k_{gx}(-h/2), \tag{2.11}$$

and

$$\bar{T}^k_{gx} \equiv \bar{J}^k_{gx}(+h/2) + \bar{J}^k_{gx}(-h/2). \tag{2.64}$$

Using Eqs. (2.50), the last term in Eq. (2.60) can be written for n=0,1 as

$$\begin{aligned}
&\langle w_0(x), \frac{2}{\sqrt{3}} [J^k_g(x,y_s(x)) - J^k_g(x,-y_s(x))]\rangle \\
&\quad = \frac{2}{3h} [\bar{J}^k_{gv}(+h/2) - \bar{J}^k_{gu}(-h/2) + \bar{J}^k_{gu}(+h/2) - \bar{J}^k_{gv}(-h/2)] \\
&\quad = \frac{2}{3h} [\bar{L}^k_{gu} + \bar{L}^k_{gv}],
\end{aligned} \tag{2.65}$$

and

$$\begin{aligned}
&\langle w_1(x), \frac{2}{\sqrt{3}} [J^k_g(x,y_s(x)) - J^k_g(x,-y_s(x))] \\
&\quad = \frac{2}{3h} [- \bar{J}^k_{gv}(+h/2) + \bar{J}^k_{gu}(-h/2) + \bar{J}^k_{gu}(+h/2) - \bar{J}^k_{gv}(-h/2)] \\
&\quad = \frac{2}{3h} [\bar{T}^k_{gu} - \bar{T}^k_{gv}].
\end{aligned} \tag{2.66}$$

Substitution of Eqs. (2.62) and (2.65) into Eq. (2.60) (written for n=0) yields

$$\Sigma_g^{r,k}\ \bar{\phi}_g^k = \bar{Q}_g^k - \frac{2}{3h}\ [\bar{L}_{gx}^k + \bar{L}_{gu}^k + \bar{L}_{gv}^k]. \tag{2.67}$$

Thus, as mentioned previously, unit weighting of the one-dimensional balance equation yields the nodal balance equation given in Eq. (2.7). Substitution of Eqs. (2.63) and (2.66) into Eq. (2.60) (written for n=1) yields

$$\Sigma_g^{r,k}\ \phi_{gx1}^k = Q_{gx1}^k - \frac{2}{3h}\ [\bar{T}_{gx}^k + \bar{T}_{gu}^k - \bar{T}_{gv}^k] + \frac{8}{3h}\ \bar{J}_{gx}^k(0). \tag{2.68}$$

Evaluation of the final term in Eq. (2.68) requires Eq. (2.26), which we repeat here

$$\bar{J}_{gx}^k(x) = -D_g^k\ \frac{d}{dx}\ \bar{\phi}_{gx}^k(x) + D_g^k\ \frac{y_s'(x)}{2y_s(x)}\ E_{gx}^k(x). \tag{2.26}$$

Using Eq. (2.33) to approximate $\bar{\phi}_{gx}^k(x)$ yields

$$\bar{J}_{gx}^k(0) = \frac{-D_g^k}{h}\ [a_{gx1}^k + \frac{72}{13}\ a_{gx2}^k\ \xi + a_{gx3}^k\ (\frac{20}{13}\ \xi - \frac{1}{2})$$

$$+ a_{gx4}^k\ (2\xi - \frac{1}{2})]_{\xi=0} - \frac{1}{2}\ \frac{D_g^k}{h}\ E_{gx}^k(0)$$

$$= \frac{-D_g^k}{h}\ [a_{gx1}^k - \frac{1}{2}\ a_{gx3}^k - \frac{1}{2}\ a_{gx4}^k + \frac{1}{2}\ E_{gx}^k(0)]$$

$$= \frac{-D_g^k}{h}\ [a_{gx1}^k - \frac{1}{2}\ a_{gx4}^k] \qquad \{\text{using Eq. (2.41)}\}$$

$$= \frac{D_g^k}{h}\ [\frac{5}{3}\ a_{gx1}^k - 12\ \phi_{gx1}^k]. \qquad \{\text{using Eq. (2.59a)}\} \tag{2.69}$$

Substitution of Eq. (2.69) into Eq. (2.68) yields

$$[\Sigma_g^{r,k} + \frac{32}{h}\frac{D_g^k}{h}]\,\phi_{gx1}^k = Q_{gx1}^k - \frac{2}{3h}\,[\bar{T}_{gx}^k + \bar{T}_{gu}^k - \bar{T}_{gv}^k] + \frac{40}{9h}\frac{D_g^k}{h}\,a_{gx1}^k. \tag{2.70}$$

The u- and v-direction analogs of Eq. (2.70) are readily derived via the transformations:

$$\begin{aligned} &\text{u-direction:} \quad x\to u,\ u\to v,\ v\to -x \\ &\text{v-direction:} \quad x\to v,\ u\to -x,\ v\to -u. \end{aligned} \tag{2.71}$$

The resulting equations can be combined with Eq. (2.70) to yield

$$\begin{bmatrix} \phi_{gx1}^k \\ \phi_{gu1}^k \\ \phi_{gv1}^k \end{bmatrix} = \frac{h}{\alpha_{g1}^k}\begin{bmatrix} Q_{gx1}^k \\ Q_{gu1}^k \\ Q_{gv1}^k \end{bmatrix} - \frac{2}{3\alpha_{g1}^k}\begin{bmatrix} 1 & 1 & -1 \\ 1 & 1 & 1 \\ -1 & 1 & 1 \end{bmatrix}\begin{bmatrix} \bar{T}_{gx}^k \\ \bar{T}_{gu}^k \\ \bar{T}_{gv}^k \end{bmatrix}$$

$$+ \frac{40}{9\alpha_{g1}^k}\frac{D_g^k}{h}\begin{bmatrix} a_{gx1}^k \\ a_{gu1}^k \\ a_{gv1}^k \end{bmatrix}, \tag{2.72}$$

where

$$\alpha_{g1}^k \equiv h\Sigma_g^{r,k} + 32\,\frac{D_g^k}{h}. \tag{2.73}$$

Rewriting Eq. (2.67) yields

$$\bar{\phi}_g^k = \frac{h}{h\Sigma_g^{r,k}} \bar{Q}_g^k - \frac{2}{3h\Sigma_g^{r,k}} [\bar{L}_{gx}^k + \bar{L}_{gu}^k + \bar{L}_{gv}^k]. \tag{2.74}$$

Equations (2.72) and (2.74) are used to evaluate the flux moments $\bar{\phi}_g^k$, ϕ_{gxl}^k, ϕ_{gul}^k, and ϕ_{gvl}^k, which, along with the surface-averaged partial currents introduced in the following section, form the principal unknowns of the nodal scheme.

2.6 The Response Matrix Equation

In this section the approximations introduced in Section 2.4 are used to derive the local response matrix equation which forms the cornerstone of the DIF3D nodal scheme. This equation relates the six outgoing surface-averaged partial currents for a single energy group to the six incoming partial currents for the same node and the spatial moments of the intra-node group source distribution. The outgoing and incoming surface-averaged partial currents across the x-directed faces shown in Fig. 2.1 are defined by

$$\bar{J}_{gx}^{out,k}(\pm h/2) \equiv \left[\frac{1}{2y_s(x)} \int_{-y_s(x)}^{y_s(x)} dy \left\{\frac{1}{4} \phi_g^k(x,y) \mp \frac{1}{2} D_g^k \frac{\partial}{\partial x} \phi_g^k(x,y)\right\}\right]_{x=\pm h/2} \tag{2.75a}$$

$$\bar{J}_{gx}^{in,k}(\pm h/2) \equiv \left[\frac{1}{2y_s(x)} \int_{-y_s(x)}^{y_s(x)} dy \left\{\frac{1}{4} \phi_g^k(x,y) \pm \frac{1}{2} D_g^k \frac{\partial}{\partial x} \phi_g^k(x,y)\right\}\right]_{x=\pm h/2} \tag{2.75b}$$

The partial currents across the u- and v-directed faces are defined in an analogous manner. The approximations developed in Section 2.4 involved both surface-averaged fluxes and net currents. These quantities are eliminated in favor of the partial currents using the simple relationships

$$\bar{\phi}_{gx}^k(\pm h/2) = 2[J_{gx}^{out,k}(\pm h/2) + \bar{J}_{gx}^{in,k}(\pm h/2)] \tag{2.76}$$

$$\bar{J}_{gx}^k(+h/2) = \bar{J}_{gx}^{out,k}(+h/2) - \bar{J}_{gx}^{in,k}(+h/2) \tag{2.77a}$$

$$\bar{\phi}_g^k = \frac{h}{h\Sigma_g^{r,k}} \bar{Q}_g^k - \frac{2}{3h\Sigma_g^{r,k}} [\bar{L}_{gx}^k + \bar{L}_{gu}^k + \bar{L}_{gv}^k]. \tag{2.74}$$

Equations (2.72) and (2.74) are used to evaluate the flux moments $\bar{\phi}_g^k$, ϕ_{gxl}^k, ϕ_{gul}^k, and ϕ_{gvl}^k, which, along with the surface-averaged partial currents introduced in the following section, form the principal unknowns of the nodal scheme.

2.6 The Response Matrix Equation

In this section the approximations introduced in Section 2.4 are used to derive the local response matrix equation which forms the cornerstone of the DIF3D nodal scheme. This equation relates the six outgoing surface-averaged partial currents for a single energy group to the six incoming partial currents for the same node and the spatial moments of the intra-node group source distribution. The outgoing and incoming surface-averaged partial currents across the x-directed faces shown in Fig. 2.1 are defined by

$$\bar{J}_{gx}^{out,k}(\pm h/2) \equiv \left[\frac{1}{2y_s(x)} \int_{-y_s(x)}^{y_s(x)} dy \left\{\frac{1}{4} \phi_g^k(x,y) \mp \frac{1}{2} D_g^k \frac{\partial}{\partial x} \phi_g^k(x,y)\right\}\right]_{x=\pm h/2} \tag{2.75a}$$

$$\bar{J}_{gx}^{in,k}(\pm h/2) \equiv \left[\frac{1}{2y_s(x)} \int_{-y_s(x)}^{y_s(x)} dy \left\{\frac{1}{4} \phi_g^k(x,y) \pm \frac{1}{2} D_g^k \frac{\partial}{\partial x} \phi_g^k(x,y)\right\}\right]_{x=\pm h/2} \tag{2.75b}$$

The partial currents across the u- and v-directed faces are defined in an analogous manner. The approximations developed in Section 2.4 involved both surface-averaged fluxes and net currents. These quantities are eliminated in favor of the partial currents using the simple relationships

$$\bar{\phi}_{gx}^k(\pm h/2) = 2[J_{gx}^{out,k}(\pm h/2) + \bar{J}_{gx}^{in,k}(\pm h/2)] \tag{2.76}$$

$$\bar{J}_{gx}^k(+h/2) = \bar{J}_{gx}^{out,k}(+h/2) - \bar{J}_{gx}^{in,k}(+h/2) \tag{2.77a}$$

$$\bar{J}^{k}_{gx}(-h/2) = \bar{J}^{in,k}_{gx}(-h/2) - \bar{J}^{out,k}_{gx}(-h/2). \qquad (2.77b)$$

These relationships are derived by separately adding and subtracting Eqs. (2.75), and then recalling the definitions of $\bar{\phi}^{k}_{gx}(x)$ and $\bar{J}^{k}_{gx}(x)$ given in Eqs. (2.21) and (2.22).

An equation for $\bar{J}^{out,k}_{gx}(+h/2)$ is derived using Eqs. (2.77a) and (2.26):

$$\bar{J}^{out,k}_{gx}(+h/2) = \bar{J}^{k}_{gx}(+h/2) + \bar{J}^{in,k}_{gx}(+h/2)$$

$$= [-D^{k}_{g} \frac{d}{dx} \bar{\phi}^{k}_{gx}(x) + D^{k}_{g} \frac{y'_{s}(x)}{2y_{s}(x)} E^{k}_{gx}(x)]_{x=h/2} + \bar{J}^{in,k}_{gx}(+h/2)$$

$$= [-D^{k}_{g} \frac{d}{dx} \phi^{k}_{gx}(x)]_{x=h/2} - \frac{D^{k}_{g}}{h} E^{k}_{gx}(h/2) + \bar{J}^{in,k}_{g}(+h/2). \qquad (2.78)$$

The first term on the right hand side of Eq. (2.78) is approximated using the polynomial approximation given in Eq. (2.33):

$$[-D^{k}_{g} \frac{d}{dx} \bar{\phi}^{k}_{gx}(x)]_{x=h/2} \cong -D^{k}_{g} \frac{d}{dx} [\bar{\phi}^{k}_{g} + \sum_{n=1}^{N} a^{k}_{gxn} f_{n}(x)]_{x=h/2}$$

$$= \frac{-D^{k}_{g}}{h} [a^{k}_{gx1} + \frac{36}{13} a^{k}_{gx2} + \frac{7}{26} a^{k}_{gx3} + \frac{1}{2} a^{k}_{gx4}]. \qquad (2.79)$$

Substitution of Eq. (2.79) into Eq. (2.78) yields

$$\bar{J}^{out,k}_{gx}(+h/2) = \frac{-D^{k}_{g}}{h} [a^{k}_{gx1} + \frac{36}{13} a^{k}_{gx2} + \frac{7}{26} a^{k}_{gx3} + \frac{1}{2} a^{k}_{gx4} + E^{k}_{gx}(h/2)]$$

$$+ \bar{J}^{in,k}_{gx}(+h/2). \qquad (2.80)$$

Since the remaining steps in the derivation of the response matrix equation involve a considerable amount of algebraic manipulation, these steps are simply outlined here with additional details provided in Section A.3 of Appendix A. The remaining steps are as follows:

(1) The expansion coefficients a^k_{gx1}, a^k_{gx2}, a^k_{gx3}, and a^k_{gx4} are eliminated from Eq. (2.80) using Eqs. (2.34a), (2.34b), (2.53), and (2.59b), respectively. The term $E^k_{gx}(h/2)$ is eliminated using Eqs. (2.43) and (2.44).

(2) The flux moments $\bar{\phi}^k_g$ and ϕ^k_{gx1} introduced via step (1) are eliminated in favor of the source moments $\bar{Q}^k_g$ and Q^k_{gx1} using Eqs. (2.74) and (2.70), respectively.

(3) All surfaced-averaged fluxes and net currents introduced via steps (1) and (2) are eliminated in favor of surface-averaged partial currents using Eqs. (2.76) and (2.77). The result, which involves outgoing and incoming partial currents on the six surfaces, plus the source moments $\bar{Q}^k_g$ and $\bar{Q}^k_{gx1}$, can be written in the form

$$[a_1\ a_2\ a_3\ a_4\ a_3\ a_2]\ \underline{J}_g^{out,k} = [b_1\ b_2] \begin{bmatrix} \bar{Q}^k_g \\ Q^k_{gx1} \end{bmatrix}$$

$$+ [c_1\ c_2\ c_3\ c_4\ c_3\ c_2]\ \underline{J}_g^{in,k}\ , \qquad (2.81)$$

where $\underline{J}_g^{out,k}$ and $\underline{J}_g^{in,k}$ are column vectors containing the six outgoing and six incoming partial currents, respectively, for the k-th node, e.g.

$$\underline{J}_g^{out,k} \equiv \text{col}\ [\bar{J}^{out,k}_{gx}(+h/2),\ \bar{J}^{out,k}_{gu}(+h/2),\ \bar{J}^{out,k}_{gv}(+h/2),\ \bar{J}^{out,k}_{gx}(-h/2),$$

$$\bar{J}^{out,k}_{gu}(-h/2),\ \bar{J}^{out,k}_{gv}(-h/2)]. \qquad (2.82)$$

The constants a_i, b_i, and c_i are given in Appendix A.

(4) Five additional equations similar to Eq. (2.81) can be obtained by applying steps (1) through (3) to Eq. (2.80) written for the remaining 5 surfaces of the hexagonal node. These equations can also be obtained by applying successive 60° rotational transformations to Eq. (2.81). Note

that the u- and v-direction analogs of Eq. (2.81) involve Q^k_{gu1} and Q^k_{gv1}, respectively. These additional equations can be combined with Eq. (2.81) to yield

$$[A^k_g]\ \underline{J}^{out,k}_g = [B^k_g]\ \underline{Q}^k_g + [C^k_g]\ \underline{J}^{in,k}_g\ , \tag{2.83}$$

where

$$\underline{Q}^k_g \equiv \text{col}\ [\bar{Q}^k_g,\ Q^k_{gx1},\ Q^k_{gu1},\ Q^k_{gv1}]. \tag{2.84}$$

The structure of the matrices introduced in Eq. (2.83) is discussed in Appendix A.

(5) The final form of the response matrix equation is obtained by inverting $[A^k_g]$ in Eq. (2.83) to yield

$$\underline{J}^{out,k}_g = [P^k_g]\ \underline{Q}^k_g + [R^k_g]\ \underline{J}^{in,k}_g\ , \tag{2.85}$$

where $[P^k_g]$ is a 6 by 4 source matrix and $[R^k_g]$ is a 6 by 6 response matrix.

Equation (2.85) is an inhomogeneous local response matrix equation written for the k-th node and g-th energy group. The energy groups are coupled via the source term $\underline{Q}^k_g$, which is calculated [as in Eq. (2.2)] in terms of the flux moments:

$$Q^k_g = \frac{1}{\lambda}\,\chi_g \sum_{g'=1}^{G} \nu\Sigma^{f,k}_{g'}\ \underline{\phi}^k_{g'} + \sum_{g'\neq g} \Sigma^{s,k}_{gg'}\ \underline{\phi}^k_{g'}\ , \tag{2.86}$$

where

$$\underline{\phi}^k_g = \text{col}\ [\bar{\phi}^k_g,\ \phi^k_{gx1},\ \phi^k_{gu1},\ \phi^k_{gv1}]. \tag{2.87}$$

Since Eq. (2.85) is written for a single energy group, the calculation of the matrices $[P_g^k]$ and $[R_g^k]$ in multigroup problems is straightforward. In two dimensions, $[P_g^k]$ and $[R_g^k]$ contain 3 and 4 unique entries, respectively, per energy group. Another important property of Eq. (2.85) is that the source and response matrices depend only on the material properties (specifically the diffusion coefficient and the removal cross section) of the k-th node. Thus the unique entries of these matrices need be computed prior to the outer iterations and stored only for unique nodes characterized by their material composition assignment.

2.7 Boundary Conditions

The nodes are coupled by requiring the surface-averaged partial currents to be continuous across the nodal interfaces. This is accomplished by using the computed outgoing partial currents as incoming partial currents to the respective neighboring nodes, i.e.

$$\bar{J}_{gx}^{in,k}(+h/2) \equiv \bar{J}_{gx}^{out,\ell}(-h/2) \tag{2.88a}$$

$$\bar{J}_{gx}^{in,\ell}(-h/2) \equiv \bar{J}_{gx}^{out,k}(+h/2), \tag{2.88b}$$

where k and ℓ are neighboring nodes sharing the surface denoted (in local coordinates) by x=h/2 in the k-th node and x=-h/2 in the ℓ-th node. Equations (2.88) are equivalent (in an integral sense) to Eqs. (2.3) and (2.4), i.e. Eqs. (2.88) insure continuity of the surface-averaged values of the flux and surface-normal component of the net current across the nodal interfaces.

The incoming partial currents on nodal surfaces which form part of the outer boundary of the solution domain are computed in terms of the outgoing partial current on the same surface, e.g.

$$\bar{J}_{gx}^{in,k}(+h/2) = \gamma_g \, \bar{J}_{gx}^{out,k}(+h/2). \tag{2.89}$$

Recalling the general form [Eq. (2.5)] of the boundary condition,

$$a_g \, \phi_g^k(r_s) + 2b_g \, \hat{n} \cdot D_g^k \, \underline{\nabla} \, \phi_g^k(r_s) = 0, \tag{2.5}$$

the coefficient γ_g is given by

$$\gamma_g = \frac{b_g - a_g}{b_g + a_g}, \qquad b_g \neq -a_g. \tag{2.90}$$

The standard boundary conditions are specified as follows:

$$\gamma_g = \begin{cases} -1 & \text{zero flux boundary condition} \\ 0 & \text{zero incoming partial current boundary conditions} \\ +1 & \text{zero net current (reflective) boundary condition.} \end{cases} \tag{2.91}$$

Periodic (i.e. rotational symmetry) boundary conditions in the hex-plane are treated by using the computed outgoing partial currents across a boundary as an incoming partial current across the corresponding periodic boundary.

2.8 Summary

The two-dimensional nodal scheme derived in this section involves a total of 10 principal unknowns per node per group: 6 surface-averaged outgoing partial currents and 4 spatial moments of the intra-node flux distribution. The partial currents are calculated from the response matrix equation, Eq. (2.85), while the flux moments are computed using Eqs. (2.72) and (2.74). The required source moments are obtained from Eq. (2.86). Since all terms (other than the source terms) on the right hand side of Eqs. (2.72) and (2.74) can be evaluated in terms of the partial currents, and the incoming partial currents are simply outgoing partial currents from neighboring nodes, these results represent 10 equations for the 10 principal unknowns. The iterative solution of these equations is discussed in Section 4.

3. DERIVATION OF THE NODAL EQUATIONS IN THREE DIMENSIONS

The three-dimensional nodal scheme derived in this section employs a transverse integration procedure to reduce the three-dimensional diffusion equation to four coupled one-dimensional equations, three in the hex-plane and one in the axial direction. The hex-plane equations are approximated as described in Section 2.4, while a more conventional cubic polynomial approximation is applied to the axial equation. The hex-plane and axial approximations are then combined to form a response matrix equation similar to that derived previously in two dimensions.

3.1 The Nodal Balance Equation

The nodal balance equation is obtained by integrating the diffusion equation over a homogeneous three-dimensional node V^k defined by

$$V^k: \quad (x,y,z)\ x\varepsilon[-h/2,+h/2],\ y\varepsilon[-y_s(x),+y_s(x)],\ z\varepsilon[-\Delta z^k/2,+\Delta z^k/2],$$

where Δz^k is the axial mesh spacing and, as before, h is the lattice pitch and $y_s(x)$ is defined in Eq. (2.6). Recall that the origin (in local coordinates) is taken as the center of the three-dimensional node. Operating on Eq. (2.1) with

$$\frac{1}{V^k} \int_{\underline{r}\varepsilon V^k} d^3\underline{r}\ \cdot \quad ,$$

where V^k is the volume of the hexagonal-z node, and then applying Gauss' theorem as in the two-dimensional development yields the three-dimensional nodal balance equation

$$\frac{2}{3h}\left[\bar{L}^k_{gx} + \bar{L}^k_{gu} + \bar{L}^k_{gv}\right] + \frac{1}{\Delta z^k}\bar{L}^k_{gz} + \Sigma^{r,k}_g\,\bar{\phi}^k_g = \bar{Q}^k_g. \tag{3.1}$$

The node-averaged values of the flux and multigroup source term are defined by

$$\bar{\phi}^k_g \equiv \frac{1}{V^k}\int_{-\Delta z^k/2}^{\Delta z^k/2} dz \int_{-h/2}^{h/2} dx \int_{-y_s(x)}^{y_s(x)} dy\ \phi^k_g(x,y,z) \tag{3.2}$$

$$\bar{Q}_g^k \equiv \frac{1}{V^k} \int_{-\Delta z^k/2}^{\Delta z^k/2} dz \int_{-h/2}^{h/2} dx \int_{-y_s(x)}^{y_s(x)} dy\ Q_g^k(x,y,z), \tag{3.3}$$

where

$$V^k \equiv \int_{-\Delta z^k/2}^{\Delta z^k/2} dz \int_{-h/2}^{h/2} dx \int_{-y_s(x)}^{y_s(x)} dy$$

$$= \frac{\sqrt{3}}{2} h^2\ \Delta z^k. \tag{3.4}$$

The terms $\bar{L}_{gx}^k$, $\bar{L}_{gu}^k$, $\bar{L}_{gv}^k$, and $\bar{L}_{gz}^k$ are leakages in the three hex-plane directions (recall Fig. 2.1) and the axial direction, e.g.

$$\bar{L}_{gx}^k \equiv \bar{J}_{gx}^k(+h/2) - \bar{J}_{gx}^k(-h/2) \tag{3.5}$$

$$\bar{L}_{gz}^k \equiv \bar{J}_{gz}^k(+\Delta z^k/2) - \bar{J}_{gz}^k(-\Delta z^k/2), \tag{3.6}$$

where $\bar{J}_{gx}^k(\pm h/2)$ and $\bar{J}_{gz}^k(\pm \Delta z^k/2)$ are face-averaged surface-normal components of the net current on the x- and z-directed faces:

$$\bar{J}_{gx}^k(\pm h/2) \equiv \left[\frac{1}{\Delta z^k} \int_{-\Delta z^k/2}^{\Delta z^k/2} dz\ \frac{1}{2y_s(x)} \int_{-y_s(x)}^{y_s(x)} dy\ -D_g^k \frac{\partial}{\partial x} \phi_g^k(x,y,z) \right]_{x=\pm h/2} \tag{3.7}$$

$$\bar{J}_{gz}^k(\pm \Delta z^k/2) \equiv \frac{\Delta z^k}{V^k} \int_{-h/2}^{h/2} dx \int_{-y_s(x)}^{y_s(x)} dy\ -D_g^k \frac{\partial}{\partial z} \phi_g^k(x,y,z) \Big|_{z=\pm \Delta z^k/2}. \tag{3.8}$$

3.2 The Transverse Integration Procedure in Three Dimensions

The transverse integration procedure discussed in Section 2.3 can be used to reduce the three-dimensional diffusion equation to two coupled equations, a two-dimensional equation in the hex-plane and a one-dimensional equation in the axial direction. The hex-plane equation can then be further reduced (as in Section 2.3) to three coupled one-dimensional equations in the three hex-plane directions. However, consistent with our approach in two dimensions, the one-dimensional hex-plane equations are derived in a single step by first introducing the partially-integrated quantities

$$\phi_{gx}^{k}(x) \equiv \int_{-\Delta z^{k}/2}^{\Delta z^{k}/2} dz \int_{-y_s(x)}^{y_s(x)} dy\ \phi_g^k(x,y,z) \tag{3.9}$$

$$J_{gx}^{k}(x) \equiv \int_{-\Delta z^{k}/2}^{\Delta z^{k}/2} dz \int_{-y_s(x)}^{y_s(x)} dy\ -D_g^k \frac{\partial}{\partial x} \phi_g^k(x,y,z) \tag{3.10}$$

$$Q_{gx}^{k}(x) \equiv \int_{-\Delta z^{k}/2}^{\Delta z^{k}/2} dz \int_{-y_s(x)}^{y_s(x)} dy\ Q_g^k(x,y,z), \tag{3.11}$$

and then performing a neutron balance on the slice (perpendicular to the x-direction) defined by

$$\delta V^k\colon\ (x,y,z)\ x\varepsilon[x,x+dx],\ y\varepsilon[-y_s(x),+y_s(x)],\ z\varepsilon[-\Delta z^k/2,+\Delta z^k/2].$$

The balance equation takes the form

$$\frac{d}{dx} J^k_{gx}(x) + \Sigma^{r,k}_g \phi^k_{gx}(x) = Q^k_{gx}(x)$$

$$-\frac{2}{\sqrt{3}} [J^k_{gxy}(x,y_s(x)) - J^k_{gxy}(x,-y_s(x))] - \int_{-y_s(x)}^{y_s(x)} dy\ L^k_{gz}(x,y), \qquad (3.12)$$

where $J^k_{gxy}(x,\pm y_s(x))$ are z-integrated, surface-normal components of the net current across the u- and v-directed surfaces:

$$J^k_{gxy}(x,y_s(x)) \equiv \int_{-\Delta z^k/2}^{\Delta z^k/2} dz\ -D^k_g\ \hat{n}_+ \cdot \underline{\nabla}\ \phi^k_g(x,y,z) \Big|_{y=y_s(x)} \qquad (3.13a)$$

$$J^k_{gxy}(x,-y_s(x)) \equiv \int_{-\Delta z^k/2}^{\Delta z^k/2} dz\ +D^k_g\ \hat{n}_- \cdot \underline{\nabla}\ \phi^k_g(x,y,z) \Big|_{y=-y_s(x)}, \qquad (3.13b)$$

and the unit vectors $\hat{n}_\pm$ are defined in Eqs. (2.20). The final term in Eq. (3.12) involves the axial leakage defined by

$$L^k_{gz}(x,y) \equiv \int_{-\Delta z^k/2}^{\Delta z^k/2} dz\ -D^k_g \frac{\partial^2}{\partial z^2} \phi^k_g(x,y,z)$$

$$\equiv -D^k_g \frac{\partial}{\partial z} \phi^k_g(x,y,z)\Big|_{z=-\Delta z^k/2}^{z=\Delta z^k/2} . \qquad (3.14)$$

Note that

$$\bar{L}^k_{gz} \equiv \frac{\Delta z^k}{V^k} \int_{-h/2}^{h/2} dx \int_{-y_s(x)}^{y_s(x)} dy\ L^k_{gz}(x,y), \qquad (3.15)$$

where $\bar{L}^k_{gz}$ is defined in Eq. (3.6).

Equation (3.12) is very similar to the one-dimensional balance equation [Eq. (2.18)] obtained in Section 2.3, with an additional term accounting for leakage in the axial direction. As in Eq. (2.25), the partially-integrated net current and flux are related by

$$J^k_{gx}(x) \equiv -D^k_g \frac{d}{dx} \phi^k_{gx}(x) + D^k_g \, y'_s(x) \, [\phi^k_{gxy}(x,y_s(x)) + \phi^k_{gxy}(x,-y_s(x))], \qquad (3.16)$$

where

$$\phi^k_{gxy}(x,y) \equiv \int_{-\Delta z^k/2}^{\Delta z^k/2} dz \; \phi^k_g(x,y,z). \qquad (3.17)$$

The one-dimensional axial equation can be obtained by either operating on the three-dimensional diffusion equation with

$$\int_{-h/2}^{h/2} dx \int_{-y_s(x)}^{y_s(x)} dy \cdot ,$$

or by performing a neutron balance on

$$\delta V^k: \quad (x,y,z) \; x\varepsilon[-h/2,+h/2], \; y\varepsilon[-y_s(x),+y_s(x)], \; z\varepsilon[z,z+dz].$$

The result is

$$\frac{d}{dz} J^k_{gz}(z) + \Sigma^{r,k}_g \phi^k_{gz}(z) = Q^k_{gz}(z) - L^k_{gxy}(z), \qquad (3.18)$$

where, analogous to Eqs. (3.9) - (3.11),

$$\phi_{gz}^{k}(z) \equiv \int_{-h/2}^{h/2} dx \int_{-y_s(x)}^{y_s(x)} dy\ \phi_g^k(x,y,z) \tag{3.19}$$

$$J_{gz}^{k}(z) \equiv \int_{-h/2}^{h/2} dx \int_{-y_s(x)}^{y_s(x)} dy\ -D_g^k \frac{\partial}{\partial z} \phi_g^k(x,y,z) \tag{3.20}$$

$$Q_{gz}^{k}(z) \equiv \int_{-h/2}^{h/2} dx \int_{-y_s(x)}^{y_s(x)} dy\ Q_g^k(x,y,z). \tag{3.21}$$

The partially-integrated hex-plane leakage $L_{gxy}^{k}(z)$ is given by

$$L_{gxy}^{k}(z) \equiv \int_{-h/2}^{h/2} dx \int_{-y_s(x)}^{y_s(x)} dy\ -D_g^k \left[\frac{\partial^2}{\partial x^2} + \frac{\partial^2}{\partial y^2}\right] \phi_g^k(x,y,z). \tag{3.22}$$

The total hex-plane leakage is

$$\bar{L}_{gxy}^{k} \equiv \frac{3h}{2} \frac{1}{V^k} \int_{-\Delta z^k/2}^{\Delta z^k/2} dz\ L_{gxy}^{k}(z), \tag{3.23}$$

which can be written in terms of the average leakages in the three hex-plane directions,

$$\bar{L}_{gxy}^{k} \equiv \bar{L}_{gx}^{k} + \bar{L}_{gu}^{k} + \bar{L}_{gv}^{k}. \tag{3.24}$$

We also introduce the hex-plane averaged quantities

$$\bar{\phi}^k_{gz}(z) \equiv \frac{\Delta z^k}{V^k} \phi^k_{gz}(z)$$

$$\equiv \frac{\Delta z^k}{V^k} \int_{-h/2}^{h/2} dx \int_{-y_s(x)}^{y_s(x)} dy\ \phi^k_g(x,y,z) \tag{3.25}$$

$$\bar{J}^k_{gz}(z) \equiv \frac{\Delta z^k}{V^k} J^k_{gz}(z)$$

$$\equiv \frac{\Delta z^k}{V^k} \int_{-h/2}^{h/2} dx \int_{-y_s(x)}^{y_s(x)} dy\ -D^k_g \frac{\partial}{\partial z} \phi^k_g(x,y,z). \tag{3.26}$$

Since Eq. (3.18) is in P-1 form, it is necessary (once again) to specify a relationship between the partially-integrated net current and flux. However, since the integration limits in Eq. (3.19) do not depend upon z, this relationship between $J^k_{gz}(z)$ and $\phi^k_{gz}(z)$ is particularly simple:

$$J^k_{gz}(z) = -D^k_g \frac{d}{dz} \phi^k_{gz}(z). \tag{3.27}$$

Similarly,

$$\bar{J}^k_{gz}(z) = -D^k_g \frac{d}{dz} \bar{\phi}^k_{gz}(z). \tag{3.28}$$

The one-dimensional hex-plane equations [Eqs. (3.12) and (3.16)] are approximated as described in Section 2.4. Thus we now turn to the development of an approximation scheme for the one-dimensional axial equations [Eqs. (3.18) and (3.27)].

3.3 Approximation of the One-Dimensional Axial Equations

3.3.1 The One-Dimensional Axial Polynomial Approximation

The one-dimensional axial flux is approximated as follows:

$$\phi_{gz}^{k}(z) \equiv \tilde{\phi}_{gz}^{k}(z) \equiv \frac{V^{k}}{\Delta z^{k}} \left[\bar{\phi}_{g}^{k} + \sum_{n=1}^{N_z} a_{gzn}^{k} f_{zn}(z)\right], \quad 2 \leq N_z \leq 3, \tag{3.29}$$

where

$$a_{gz1}^{k} \equiv \bar{\phi}_{gz}^{k}(+\Delta z^{k}/2) - \bar{\phi}_{gz}^{k}(-\Delta z^{k}/2) \tag{3.30a}$$

$$a_{gz2}^{k} \equiv \bar{\phi}_{gz}^{k}(+\Delta z^{k}/2) + \bar{\phi}_{gz}^{k}(-\Delta z^{k}/2) - 2\bar{\phi}_{g}^{k} \tag{3.30b}$$

$$f_{z1}(z) \equiv \frac{z}{\Delta z^{k}} \equiv \xi \tag{3.31a}$$

$$f_{z2}(z) \equiv 3\xi^{2} - \frac{1}{4} \tag{3.31b}$$

$$f_{z3}(z) \equiv \xi(\xi - \tfrac{1}{2})(\xi + \tfrac{1}{2}). \tag{3.31c}$$

As in the hex-plane approximation, the axial approximation is constructed such that the node-averaged flux $\bar{\phi}_{g}^{k}$ and the surface-averaged fluxes $\bar{\phi}_{gz}^{k}(\pm\Delta z^{k}/2)$ are preserved, i.e.

$$\frac{1}{V^{k}} \int_{-\Delta z^{k}/2}^{\Delta z^{k}/2} dz\, \tilde{\phi}_{gz}^{k}(z) \equiv \bar{\phi}_{g}^{k} \tag{3.32a}$$

$$\left[\frac{\Delta z^k}{v^k}\,\tilde{\phi}^k_{gz}(z)\right]_{z=\pm\Delta z^k/2} \equiv \bar{\phi}^k_{gz}(\pm\Delta z^k/2). \tag{3.32b}$$

Consistent with Eqs. (3.32), the basis functions defined in Eqs. (3.31) satisfy the constraints

$$\int_{-\Delta z^k/2}^{\Delta z^k/2} dz\, f_{zn}(z) \equiv 0, \qquad n = 1,2,3, \tag{3.33a}$$

$$f_{z3}(\pm\Delta z^k/2) \equiv 0. \tag{3.33b}$$

Comparison of Eqs. (3.16) and (3.27) shows that unlike the one-dimensional hex-plane fluxes, the axial flux $\phi^k_{gz}(z)$ does not exhibit a first-derivative discontinuity. Thus the basis function $f_{z3}(z)$ is a simple cubic polynomial subject only to the constraints given in Eqs. (3.33).

Equation (3.29) is equivalent to the polynomial used to approximate the one-dimensional fluxes in the Cartesian-geometry nodal expansion method[15] (NEM). The NEM formulation however differs from the Cartesian-geometry analog of the method developed here in that the NEM equations are not cast in the multidimensional response matrix form shown in Eq. (2.85). Although NEM calculations for light water reactors (LWR) typically use a fourth-order polynomial expansion [i.e. $N_z \equiv 4$ in Eq. (3.29)], only a third-order (cubic) polynomial is used to approximate the one-dimensional axial flux here. This choice is based on the observation that while LWR nodes are often 10 diffusion lengths in dimension, the 15 to 20 cm axial burnup regions typical of fast reactor calculations are equivalent to axial node dimensions of only 3 to 4 diffusion lengths.

3.3.2 Calculation of the Expansion Coefficient a^k_{gz3}

The expansion coefficient a^k_{gz3} is calculated by applying a weighted residual approximation to the axial balance equation, Eq. (3.18). As in Section 2.4.4, we weight the one-dimensional balance equation with weight function $w(z)$, and then require the result to be zero when integrated over the interval $z\varepsilon[-\Delta z^k/2,+\Delta z^k/2]$, i.e.

$$\langle w(z),\, \frac{d}{dz} J^k_{gz}(z) + \Sigma^{r,k}_g\, \phi^k_{gz}(z) - Q^k_{gz}(z) + L^k_{gxy}(z)\rangle \equiv 0, \tag{3.34}$$

where the inner product is defined by

$$\langle w(z),\ \phi_{gz}^{k}(z)\rangle \equiv \frac{1}{V^{k}} \int_{-\Delta z^{k}/2}^{\Delta z^{k}/2} dz\ w(z)\ \phi_{gz}^{k}(z).$$

As before, it can be shown that unit weighting, i.e.

$$w(z) \equiv w_{0}(z) \equiv 1,$$

reduces Eq. (3.34) to the three-dimensional nodal balance equation, Eq. (3.1).

Several choices of weight functions are possible for the calculation of a_{gz3}^{k}. These choices include "half-node" weighting such as that used in the hex-plane approximation, i.e.

$$w(z) \equiv w_{z1}(z) \equiv \mathrm{sgn}(z), \tag{3.35a}$$

moments weighting,

$$w(z) \equiv w_{z1}(z) \equiv \frac{z}{\Delta z^{k}} \equiv f_{z1}(z), \tag{3.35b}$$

and Galerkin weighting,

$$w(z) \equiv w_{z1}(z) \equiv f_{z3}(z). \tag{3.35c}$$

Numerical comparisons[15] using the nodal expansion method have shown moments weighting to be more accurate than Galerkin weighting. Similar studies[13] during the early stages of the present work support this conclusion. Additional slab-geometry results have further demonstrated that moments weighting is slightly more accurate than half-node weighting. Thus Eq. (3.34), with weight function $w_{z1}(z)$ defined in Eq. (3.35b), is used to calculate a_{gz3}^{k}.

The axial spatial moment is thus defined by

$$\phi^k_{gz1} \equiv \langle w_{z1}(z),\ \phi^k_{gz}(z)\rangle$$

$$\equiv \frac{1}{V^k} \int_{-\Delta z^k/2}^{\Delta z^k/2} dz\ \frac{z}{\Delta z^k}\ \phi^k_{gz}(z) \tag{3.36a}$$

$$\equiv \frac{1}{V^k} \int_{-\Delta z^k/2}^{\Delta z^k/2} dz\ \frac{z}{\Delta z^k} \int_{-h/2}^{h/2} dx \int_{-y_s(x)}^{y_s(x)} dy\ \phi^k_g(x,y,z). \tag{3.36b}$$

Substituting Eq. (3.29) into Eq. (3.36a) and performing the necessary integrations yields

$$\phi^k_{gz1} = \frac{1}{120}\ [10\ a^k_{gz1} - a^k_{gz3}],$$

or, using Eq. (3.30a),

$$a^k_{gz3} = -120\ \phi^k_{gz1} + 10\ [\bar{\phi}^k_{gz}(+\Delta z^k/2) - \bar{\phi}^k_{gz}(-\Delta z^k/2)]. \tag{3.37}$$

The three-dimensional nodal scheme thus involves a total of five flux moments: the node-averaged flux, three hex-plane moments, and one axial moment. Equations for these moments are derived in the following sub-section.

3.4 The Flux Moments Equations

The zero-moment or node-averaged flux satisfies the nodal balance equation [Eq. (3.1)]:

$$\bar{\phi}^k_g = \frac{1}{\Sigma^{r,k}_g}\ \bar{Q}^k_g - \frac{2}{3h\Sigma^{r,k}_g}\ [\bar{L}^k_{gx} + \bar{L}^k_{gu} + \bar{L}^k_{gv}] - \frac{1}{\Delta z^k \Sigma^{r,k}_g}\ \bar{L}^k_{gz}. \tag{3.38}$$

This result can also be obtained via unit weighting of either Eq. (3.12) or (3.18).

The hex-plane moments equations are derived from Eq. (3.12) using the same procedure as in Section 2.5. The x-direction result is

$$[\Sigma_g^{r,k} + \frac{32}{h}\frac{D_g^k}{h}]\,\phi_{gxl}^k = Q_{gxl}^k - \frac{1}{\Delta z^k} L_{gzxl}^k$$

$$- \frac{2}{3h}\,[\bar{T}_{gx}^k + \bar{T}_{gu}^k - \bar{T}_{gv}^k] + \frac{40}{9h}\frac{D_g^k}{h}\, a_{gxl}^k. \qquad (3.39)$$

This equation is very similar to Eq. (2.70). The additional term

$$L_{gzxl}^k \equiv \frac{\Delta z^k}{V^k} \int_{-h/2}^{h/2} dx\ \mathrm{sgn}(x) \int_{-y_s(x)}^{y_s(x)} dy\ L_{gz}^k(x,y)$$

$$\equiv \frac{\Delta z^k}{V^k} \int_{-h/2}^{h/2} dx\ \mathrm{sgn}(x) \int_{-y_s(x)}^{y_s(x)} dy \int_{-\Delta z^k/2}^{\Delta z^k/2} dz\ -D_g^k \frac{\partial^2}{\partial z^2}\phi_g^k(x,y,z) \qquad (3.40)$$

is the x-direction moment of the partially-integrated axial leakage.

The axial flux moment equation is derived from Eq. (3.34) with w(z) given by Eq. (3.35b):

$$\langle w_{zl}(z)\frac{d}{dz} J_{gz}^k(z)\rangle + \Sigma_g^{r,k}\,\phi_{gzl}^k = Q_{gzl}^k - \frac{2}{3h} L_{gxyzl}^k, \qquad (3.41)$$

where the axial flux moment ϕ_{gzl}^k is defined in Eqs. (3.36), and

$$L_{gxyzl}^k \equiv \frac{3h}{2}\frac{1}{V^k} \int_{-\Delta z^k/2}^{\Delta z^k/2} dz\ \frac{z}{\Delta z^k} L_{gxy}^k(z) \qquad (3.42a)$$

$$\equiv \frac{3h}{2}\frac{1}{V^k}\int_{-\Delta z^k/2}^{\Delta z^k/2} dz\,\frac{z}{\Delta z^k}\int_{-h/2}^{h/2} dx\int_{-y_s(x)}^{y_s(x)} dy\; -D_g^k\left[\frac{\partial^2}{\partial x^2}+\frac{\partial^2}{\partial y^2}\right]\phi_g^k(x,y,z) \quad (3.42b)$$

is the axial moment of the partially-integrated hex-plane leakage. Integrating the first term in Eq. (3.41) by parts yields

$$\langle w_{z1}(z),\frac{d}{dz}J_{gz}^k(z)\rangle = \frac{1}{2\Delta z^k}\left[\bar{J}_{gz}^k(+\Delta z^k/2)-\bar{J}_{gz}^k(-\Delta z^k/2)\right]$$

$$+\frac{1}{\Delta z^k}\frac{D_g^k}{\Delta z^k}a_{gz1}^k, \quad (3.43)$$

where $\bar{J}_{gz}^k(z)$ and a_{gz1}^k are defined in Eqs. (3.26) and (3.30a), respectively. Substitution of Eq. (3.43) into Eq. (3.41) yields after rearrangement

$$\phi_{gz1}^k = \frac{1}{\Sigma_g^{r,k}}\left[Q_{gz1}^k-\frac{2}{3h}L_{gxyz1}^k\right]-\frac{1}{2}\frac{1}{\Delta z^k\,\Sigma_g^{r,k}}\bar{T}_{gz}^k$$

$$-\frac{D_g^k}{\Delta z^k}\frac{1}{\Delta z^k\,\Sigma_g^{r,k}}a_{gz1}^k, \quad (3.44)$$

where

$$\bar{T}_{gz}^k \equiv \bar{J}_{gz}^k(+\Delta z^k/2)+\bar{J}_{gz}^k(-\Delta z^k/2). \quad (3.45)$$

Equation (3.39) and its u- and v-direction analogs can be combined with Eq. (3.44) to yield

$$\begin{bmatrix} \phi^k_{gx1} \\ \phi^k_{gu1} \\ \phi^k_{gv1} \\ \phi^k_{gz1} \end{bmatrix} = \frac{h}{\alpha^k_{g1}} \begin{bmatrix} 1 & 0 & 0 & 0 \\ 0 & 1 & 0 & 0 \\ 0 & 0 & 1 & 0 \\ 0 & 0 & 0 & \alpha^k_{g2} \end{bmatrix} \begin{bmatrix} Q^k_{gx1} - \frac{1}{\Delta z^k} L^k_{gzx1} \\ Q^k_{gu1} - \frac{1}{\Delta z^k} L^k_{gzu1} \\ Q^k_{gv1} - \frac{1}{\Delta z^k} L^k_{gzv1} \\ Q^k_{gz1} - \frac{2}{3h} L^k_{gxyz1} \end{bmatrix}$$

$$- \frac{2}{3\alpha^k_{g1}} \begin{bmatrix} 1 & 1 & -1 & 0 \\ 1 & 1 & 1 & 0 \\ -1 & 1 & 1 & 0 \\ 0 & 0 & 0 & \alpha^k_{g3} \end{bmatrix} \begin{bmatrix} \bar{T}^k_{gx} \\ \bar{T}^k_{gu} \\ \bar{T}^k_{gv} \\ \bar{T}^k_{gz} \end{bmatrix}$$

$$+ \frac{40}{9\alpha^k_{g1}} \frac{D^k_g}{h} \begin{bmatrix} 1 & 0 & 0 & 0 \\ 0 & 1 & 0 & 0 \\ 0 & 0 & 1 & 0 \\ 0 & 0 & 0 & \alpha^k_{g4} \end{bmatrix} \begin{bmatrix} a^k_{gx1} \\ a^k_{gu1} \\ a^k_{gv1} \\ a^k_{gz1} \end{bmatrix} , \qquad (3.46)$$

where

$$\alpha^k_{g2} \equiv \frac{\alpha^k_{g1}}{h\Sigma^{r,k}_g} \qquad (3.47a)$$

$$\alpha_{g3}^{k} \equiv \frac{3\alpha_{g1}^{k}}{4\Delta z^{k}\,\Sigma_{g}^{r,k}} \tag{3.47b}$$

$$\alpha_{g4}^{k} \equiv \frac{9\alpha_{g1}^{k}}{40}\,\frac{h}{\Delta z^{k}}\,\frac{1}{\Delta z^{k}\,\Sigma_{g}^{r,k}}\quad , \tag{3.47c}$$

and α_{g1}^{k} is defined in Eq. (2.73). The calculation of the leakage moments L_{gzxl}^{k}, L_{gzul}^{k}, L_{gzvl}^{k}, and L_{gxyzl}^{k} is discussed in Section 3.6.

3.5 The Response Matrix Equation

The face-averaged partial currents in three dimensions are defined by

$$\bar{J}_{gx}^{out,k}(\pm h/2) \equiv \frac{1}{\Delta z^{k}} \int_{-\Delta z^{k}/2}^{\Delta z^{k}/2} dz \left[\frac{1}{2y_{s}(x)} \int_{-y_{s}(x)}^{y_{s}(x)} dy \left\{ \frac{1}{4}\,\phi_{g}^{k}(x,y,z) \mp \frac{1}{2}\,D_{g}^{k}\,\frac{\partial}{\partial x}\,\phi_{g}^{k}(x,y,z) \right\} \right]_{x=\pm h/2} \tag{3.48a}$$

$$\bar{J}_{gx}^{in,k}(\pm h/2) \equiv \frac{1}{\Delta z^{k}} \int_{-\Delta z^{k}/2}^{\Delta z^{k}/2} dz \left[\frac{1}{2y_{s}(x)} \int_{-y_{s}(x)}^{y_{s}(x)} dy \left\{ \frac{1}{4}\,\phi_{g}^{k}(x,y,z) \pm \frac{1}{2}\,D_{g}^{k}\,\frac{\partial}{\partial x}\,\phi_{g}^{k}(x,y,z) \right\} \right]_{x=\pm h/2} \tag{3.48b}$$

$$\bar{J}_{gz}^{out,k}(\pm\Delta z^k/2) \equiv \frac{\Delta z^k}{V^k} \int_{-h/2}^{h/2} dx \int_{-y_s(x)}^{y_s(x)} dy \left[\frac{1}{4} \phi_g^k(x,y,z) \right.$$

$$\left. \mp \frac{1}{2} D_g^k \frac{\partial}{\partial z} \phi_g^k(x,y,z) \right]_{z=\pm\Delta z^k/2} \tag{3.49a}$$

$$\bar{J}_{gz}^{in,k}(\pm\Delta z^k/2) \equiv \frac{\Delta z^k}{V^k} \int_{-h/2}^{h/2} dx \int_{-y_s(x)}^{y_s(x)} dy \left[\frac{1}{4} \phi_g^k(x,y,z) \right.$$

$$\left. \pm \frac{1}{2} D_g^k \frac{\partial}{\partial z} \phi_g^k(x,y,z) \right]_{z=\pm\Delta z^k/2} . \tag{3.49b}$$

The surface-averaged fluxes and net currents can be written in terms of the face-averaged partial currents using the relationships shown in Eqs. (2.76) and (2.77).

The equation used to compute $\bar{J}_{gx}^{out,k}(+h/2)$ is identical to Eq. (2.80) derived in Section 2.6:

$$\bar{J}_{gx}^{out,k}(+h/2) = \frac{-D_g^k}{h} \left[a_{gx1}^k + \frac{36}{13} a_{gx2}^k + \frac{7}{26} a_{gx3}^k + \frac{1}{2} a_{gx4}^k + E_{gx}^k(h/2) \right]$$

$$+ \bar{J}_{gx}^{in,k}(+h/2). \tag{3.50}$$

A similar equation for $\bar{J}_{gz}^{out,k}(+\Delta z^k/2)$ is derived by using the one-dimensional axial polynomial [Eq. (3.29)] to evaluate the derivative in Eq. (3.28). Substituting this result into the z-direction analog of Eq. (2.77a) yields

$$\bar{J}_{gz}^{out,k}(+\Delta z^k/2) = -\frac{D_g^k}{\Delta z^k} \left[a_{gz1}^k + 3a_{gz2}^k + \frac{1}{2} a_{gz3}^k \right] + \bar{J}_{gz}^{in,k}(+\Delta z^k/2). \tag{3.51}$$

The derivation of the final form of the three-dimensional response matrix equation follows the five steps described in Section 2.6. We repeat these steps here, with some obvious overlap, for the three-dimensional case. Additional details are provided in Appendix B.

(1) The expansion coefficients a^k_{gx1}, a^k_{gx2}, a^k_{gx3}, and a^k_{gx4} are are eliminated from Eq. (3.51) using Eqs. (2.34a), (2.34b), (2.53) and (2.59b), respectively. The term $E^k_g(h/2)$ is eliminated using Eqs. (2.43) and (2.44). The expansion coefficients a^k_{gz1}, a^k_{gz2}, and a^k_{gz3} are eliminated from Eq. (3.53) using Eqs. (3.30a), (3.30b), and (3.37), respectively.

(2) The flux moments $\bar{\phi}^k_g$, $\bar{\phi}^k_{gx1}$, and $\bar{\phi}^k_{gz1}$ introduced via step (1) are eliminated in favor of the source moments $\bar{Q}^k_g$, Q^k_{gx1}, and Q^k_{gz1} and the leakage moments L^k_{gzx1} and L^k_{gxyz1} using Eqs. (3.38), (3.39), and (3.44), respectively.

(3) All surface-averaged fluxes and net currents introduced via steps (1) and (2) are eliminated in favor of surface-averaged partial currents using Eqs. (2.76) and (2.77) and their z-directed analogs. Equations (3.50) and (3.51) can then be written as

$$[a_1\ a_2\ a_3\ a_4\ a_3\ a_2\ a_5\ a_5]\ \underline{J}_g^{out,k} = [b_1\ b_2] \begin{bmatrix} \bar{Q}^k_g \\ \\ Q^k_{gx1} - \frac{1}{\Delta z^k} L^k_{gzx1} \end{bmatrix}$$

$$+ [c_1\ c_2\ c_3\ c_4\ c_3\ c_2\ c_5\ c_5]\ \underline{J}_g^{in,k} \qquad (3.52)$$

and

$$[a_6\ a_6\ a_6\ a_6\ a_6\ a_6\ a_7\ a_8]\ \underline{J}_g^{out,k} = [b_3\ b_4] \begin{bmatrix} \bar{Q}^k_g \\ \\ Q^k_{gz1} - \frac{2}{3h} L^k_{gxyz1} \end{bmatrix}$$

$$+ [c_6\ c_6\ c_6\ c_6\ c_6\ c_6\ c_7\ c_8]\ \underline{J}_g^{in,k}, \qquad (3.53)$$

respectively, where $\underline{J}_g^{out,k}$ and $\underline{J}_g^{in,k}$ are column vectors containing the eight outgoing and eight incoming partial currents, respectively, for the k-th node, e.g.

$$\underline{J}_g^{out,k} \equiv \text{col}\ [\bar{J}_{gx}^{out,k}(+h/2),\ \bar{J}_{gu}^{out,k}(+h/2),\ \bar{J}_{gv}^{out,k}(+h/2),\ \bar{J}_{gx}^{out,k}(-h/2),$$

$$\bar{J}_{gu}^{out,k}(-h/2),\ \bar{J}_{gv}^{out,k}(-h/2),\ \bar{J}_{gz}^{out,k}(+\Delta z^k/2),\ \bar{J}_{gz}^{out,k}(-\Delta z^k/2)]. \quad (3.54)$$

The constants a_i, b_i, and c_i are defined in Appendix B.

(4) Five additional equations similar to Eq. (3.52) can be obtained by applying successive 60° rotational transformations to Eq. (3.52). Calculation of $\bar{J}_{gz}^{out,k}(-\Delta z^k/2)$ yields an additional equation similar to Eq. (3.55). These additional equations can be combined with Eqs. (3.52) and (3.53) to yield

$$[A_g^k]\ \underline{J}_g^{out,k} = [B_g^k]\ \{\underline{Q}_g^k - \underline{L}_g^k\} + [C_g^k]\ \underline{J}_g^{in,k}, \quad (3.55)$$

where

$$\underline{Q}_g^k \equiv \text{col}\ [\bar{Q}_g^k,\ Q_{gxl}^k,\ Q_{gul}^k,\ Q_{gvl}^k,\ Q_{gzl}^k] \quad (3.56)$$

and

$$\underline{L}_g^k \equiv \text{col}\ [0,\ \frac{1}{\Delta z^k} L_{gzxl}^k,\ \frac{1}{\Delta z^k} L_{gzul}^k,\ \frac{1}{\Delta z^k} L_{gzvl}^k,\ \frac{2}{3h} L_{gxyzl}^k]. \quad (3.57)$$

(5) The final form of the response matrix equation is obtained by inverting $[A_g^k]$ in Eq. (3.55) to yield

$$\underline{J}_g^{out,k} = [P_g^k]\ \{\underline{Q}_g^k - \underline{L}_g^k\} + [R_g^k]\ \underline{J}_g^{in,k}, \quad (3.58)$$

where $[P_g^k]$ is an 8 by 5 source matrix and $[R_g^k]$ is an 8 by 8 response matrix equation.

As before, the source term is calculated using

$$\underline{Q}_g^k = \frac{1}{\lambda} \chi_g \sum_{g'=1}^{G} \nu\Sigma_{g'}^{f,k}\ \underline{\phi}_{g'}^k + \sum_{g' \neq g} \Sigma_{gg'}^{s,k}\ \underline{\phi}_{g'}^k, \quad (3.59)$$

where

$$\underline{\phi}_g^k \equiv \text{col}\ [\bar{\phi}_g^k,\ \phi_{gx1}^k,\ \phi_{gu1}^k,\ \phi_{gv1}^k,\ \phi_{gz1}^k]. \tag{3.60}$$

In three dimensions, $[P_g^k]$ and $[R_g^k]$ contain 5 and 8 unique entries, respectively. As in two dimensions, these entries depend only on the material properties and axial mesh spacing of the k-th node, and thus need be computed and stored only for unique nodes characterized by their material composition assignment and axial mesh spacing.

The incorporation of boundary conditions into the global solution of Eq. (3.58) is accomplished in the same manner as discussed in Section 2.7.

3.6 Calculation of the Leakage Moments

The x-direction moment [Eq. (3.40)] of the partially-integrated axial leakage [Eq. (3.14)] is calculated using the approximation

$$L_{gz}^k(x,y) \cong \bar{L}_{gz}^k. \tag{3.61}$$

Thus the space-dependent axial leakage is simply replaced by its average value over the z-directed faces. Substitution of Eq. (3.61) into Eq. (3.40) and its u- and v-direction analogs yields

$$L_{gzx1}^k \equiv L_{gzu1}^k \equiv L_{gzv1}^k \equiv 0. \tag{3.62}$$

The axial moment [Eq. (3.42)] of the partially-integrated hex-plane leakage [Eq. 3.22] is calculated using the approximation

$$L_{gxy}^k(z) \cong \rho_{gxy}^k(z), \qquad z\varepsilon\ \Delta z^k, \tag{3.63}$$

where $\rho_{gxy}^k(z)$ is a quadratic polynomial:

$$\rho_{gxy}^k(z) \equiv \bar{L}_{gxy}^k + \rho_{gxy1}^k\ f_{z1}(z) + \rho_{gxy2}^k\ f_{z2}(z), \qquad z\varepsilon\ [z_1,\ z_2]. \tag{3.64}$$

Here $f_{z1}(z)$ and $f_{z2}(z)$ are as given in Eqs. (3.31a) and (3.31b), and z_1 and z_2 will be defined shortly. This "quadratic leakage" approximation[15] has been used extensively in the development of recent Cartesian-geometry nodal schemes.[15-20] Setting $\rho^k_{gxy1} \equiv \rho^k_{gxy2} \equiv 0$ in Eq. (3.64) reduces Eq. (2.63) to a "flat leakage" approximation as in Eq. (3.61). The coefficients ρ^k_{gxy1} and ρ^k_{gxy2} are calculated in the following manner. Let k- and k+ denote the neighboring nodes in the minus and plus z-directions, i.e. the nodes immediately below and above the k-th node, respectively. The coordinates z_1 and z_2 are defined by

$$z_1 \equiv -\Delta z^k/2 - \Delta z^{k-} \tag{3.65a}$$

$$z_2 \equiv +\Delta z^k/2 + \Delta z^{k+}, \tag{3.65b}$$

and thus the quadratic polynomial extends over the three nodes k-, k, and k+. The expansion coefficients in Eq. (3.64) are calculated such that the total hex-plane leakages [Eq. (3.23)] in the nodes k- and k+ are preserved:

$$\bar{L}^{k-}_{gxy} \equiv \frac{3h}{2}\frac{1}{V^{k-}}\int_{z_1}^{-\Delta z^k/2} dz\ \rho^k_{gxy}(z) \tag{3.66a}$$

$$\bar{L}^{k+}_{gxy} \equiv \frac{3h}{2}\frac{1}{V^{k+}}\int_{+\Delta z^k/2}^{z_2} dz\ \rho^k_{gxy}(z). \tag{3.66b}$$

The required leakage moment is calculated by substituting Eq. (3.63) into Eq. (3.42a) and performing the necessary integrations:

$$L^k_{gxyz1} = \frac{3h}{2}\frac{\Delta z^k}{V^k}\frac{1}{12}\rho^k_{gxy1}. \tag{3.67}$$

As shown in Section C.1 of Appendix C, this procedure leads to the final result

$$L^k_{gxyzl} \equiv \mu^k_- \left[\bar{L}^k_{gxy} - \bar{L}^{k-}_{gxy}\right] + \mu^k_+ \left[\bar{L}^{k+}_{gxy} - \bar{L}^k_{gxy}\right], \tag{3.68}$$

where the coefficients μ^k_- and μ^k_+ depend only upon the axial mesh spacings:

$$\mu^k_- \equiv \frac{\Delta z^k}{12d}\left[2\Delta z^{k+} + \Delta z^k\right]\left[\Delta z^{k+} + \Delta z^k\right] \tag{3.69a}$$

$$\mu^k_+ \equiv \frac{\Delta z^k}{12d}\left[2\Delta z^{k-} + \Delta z^k\right]\left[\Delta z^{k-} + \Delta z^k\right] \tag{3.69b}$$

$$d \equiv \left[\Delta z^{k-} + \Delta z^k\right]\left[\Delta z^{k-} + \Delta z^k + \Delta z^{k+}\right]\left[\Delta z^k + \Delta z^{k+}\right]. \tag{3.69c}$$

The incorporation of axial boundary conditions into the calculation of these coefficients is discussed in Appendix C. Using Eq. (3.24), the total hex-plane leakages shown in Eq. (3.68) can be computed in terms of the directional leakages $\bar{L}^k_{gx}$, $\bar{L}^k_{gu}$, and $\bar{L}^k_{gv}$, which, in turn, are readily calculated using the available face-averaged partial currents.

The quadratic approximation to $L^k_{gxy}(z)$ is necessary in order to obtain sufficient accuracy using coarse (~20 cm) axial meshes. The flat approximation to $L^k_{gz}(x,y)$ is clearly less accurate, although the error due to this approximation will remain within acceptable limits provided the second derivatives of $L^k_{gz}(x,y)$ over the node are (in some sense) small. This should be the case in typical LMFBR designs in which the lattice pitch is ~11 to 16 cm, or only 2 to 3 diffusion lengths.

The contribution to the total error due to the approximations introduced in Eqs. (3.61) and (3.63) is analyzed in Appendix C for a simple homogeneous model problem. The results of this study confirm the accuracy of the quadratic approximation to $L^k_{gxy}(z)$, and further suggest that the error due to the flat approximation of $L^k_{gz}(x,y)$ represents a significant contribution to the total error. It is clear that this error could be essentially eliminated by introducing a quadratic approximation analogous to Eq. (3.63), i.e.

$$\int_{-y_s(x)}^{y_s(x)} dy\, L^k_{gz}(x,y) \equiv \rho^k_{gz}(x), \tag{3.70}$$

where $\rho_{gz}^{k}(x)$ is a quadratic polynomial extending over the two neighboring nodes in the x-direction. Use of this approximation plus the analogous expressions in the u- and v-directions leads to expressions of the form shown in Eq. (3.68), only involving axial leakages in the six neighboring nodes in the hex-plane. From a computational viewpoint, the calculation of the axial moments using Eq. (3.68) is relatively straightforward; however, the additional hex-plane coupling introduced by Eq. (3.70) would greatly complicate the solution of the partial currents. Furthermore, although the results in Appendix C suggest that the flat leakage approximation has a significant effect on the overall accuracy of the nodal scheme, the numerical results presented in Section 5 demonstrate that in spite of Eq. (3.61), very acceptable accuracy is obtained in three-dimensional nodal calculations. For these reasons, the approximation given in Eq. (3.70) has not been implemented in the DIF3D nodal option.

3.7 Summary

The three-dimensional nodal scheme derived in this section involves a total of 13 principal unknowns per node per group: 8 surface-averaged outgoing partial currents and 5 spatial moments of the intra-node flux distribution. The partial currents are calculated from the response matrix equation, Eq. (3.58), while the flux moments are computed using Eqs. (3.38) and (3.46). The required source moments are obtained from Eq. (3.59), and the leakage moments are calculated using Eqs. (3.62) and (3.68).

4. NUMERICAL SOLUTION OF THE NODAL EQUATIONS

4.1 Overview of the Solution Procedure

The nodal equations are solved using a conventional fission source iteration procedure[21] accelerated by coarse-mesh rebalance[21,22] and asymptotic source extrapolation.[23] At each fission source (or "outer") iteration, the interface partial currents for each group are computed by solving the response matrix equations with a known group source term. This solution is accomplished via a series of sweeps through the spatial mesh. These sweeps, which are discussed in Section 4.2, are analogous to the "inner" iterations used to invert the in-group diffusion-removal matrix in the finite difference option. The coarse-mesh rebalance and asymptotic source extrapolation procedures are described in Sections 4.3 and 4.4, respectively.

The algorithm used to solve the nodal equations is shown in Fig. 4.1. The nodal coupling coefficients are computed prior to the start of the outer iterations (n is the outer iteration index). The solution vectors (i.e. the flux moments, interface partial currents, and fission source moments) are initialized by assuming a spatially constant flux distribution in each energy group. As shown in Fig. 4.1, the loop over energy groups performed at each outer iteration consists of the following steps:

(1) The coarse-mesh rebalance factors and asymptotic source extrapolation factor computed at the previous outer iteration are applied to the partial currents and fission source moments as described in Sections 4.3 and 4.4.

(2) The group source term of outer iteration n is computed using Eq. (3.59):

$$\underline{Q}_g^{k(n)} = \frac{1}{\lambda^{(n-1)}} \chi_g \underline{\Psi}^{k(n-1)} + \sum_{g'<g} \Sigma_{gg'}^{s,k} \underline{\phi}_{g'}^{k(n)}, \quad k = 1,\ldots,K, \tag{4.1}$$

where $\underline{\Psi}^k$ is a vector containing the fission source moments, i.e.

$$\underline{\Psi}^k \equiv \sum_{g'=1}^{G} \nu\Sigma_{g'}^{f,k} \underline{\phi}_{g'}^{k} \quad , \tag{4.2}$$

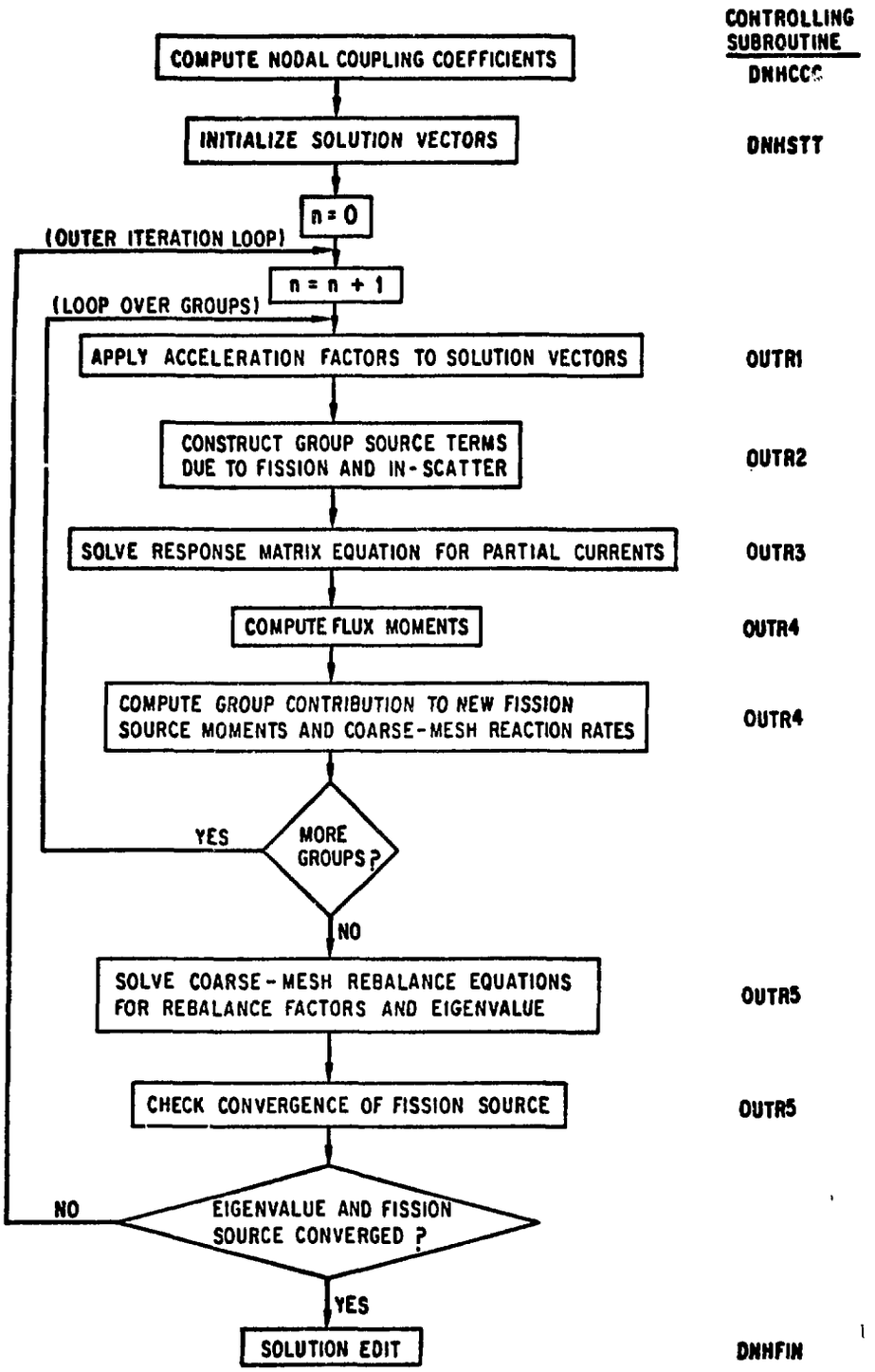

Fig. 4.1 Overview of the Nodal Solution Algorithm

and $\lambda^{(n-1)}$ is the eigenvalue computed at the previous outer iteration. The in-scatter contribution in Eq. (4.1) is evaluated assuming no up-scatter.*

(3) The interface partial currents are computed by solving the response matrix equations [Eq. (2.85) or Eq. (3.58)] with known source terms $Q_g^{k(n)}$. This calculation involves a series of inner iterations discussed in Section 4.2.

(4) The flux moments are calculated from either Eqs. (2.72) and (2.74) (two dimensions) or Eqs. (3.38) and (3.46) (three-dimensions) using the most recently computed partial currents to evaluate all terms in these equations with the exception of the transverse leakage moment L^k_{gxyzl} in Eq. (3.46). This latter term retains its value used in the calculation of the partial currents at the final inner iteration preceeding the flux-moment calculation.

(5) The calculated flux moments are then used to compute the group contribution to the new fission source moments [Eq. (4.2)]. The group contributions to the reaction rates and leakages required for the coarse-mesh balance equations are also computed.

Once all energy groups have been processed, the coarse-mesh rebalance equations are solved and the convergence of the fission source is checked for asymptotic behavior. The outer iterations are terminated when the following convergence criteria are satisfied:

Eigenvalue:
$$\left|\lambda^{(n)} - \lambda^{(n-1)}\right| < \varepsilon_1 \tag{4.3a}$$

Pointwise Fission Source:
$$\max_k \left|\frac{\psi^{k(n)} - \psi^{k(n-1)}}{\psi^{k(n)}}\right| < \varepsilon_2 \tag{4.3b}$$

Average Fission Source:
$$\frac{1}{K}\left[\sum_{k=1}^{K} \left[\frac{\psi^{k(n)} - \psi^{k(n-1)}}{\psi^{k(n)}}\right]^2\right]^{1/2} < \varepsilon_3 \,. \tag{4.3c}$$

The default values of the convergence criteria ε_1, ε_2, and ε_3 are 1.0×10^{-7}, 1.0×10^{-5}, and 1.0×10^{-5}, respectively.

*Up-scattering is not permitted in the DIF3D nodal option.

4.2 Solution of the Response Matrix Equations

4.2.1 Two Dimensions

The two-dimensional response matrix equations are solved in each group at each outer iteration by sweeping the nodes in the "four color checkerboard" ordering shown in Fig. 4.2. This ordering is motivated by the "red-black checkerboard" ordering (often referred to as σ_1 - ordering[21]) in Cartesian geometry. Note that the hexagons are assigned colors (i=1,...,4) such that two hexagons of the same color do not share a common surface. (It is also possible to color a hexagonal map using only three colors.) The ordering in Fig. 4.2 suggests an iterative procedure based on a mesh sweep (or inner iteration) consisting of four passes through the mesh in which all outgoing partial currents from nodes of color i are computed during the i-th pass. Letting n and ml denote the outer and inner iteration indices, respectively, the local response matrix equation solved at each node is

$$\underline{J}_g^{out,k(n,ml)} = [P_g^k]\ \underline{Q}_g^{k(n)} + [R_g^k]\ \underline{J}_g^{in,k(n,ml/ml-1)}, \tag{4.4}$$

where the incoming partial currents are the most recently computed outgoing partial currents from neighboring nodes. The incoming partial currents on the outer boundary are updated at the end of each inner iteration using Eq. (2.89). Models with either sixth- or third-core symmetry are solved by sweeping only over those nodes contained in the fractional-core region of solution.

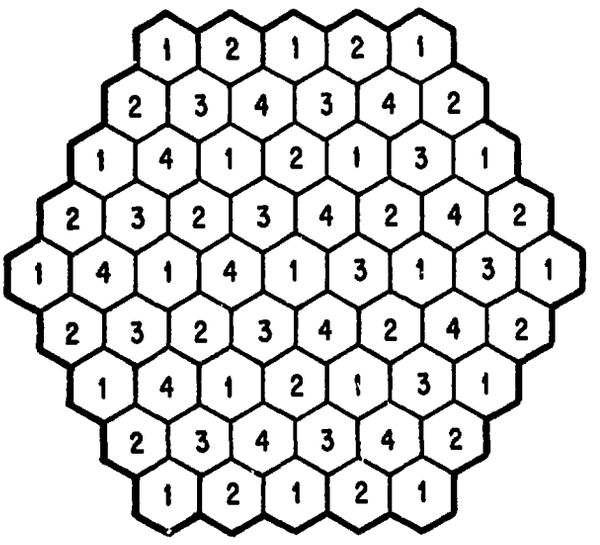

Fig. 4.2 The Four-Color Checkerboard Ordering in Hexagonal Geometry

The choice of this inner iteration procedure is based on two primary considerations: First, because the convergence rate of the outer iterations can be reduced by the introduction of higher harmonics during the inner iterations, it is important that the partial currents be computed such that any symmetry inherent in the problem be preserved by the inner iteration procedure. For example, given a third-core symmetric source distribution, a single mesh sweep in the ordering shown in Fig. 4.2 will produce a partial current solution which is exactly third-core symmetric. Although this scheme does not preserve exactly either sixth- or twelfth-core symmetry, it does so approximately since exact twelfth-core symmetry would be preserved for $1 \equiv 2$ and $3 \equiv 4$ in Fig. 4.2.

The second consideration in the choice of an iterative procedure is the following: Since the structure [see Eq. (A.49)] of $[R_g^k]$ permits very efficient coding of the operations necessary to calculate simultaneously all outgoing partial currents from a node, it is considered important that Eq. (4.4) be solved in such a manner. For example, although a scheme in which all hexagons on a ring are solved simultaneously preserves all possible symmetries, it sacrifices the computational advantages inherent in Eq. (4.4) by requiring the formation and solution of penta-diagonal matrix equations for the partial currents across surfaces shared by hexagons on the same ring. Other schemes which are contrary to one or both of the above considerations include (a) solving simultaneously for all x-directed partial currents on each x-line, followed by similar solutions on u- and v-lines, and (b) solving simultaneously for all outgoing partial currents from all nodes on an x-line. This latter scheme is analogous to the line over-relaxation procedure[14] employed in the DIF3D finite difference option. Thus, in conclusion, the four-color checkerboard sweep appears to offer a compromise between preserving inherent problem symmetry and exploiting the computational advantages associated with the direct solution of Eq. (4.4) for each node.

This inner iteration procedure is equivalent to a Gauss-Seidel iteration[21] applied to the global response matrix equation.* To demonstrate, we introduce the global partial current vector

$$\underline{J}_{gxy}^{out} \equiv \text{col}\,[\underline{J}_{gxy1}^{out}, \underline{J}_{gxy2}^{out}, \underline{J}_{gxy3}^{out}, \underline{J}_{gxy4}^{out}, \underline{J}_{gxy}^{in,B}], \tag{4.5}$$

where

$\underline{J}_{gxyi}^{out}$ contains all outgoing partial currents for nodes of color i, i = 1,...,4,

*In the following discussion it is assumed that the outgoing partial currents from all nodes of the same color can be solved simultaneously, i.e. that any node can be decoupled from all other nodes of the same color. This is rigorously true only for the full-core model shown in Fig. 4.2. It is not true for fractional-core models (see Fig. 7.2) with periodic boundary conditions since nodes of the same color may be coupled via the periodic boundary conditions. The terms introduced by this periodic coupling have been omitted in the development of the two-dimensional Gauss-Seidel procedure in order to simplify the presentation.

and

$\underline{J}_{gxy}^{in,B}$ contains all incoming partial currents for group g on the outer boundary.

The global source vector is

$$\underline{S}_{gxy} \equiv \text{col}\ [\underline{S}_{gxy1},\ \underline{S}_{gxy2},\ \underline{S}_{gxy3},\ \underline{S}_{gxy4},\ 0], \tag{4.6}$$

where

$\underline{S}_{gxyi}$ contains the terms $[P_g^k]\underline{Q}_g^k$ for all nodes of color i.

Eliminating incoming partial currents across the interior surfaces in favor of outgoing partial currents, and then combining the local response matrix equations for all nodes with the boundary conditions [Eq. (2.89)] yields the global response matrix equation for group g:

$$[R_g^{xy}]\ \underline{J}_{gxy}^{out(n)} = \underline{S}_{gxy}^{(n)}. \tag{4.7}$$

The global response matrix is

$$[R_g^{xy}] \equiv \begin{bmatrix} [I] & -[r_{12}] & -[r_{13}] & -[r_{14}] & -[r_{1B}] \\ -[r_{21}] & [I] & -[r_{23}] & -[r_{24}] & -[r_{2B}] \\ -[r_{31}] & -[r_{32}] & [I] & -[r_{34}] & -[r_{3B}] \\ -[r_{41}] & -[r_{42}] & -[r_{43}] & [I] & -[r_{4B}] \\ -[r_{B1}] & -[r_{B2}] & -[r_{B3}] & -[r_{B4}] & [I] \end{bmatrix}, \tag{4.8}$$

where

$[r_{ij}]$ and $[r_{iB}]$ contain entries of $[R_g^k]$ for nodes of color i,

$[r_{Bi}]$ contain the boundary coefficients introduced in Eq. (2.89),

and [I] is the identity matrix. Applying the Gauss-Seidel procedure to Eq. (4.7) yields

$$\underline{J}_{gxy1}^{out(ml)} = \underline{S}_{gxy1}^{(n)} + [r_{12}]\,\underline{J}_{gxy2}^{out(ml-1)} + [r_{13}]\,\underline{J}_{gxy3}^{out(ml-1)}$$

$$+ [r_{14}]\,\underline{J}_{gxy4}^{out(ml-1)} + [r_{1B}]\,\underline{J}_{gxy}^{in,B(ml-1)}$$

$$\vdots$$

$$\underline{J}_{gxy4}^{out(ml)} = \underline{S}_{gxy4}^{(n)} + [r_{41}]\,\underline{J}_{gxy1}^{out(ml)} + [r_{42}]\,\underline{J}_{gxy2}^{out(ml)}$$

$$+ [r_{43}]\,\underline{J}_{gxy3}^{out(ml)} + [r_{46}]\,\underline{J}_{gxy}^{in,B(ml-1)}$$

$$\underline{J}_{gxy}^{in,b(ml)} = [r_{B1}]\,\underline{J}_{gxy1}^{out(ml)} + [r_{B2}]\,\underline{J}_{gxy2}^{out(ml)} + [r_{B3}]\,\underline{J}_{gxy3}^{out(ml)}$$

$$+ [r_{B4}]\,\underline{J}_{gxy4}^{out(ml)}, \quad ml = 1,\ldots,Ml_g. \tag{4.9}$$

The outer iteration index n has been dropped from the partial current vectors to simplify the notation.

The number (Ml_g) of inner iterations per outer iteration in group g is determined in the following manner. Let

$$\overline{\kappa_g h} \equiv \frac{1}{K}\sum_{k=1}^{K} \kappa_g^k\, h, \qquad \kappa_g^k \equiv \sqrt{\Sigma_g^{r,k}/D_g^k}\ , \tag{4.10}$$

where the summation is over all nodes in the reactor. Thus $\overline{\kappa_g h}$ is simply the reactor-averaged value of the node dimension (i.e. the lattice pitch) measured in diffusion lengths.* The convergence rate of the iterative

*The diffusion length L_g is defined by $L_g^2 \equiv D_g/\Sigma_g^r$.

procedure shown in Eq. (4.9) increases with increasing $\overline{\kappa_g h}$ since the spectral radius[21] of the Gauss-Seidel iteration matrix decreases with increasing node size. The decreased spectral radius of the iteration matrix is due to the decreasing values of the transmission coefficient (see Appendix A) with increased node size, which in turn increases the diagonal dominance of the global response matrix $[R_g^{xy}]$. In view of this observation, plus numerical results for a number of test problems, the following simple formula is used to determine the number of inner iterations to be performed at each outer iteration:

$$Ml_g \equiv \begin{cases} 2 & \overline{\kappa_g h} > 1 \\ 4 & \overline{\kappa_g h} < 1 \end{cases} . \tag{4.11}$$

In only one problem studied to date has a value of $\overline{\kappa_g h} < 1$ been observed. (This occurred in group 2 of the SNR benchmark problem discussed in Section 5.2.) Thus, in two-dimensional calculations, only two Gauss-Seidel iterations of Eq. (4.7) are typically performed in each energy group at each outer iteration.

4.2.2 Three Dimensions

Before discussing the solution procedure in three dimensions, it is convenient to partition the local three-dimensional response matrix equation into two coupled equations for the hex-plane and axial partial currents:

$$\underline{J}_{gxy}^{out,k} = [P_{gxy}^k]\ \underline{Q}_g^k + [R_{gxy}^k]\ \underline{J}_{gxy}^{in,k} + [R_{gxyz}^k]\ \underline{J}_{gz}^{in,k} \tag{4.12a}$$

$$\underline{J}_{gz}^{out,k} = [P_{gz}^k]\ \{\underline{Q}_g^k - \underline{L}_g^k\} + [R_{gz}^k]\ \underline{J}_{gz}^{in,k} + [R_{gzxy}^k]\ \underline{J}_{gxy}^{in,k}, \tag{4.12b}$$

where $\underline{J}_{gxy}^{out,k}$ and $\underline{J}_{gz}^{out,k}$ contain, respectively, the six outgoing partial currents in the hex-plane and the two outgoing partial currents in the z-direction for the k-th node. The structures of the sub-matrices introduced here are shown in Eqs. (B.30) and (B.31). Using the leakage approximations shown in Eq. (3.62), the leakage-moment vector defined in Eq. (3.57) becomes

$$\underline{L}_g^k \equiv \text{col}\ [0,\ 0,\ 0,\ 0,\ \frac{2}{3h}\ L_{gxyz1}^k].$$

As shown in Eq. (4.12a), the leakage moment shown here does not enter into the calculation of the hex-plane partial currents.

Equations (4.12) are solved by sweeping the axial mesh planes in a standard red-black checkerboard ordering, i.e. the odd-numbered planes are processed during the first pass, followed by the even-numbered planes on the second pass. The following calculations are performed for each plane encountered in this two-pass axial sweep: (1) The hex-plane partial currents are calculated using Eq. (4.12a) as the nodes are swept in the four-color checkerboard ordering described in the previous subsection. (2) These hex-plane partial currents are used in conjunction with the corresponding hex-plane partial currents on the two neighboring planes to compute the leakage moment L^k_{gxyzl} as shown in Eq. (3.68). (3) The outgoing z-directed partial currents are then computed using Eq. (4.12b) during a single (sequential) sweep of the nodes on the plane. The incoming partial currents on the axial boundaries are computed as in Eq. (2.89). Two complete sweeps in the axial direction are performed in each group at each outer iteration.

As in two dimensions, this iterative procedure is equivalent to a Gauss-Seidel iteration of a global matrix equation. Let

$$\underline{J}^{out}_{gxy,odd} \equiv \text{col}\ [\underline{J}^{out,1}_{gxy},\ \underline{J}^{out,3}_{gxy},\ \ldots]$$

$$\underline{J}^{out}_{gxy,evn} \equiv \text{col}\ [\underline{J}^{out,2}_{gxy},\ \underline{J}^{out,4}_{gxy},\ \ldots],$$

where $\underline{J}^{out,\ell}_{gxy}$ denotes $\underline{J}^{out}_{gxy}$ [defined in Eq. (4.5)] written for the ℓ-th plane. Thus $\underline{J}^{out}_{gxy,odd}$ and $\underline{J}^{out}_{gxy,evn}$ contain all hex-plane partial currents for the odd- and even-numbered planes, respectively. Furthermore, let

$\underline{J}^{out}_{gz,odd}$ and $\underline{J}^{out}_{gz,evn}$ contain outgoing z-directed partial currents for all nodes on odd-and even-numbered planes, respectively,

$\underline{J}^{in,B}_{gz}$ contain all incoming z-directed partial currents on the outer axial boundaries,

$\underline{L}_{g,odd}$ and $\underline{L}_{g,evn}$ contain the leakage moments L^k_{gxyzl} [see Eqs. (3.42) and (3.68)] for all nodes on odd- and even-numbered planes, respectively,

$\underline{S}_{gxy,odd}$ and $\underline{S}_{gxy,evn}$ contain the terms $[P^k_{gxy}]\underline{Q}^k_g$ for all nodes on odd- and even-numbered planes, respectively,

and

$\underline{S}_{gz,odd}$ and $\underline{S}_{gz,evn}$ contain the terms $[P^k_{gz}]\underline{Q}^k_g$ for all nodes on odd- and even-numbered planes, respectively.

The global matrix equation is

$$\begin{bmatrix} [r_1^{xy}] & [0] & [0] & [0] & -[r_1^{xyz}] & [0] & -[r_{1B}^{xyz}] \\ -[r_1^{zxy}] & [I] & [p_1^z] & [0] & -[r_1^z] & [0] & -[r_{1B}^z] \\ -[\mu_{11}^z] & [0] & [I] & -[\mu_{12}^z] & [0] & [0] & [0] \\ [0] & -[r_2^{xyz}] & [0] & [r_2^{xy}] & [0] & [0] & -[r_{2B}^{xyz}] \\ [0] & -[r_2^z] & [0] & -[r_2^{zxy}] & [I] & [p_2^z] & -[r_{2B}^z] \\ -[\mu_{21}^z] & [0] & [0] & -[\mu_{22}^z] & [0] & [I] & [0] \\ [0] & -[r_{B1}^z] & [0] & [0] & -[r_{B2}^z] & [0] & [I] \end{bmatrix} \begin{bmatrix} \underline{J}^{out}_{gxy,odd} \\ \underline{J}^{out}_{gz,odd} \\ \underline{L}_{g,odd} \\ \underline{J}^{out}_{gxy,evn} \\ \underline{J}^{out}_{gz,evn} \\ \underline{L}_{g,evn} \\ \underline{J}^{in,B}_{gz} \end{bmatrix} = \begin{bmatrix} \underline{S}^{(n)}_{gxy,odd} \\ \underline{S}^{(n)}_{gz,odd} \\ \underline{0} \\ \underline{S}^{(n)}_{gxy,evn} \\ \underline{S}^{(n)}_{gz,evn} \\ \underline{0} \\ \underline{0} \end{bmatrix}. \tag{4.13}$$

where, with reference to Eqs. (4.12),

$[r_i^{xy}]$, $i = 1,2$, contain entries of $[R^k_{gxy}]$ for nodes on odd- and even numbered planes, respectively,

$[r_i^{xyz}]$ and $[r_{iB}^{xyz}]$, $i = 1,2$, contain entries of $[R^k_{gxyz}]$,

$[r_i^{zxy}]$, $i = 1,2$, contain entries of $[R^k_{gzxy}]$,

and

$[r_i^z]$ and $[r_{iB}^z]$, i = 1,2, contain entries of $[R_{gz}^k]$.

In addition,

$[p_i^z]$, i = 1,2, contain the coefficents p_1^z shown in Eq. (B.31)

$[\mu_{i1}^z]$ and $[\mu_{i2}^z]$, i = 1,2, contain the transverse leakage coefficients introduced in Eq. (3.68),

and

$[r_{Bi}^z]$, i = 1,2, contain the axial boundary coefficients analogous to those introduced in Eq. (2.89).

Applying the Gauss-Seidel procedure to Eq. (4.13) yields

$$[r_1^{xy}]\ \underline{J}_{gxy,odd}^{out(m2)} = \underline{S}_{gxy,odd}^{(n)} + [r_1^{xyz}]\ \underline{J}_{gxy,evn}^{out(m2-1)} + [r_{1B}^{xyz}]\ \underline{J}_{gz}^{in,B(m2-1)}$$

$$\underline{J}_{gz,odd}^{out(m2)} = \underline{S}_{gz,odd}^{(n)} - [p_1^z]\ \underline{L}_{g,odd}^{(m2-1)} + [r_1^{zxy}]\ \underline{J}_{gxy,odd}^{out(m2)}$$

$$+ [r_1^z]\ \underline{J}_{gz,evn}^{out,(m2-1)} + [r_{1B}^z]\ \underline{J}_{gz}^{in,B(m2-1)}$$

$$\underline{L}_{g,odd}^{(m2)} = [\mu_{11}^z]\ \underline{J}_{gxy,odd}^{out(m2)} + [\mu_{12}^z]\ \underline{J}_{gxy,evn}^{out(m2-1)}$$

$$\vdots$$

$$\underline{J}_{gz}^{in,B(m2)} = [r_{B1}^z]\ \underline{J}_{gz,odd}^{out,(m2)} + [r_{B2}^z]\ \underline{J}_{gz,evn}^{out(m2)},$$

$$m2 = 1,\ldots,M2. \qquad (4.14)$$

Here m2 denotes the axial sweep index, and the outer iteration index n has been dropped from the partial current vectors to simplify the notation. As mentioned previously, two axial sweeps per group are performed at each outer iteration, and thus

$$M2_g \equiv 2, \qquad g = 1,\ldots,G. \tag{4.15}$$

It is clear that the matrix in Eq. (4.13) is reducible since the leakage vectors $\underline{L}_{g,odd}$ and $\underline{L}_{g,evn}$ can be written in terms of the hex-plane partial current vectors $\underline{J}^{out}_{gxy,odd}$ and $\underline{J}^{out}_{gxy,evn}$. However, we prefer the form shown since, in the actual calculation, the leakage moments are not eliminated in favor of the partial currents.

The matrices $[r_1^{xy}]$ and $[r_2^{xy}]$ are block-diagonal with block sub-matrices identical to the two-dimensional matrix $[R_g]$ shown in Eq. (4.8). Therefore, the equations represented by the first line in Eq. (4.14) can be decoupled into separate equations for each of the odd-numbered planes. These single-plane equations are identical in form to the two-dimensional global response matrix equation, and are thus solved using the iteration shown in Eq. (4.9). As in two dimensions, the number (Ml_g) of iterations performed on the hex-plane is calculated using Eq. (4.11).

In summary, the three-dimensional response matrix equations are solved using $M2_g(\equiv 2)$ axial mesh sweeps in which first the odd-numbered planes and then the even-numbered planes are processed during each sweep. The hex-plane partial currents are computed using Ml_g (typically 2) four-color checkerboard sweeps on each plane, while the outgoing axial partial currents for the plane are computed using a single (sequential) sweep of the nodes on the plane.

4.3 Coarse-Mesh Rebalance Acceleration of the Outer Iterations

The outer (fission source) iterations are accelerated using the well-known coarse-mesh rebalance method[21,22] in combination with the asymptotic source extrapolation technique discussed in Section 4.4. Coarse-mesh rebalance has proven to be an effective means of accelerating the convergence of iterative schemes encountered in the solution of the neutron transport, neutron diffusion, and fluid dynamics problems. The basic idea of the method is to scale the fluxes calculated at each outer iteration on the "fine-mesh" by rebalance factors computed such that a neutron balance is enforced over each cell (region) of a "coarse-mesh" super-imposed on the fine mesh. This approach is nonlinear since the fine mesh fluxes are used to compute the coefficients of the coarse-mesh equations.

4.3.1 Construction of the Coarse-Mesh Equations

The rebalance equations are constructed on a mesh defined such that each ring of hexagons forms a coarse-mesh region in the hex-plane (see Fig. 4.3) and each fine-mesh plane is assigned to an axial coarse-mesh region comprised of one or more adjacent fine-mesh planes. The coarse-mesh regions are denoted by V^m, $m = 1,\ldots,M$, where

$$M \equiv I \cdot J$$

$I \equiv$ number of rings of hexagons (including the central hexagon)

and

$J \equiv$ number of coarse-mesh rebalance intervals in the axial direction.

Typically 2 or 3 axial planes are combined to form a single axial coarse-mesh region. The use of rings of hexagons as hex-plane coarse-mesh regions simplifies both the construction of the coarse-mesh equations and their solution since, in two dimensions, these equations have the simple tri-diagonal structure of conventional one-dimensional finite difference equations.

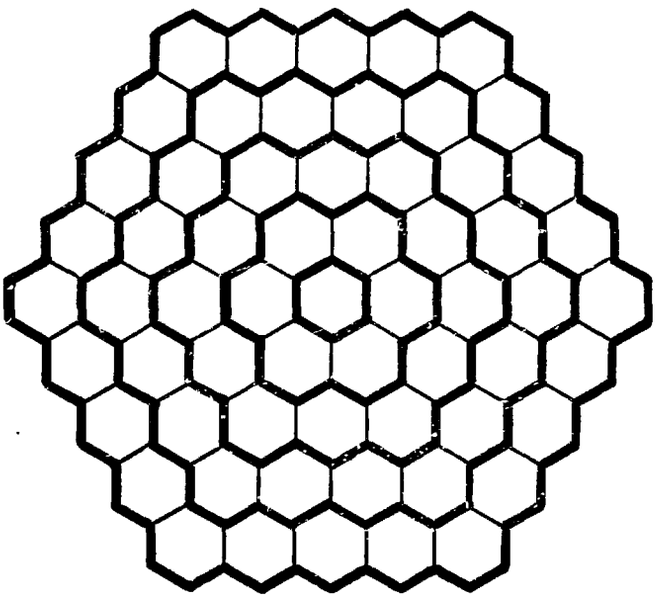

Fig. 4.3 Coarse-Mesh Rebalance Regions in the Hex-Plane

The rebalance equations are derived in the following manner. Using the nodal fluxes, interface partial currents, and eigenvalue computed at the n-th outer iteration, the following coarse-mesh balance equation is obtained by multiplying the three-dimensional nodal balance equation [(Eq. (3.1)] by V^k, and then summing the result over all nodes k contained in coarse-mesh region V^m and over all energy groups g:

$$-\sum_{\ell} J^{\ell\to m} + [\sum_{\ell} J^{m\to\ell} + A^m] = \frac{1}{\lambda^{(n)}} P^m, \quad m = 1,\ldots,M. \tag{4.16}$$

Here the integrated effective absorption rate and the integrated production rate for coarse-mesh cell m are

$$A^m \equiv \sum_{k\varepsilon V^m} V^k \sum_{g=1}^{G} \Sigma_g^{a,k} \bar{\phi}_g^{k(n)} \tag{4.17}$$

and

$$P^m \equiv \sum_{k\varepsilon V^m} V^k \sum_{g=1}^{G} \chi_g \sum_{g'}^{G} \nu\Sigma_{g'}^{f,k} \bar{\phi}_{g'}^{k(n)} \tag{4.18}$$

where the notation $k\varepsilon V^m$ implies all nodes k such the $V^k \varepsilon V^m$. The effective absorption cross section is defined by*

$$\Sigma_g^{a,k} \equiv \Sigma_g^{r,k} - \sum_{g'=1}^{G} \Sigma_{g'g}^{s,k} \quad , \tag{4.19}$$

where $\Sigma_{g'g}^{s,k}$ is the scattering cross section from group g to group g'. The quantity $J^{m\to\ell}$ represents the total neutron leakage from region m to its neighboring coarse-mesh region ℓ; the summations in Eq. (4.16) are over all such adjacent coarse-mesh regions. As shown in Fig. 4.3, each

*The "effective" absorption cross section defined in Eq. (4.19) is not necessarily equal to the "true" absorption cross section because the DIF3D scattering cross sections include contributions due to (n,2n) reactions.

coarse-mesh region (with the obvious exception of the central hexagon) imbedded in the reactor has two neighbors in two dimensions and four neighbors in three dimensions. The leakages are readily expressed in terms of the available face-averaged partial currents across the surface $S^{m\ell}$ common to coarse-mesh regions m and ℓ:

$$J^{m\to\ell} = \sum_{r_s \epsilon S^{m\ell}} S^k(r_s) \sum_{g=1}^{G} \bar{J}_g^{out,k(n)}(r_s), \qquad k \in V^m. \tag{4.20}$$

The notation here differs slightly from that used previously. $\bar{J}_g^{out,k}(r_s)$ is the face-averaged outgoing partial current from node k across a nodal surface (denoted by local coordinate r_s) which forms part of the surface $S^{m\ell}$, and $S^k(r_s)$ is the area of the nodal surface. The total leakage $J^{\ell\to m}$ is written in a similar manner in terms of outgoing partial currents from nodes in coarse-mesh region V^ℓ.

Equation (4.16) will not be satisfied if the outer iteration procedure is not converged because the fluxes and partial currents were calculated using a fission source from the previous iteration. We can, however, improve the solution (and hence the overall convergence rate of the outer iterations) by first defining the "rebalanced" solution

$$\left.\begin{aligned} \hat{\bar{\phi}}_g^{k(n)} &\equiv f^m \bar{\phi}_g^{k(n)} \\ \hat{\bar{J}}_g^{out,k(n)}(r_s) &\equiv f^m \bar{J}_g^{out,k(n)}(r_s) \end{aligned}\right\} \quad \begin{aligned} g &= 1,\ldots,G \qquad (4.21a) \\ k &\in V^m, \qquad (4.21b) \end{aligned}$$

and then calculating the rebalance factors f^m, m = 1,...,M such that the rebalance solution satisfies Eq. (4.16). The following eigenvalue equation for the rebalance factors is thus obtained:

$$-\sum_{\ell} J^{\ell\to m} f^\ell + \Big[\sum_{\ell} J^{m\to\ell} + A^m\Big] f^m = \frac{1}{\lambda} P^m f^m, \qquad m = 1,\ldots,M. \tag{4.22}$$

Equation (4.22) is solved for the rebalance factors and the new estimate for the eigenvalue as described in the following section. Note that the rebalance factors will approach 1 as the outer iterations converge.

4.3.2 Solution of the Coarse-Mesh Equations

The coarse-mesh equations represented by Eq. (4.22) can be combined in the form

$$[M]\underline{f} = \frac{1}{\lambda}[P]\underline{f} \ , \tag{4.23}$$

where

$$\underline{f} \equiv \text{col}\ [f^1,\ldots,f^M]$$

$$[P] \equiv \text{diag}\ [P^1,\ldots,P^M],$$

and the rebalance equations are ordered first by axial region and then by hex-plane region. Therefore, [M] has the following block tri-diagonal structure:

$$[M] \equiv \begin{bmatrix} [B_1] & [C_1] & & & & \\ [A_2] & [B_2] & [C_2] & & & \\ & [A_3] & [B_3] & [C_3] & & \\ & & \ddots & \ddots & \ddots & \\ & & & [A_I] & [B_I] \end{bmatrix} . \tag{4.24}$$

The entries of the diagonal matrices $[A_i]$ and $[C_i]$ involve the coarse-mesh leakages [Eq. (4.20)] in the hex-plane, while the off-diagonal entries of the tri-diagonal matrices $[B_i]$ involve leakages between adjacent axial coarse-mesh regions. These sub-matrices are square with dimension J, the number of coarse-mesh regions in the axial direction. The sub-matrices in Eq. (4.24) are reduced to scalar quantities in two-dimensional calculations.

Equation (4.23) is constructed and solved following each outer iteration. The solution to this eigenvalue problem can be obtained using either the power method[21] or the Wielandt method[21] of fractional iteration. For problems in which the [M] matrix can be inverted directly, the Wielandt method is often more efficient for reasons which will be discussed below. This approach is based on the application of the power method to the "shifted" eigenvalue problem obtained by rewriting Eq. (4.23) in the form

$$[\tilde{M}]\underline{f} = \frac{1}{\tilde{\lambda}} [P]\underline{f} \ , \tag{4.25}$$

where

$$[\tilde{M}] \equiv [M] - \frac{1}{\lambda_e} [P] \tag{4.26}$$

$$\frac{1}{\tilde{\lambda}} \equiv \frac{1}{\lambda} - \frac{1}{\lambda_e} \ , \tag{4.27}$$

and λ_e is an estimate for the fundamental-mode eigenvalue λ_o (k-effective) such that $\lambda_e > \lambda_o$. This estimate is calculated using

$$\lambda_e \equiv 1.05 \ \lambda^{(n-1)}, \tag{4.28}$$

where $\lambda^{(n-1)}$ is the rebalanced eigenvalue computed at the previous outer iteration. The convergence rate of the power method is determined by the dominance ratio* of the matrix $[M^{-1}][P]$; the closer this ratio is to 1, the slower the convergence rate. It can be shown that for $\lambda_e > \lambda_o$, the dominance ratio of $[\tilde{M}]^{-1}[P]$ is smaller than that of $[M]^{-1}[P]$. Hence the Wielandt method, which is obtained by applying the power method to Eq. (4.25), will converge faster than the power method applied directly to Eq. (4.23). We thus solve Eq. (4.25) using the following iterative procedure:

$$\underline{S}^{(t)} \equiv [\tilde{M}]^{-1}[P] \ \underline{f}^{(t-1)} \tag{4.29a}$$

$$\tilde{\lambda}^{(t)} = \frac{\|[P] \ \underline{S}^{(t)}\|_1}{\|[P] \ \underline{f}^{(t-1)}\|_1} \tag{4.29b}$$

$$\underline{f}^{(t)} = \frac{1}{\tilde{\lambda}^{(t)}} \underline{S}^{(t)} \ , \tag{4.29c}$$

---

*The dominance ratio of a matrix is defined by

$$\sigma \equiv \left| \frac{\lambda_1}{\lambda_o} \right| ,$$

where λ_o and λ_1 are, respectively, the largest and second largest eigenvalues of the matrix.

where t is the coarse-mesh iteration index and $\|\cdot\|_1$ denotes the L_1 vector norm. The indicated matrix inversion is performed using a direct matrix factorization technique[21] based on the block tri-diagonal structure of [M]. The factorization is performed prior to the start of the coarse-mesh iterations; a forward elimination, backward substitution procedure is then used to compute the rebalance factors at each coarse-mesh iteration. A fixed (user-specified) number of coarse-mesh iterations are performed at each outer iteration. Numerical calculations to date have demonstrated that due to the efficiency of the Wielandt method, only two coarse-mesh iterations are required at each outer iteration.

The computed rebalance factors are used to scale the partial currents and fission source moments in accordance with Eqs. (4.21):

$$\hat{\underline{J}}_g^{out,k(n)} \equiv f^m \, \underline{J}_g^{out,k(n)} \tag{4.30a}$$

$$\hat{\underline{\Psi}}^{k(n)} \equiv f^m \, \underline{\Psi}^{k(n)}, \qquad k \in V^m. \tag{4.30b}$$

The fission source is scaled prior to checking the convergence of the fission source (see Fig. 4.1), while the group partial currents are scaled at the beginning of the loop over groups in the next outer iteration in order to avoid an additional group loop following the rebalance procedure. (It is not necessary to scale the flux moments $\underline{\phi}_g^{k(n)}$ because, as shown in Eq. (4.1), they do not enter into the calculation of the group source term $\underline{Q}_g^{k(n+1)}$ if there is no up-scatter). The final estimate for the eigenvalue at the n-th outer iteration is obtained from Eq. (4.27)

$$\frac{1}{\lambda^{(n)}} = \frac{1}{\tilde{\lambda}} + \frac{1}{\lambda_e},$$

where $\tilde{\lambda}$ is the final iterate computed during the coarse-mesh iterations.

4.4 Acceleration of the Outer Iterations Using Asymptotic Extrapolation

The outer iterations are also accelerated using an asymptotic source extrapolation procedure similar to that described in Ref. 23. This procedure is based on the assumption that the fission source converges to the exact (fully converged) solution $\underline{\Psi}^{(\infty)}$ with the asymptotic behavior

$$\underline{\Psi}^{(\infty)} = \underline{\Psi}^{(n)} + \underline{R} \, \sigma^n, \tag{4.32}$$

where $\underline{\Psi}$ is the global fission source vector containing the node-averaged fission sources for all nodes, n is the outer iteration index, σ is the dominance ratio (see footnote in Section 4.3.2) and $\underline{R}$ is an unknown vector. The vector $\underline{\Psi}^{(n)}$ is constructed using the rebalanced fission source [Eq. (4.30b)] computed at the end of the n-th outer iteration. An estimate for the dominance ratio can be calculated in a manner consistent with Eq. (4.32):

$$\tilde{\sigma}^{(n)} = \frac{\| \underline{\Psi}^{(n)} - \underline{\Psi}^{(n-1)} \|_2}{\| \underline{\Psi}^{(n-1)} - \underline{\Psi}^{(n-2)} \|_2} , \tag{4.33}$$

where $\| \cdot \|_2$ denotes the L_2 vector norm. Given the assumed asymptotic behavior shown in Eq. (4.32), an improved estimate $\hat{\underline{\Psi}}^{(n)}$ is

$$\hat{\underline{\Psi}}^{(n)} = \underline{\Psi}^{(n)} + \omega^{(n)} [\underline{\Psi}^{(n)} - \underline{\Psi}^{(n-1)}], \tag{4.34}$$

where

$$\omega^{(n)} \equiv \frac{\tilde{\sigma}^{(n)}}{1 - \tilde{\sigma}^{(n)}} . \tag{4.35}$$

The extrapolation shown in Eq. (4.34) is applied only when asymptotic behavior is observed, as determined by the criterion

$$\min [\varepsilon_\omega^{(n)}, \varepsilon_\omega^{(n-1)}] < 0.1, \tag{4.36}$$

where

$$\varepsilon_\omega^{(n)} \equiv \left| \frac{\omega^{(n)} - \omega^{(n-1)}}{\omega^{(n)}} \right| . \tag{4.37}$$

An additional criterion which must also be satisfied prior to extrapolation is

$$n - n^* > 5, \tag{4.38}$$

where n^* denotes the outer iteration at which the most recent extrapolation was performed.

The convergence of the fission source is checked following the rebalance step as shown in Fig. 4.1. If Eqs. (4.36) and (4.38) are satisfied, the fission source moments and interface partial currents are extrapolated in accordance with Eq. (4.34):

$$\left.\begin{aligned} \hat{\underline{\psi}}^{k(n)} &= \underline{\psi}^{k(n)} + \omega^{(n)} \left[\underline{\psi}^{k(n)} - \underline{\psi}^{k(n-1)}\right] \\ \hat{\underline{J}}_g^{out,k(n)} &= \underline{J}_g^{out,k(n)} + \omega^{(n)} \left[\underline{J}_g^{out,k(n)} - \underline{J}_g^{out,k(n-1)}\right], \quad g = 1,\ldots,G \end{aligned}\right\} \; k=1,\ldots,K \quad . \quad (4.39)$$

As with the rebalance scaling of the partial currents shown in Eq. (4.30b), these operations are performed during the following outer iteration. The rebalance factors are applied prior to the extrapolation, and thus the vectors appearing on the right hand side of Eq. (4.39) are the most recent rebalanced solutions.

4.5 On the Computational Efficiency of the Nodal Scheme

DIF3D finite difference calculations are typically performed using 6 triangular mesh cells per hexagonal fuel assembly and 3 axial mesh planes per axial burnup region, for a total of 18 flux unknowns per group per hexagonal-z cell defined by the axial burnup boundaries. As will be shown in the following section, the accuracy of the nodal scheme permits the use of a single mesh plane per axial burnup region. The nodal option thus involves a total of 13 principal unknowns per group for this same hexagonal-z cell. Numerical results given in the following section demonstrate that in spite of the similar numbers of unknowns involved in the two schemes, the nodal option runs approximately 8 times faster than the finite difference option. This rather surprising improvement in efficiency can be attributed to differences in the two solution algorithms. The nodal solution procedure described in Sections 4.1 and 4.2 requires the recalculation of a total of 32 partial currents and flux moments per node per group per outer iteration. A typical finite difference calculation using an average of 12 inner iterations per group requires calculation of a total of $12 \times 18 = 216$ fluxes per coarse-mesh cell (node) per outer iteration. Thus, measured in terms of the more meaningful number of total unknowns computed during an outer iteration, the nodal option offers a potential increase in efficiency by a factor of $216/32 \cong 6.5$. Although the actual improvement obviously depends on additional factors such as the CPU time necessary to compute an unknown and the total number of outer iterations, this predicted ratio is consistent with that observed in the numerical comparisons given in the following section.

5. SAMPLE NUMERICAL CALCULATIONS

Numerical results are presented in this section for two computational benchmark problems representing a 300 MWe homogeneous-core LMFBR and a 1000 MWe heterogeneous-core design. Both problems are analyzed in two and three dimensions. Nodal and finite difference results are compared in terms of the accuracy of the respective spatial approximations and the computational effort required to achieve this accuracy. The accuracy is measured by the errors with respect to a spatially-converged solution of the multigroup neutron diffusion equation, while the computational effort is reflected by the central processor unit (CPU) time. In particular, we are interested in the error in the computed value of k-effective,

$$\varepsilon_k(\%) \equiv 100 \frac{k_{eff} - k_{eff}^{ref}}{k_{eff}^{ref}},$$

as well as the errors in the flux and/or power density averaged over specified regions of the reactor. The reference solution (e.g. k_{eff}^{ref}) is calculated using Richardson extrapolation of the finite difference results, and is thus assumed to be the exact solution of the multigroup diffusion equation. All calculations were performed using the IBM 370/195 computer at Argonne National Laboratory (ANL) with the exception of the three-dimensional LCCEWG calculations, which were done on the ANL IBM 3033 computer. The CPU times on the 3033 are 35 to 50% larger than the 370/195 times for the same problem. All CPU times quoted here are for the calculation of the coupling coefficients and the outer iterations, and do not include the time required for input processing and solution edits.

5.1 The SNR Benchmark Problem

The SNR benchmark problem[24,25] is a 4-group model of a 300 MWe homogeneous-core LMFBR originally specified in both Cartesian and triangular geometry. The modified problem[25] solved here is obtained by altering the outer boundary of the triangular-geometry model (while preserving the volume of the core) to allow imposition of boundary conditions along surfaces of hexagons. The model consists of a two-zone core surrounded by radial and axial blankets without a reflector. The height of the active core is 95 cm, and each axial blanket is 40 cm thick. A total of 11 rings of hexagons (including the central hexagon) are included in the model, with a lattice pitch of 11.2003 cm. Vacuum boundary conditions are imposed on the outer surfaces of the blankets. The full-core model includes a total of 18 control rods, with 6 of these rods parked at the core-upper axial blanket interface, and the remaining 12 rods inserted to the core midplane. All calculations were performed using sixth-core planar symmetry.

5.1.1 Two-Dimensional Results

The two-dimensional problem solved here corresponds to the original "rods in" configuration[24,25] representing a horizontal slice taken through the upper half of the core. The NH2, NH3, and NH4 approximation shown in Table 5.1 were obtained using the nodal option in DIF3D with N = 2,3,4 respectively in Eq. (2.33). The finite difference calculations used the indicated number of triangular mesh cells per hexagonal assembly. The nodal results demonstrate the improved accuracy of the NH4 scheme relative to the NH2 and NH3 approximations. With the exception of the average flux in the radial blanket, the NH4 results are considerably more accurate than the DIF3D(6Δ) results. In particular, the NH4 eigenvalue and average flux in the control rod are almost as accurate as the DIF3D(24Δ) results. Thus the accuracy of the NH4 approximation falls between that of the DIF3D(6Δ) and DIF3D(24Δ) results, with a reduction in CPU time by factors of 1.6 and 8.2 relative to the finite difference calculations.

Table 5.1 Summary of Results for the Two-Dimensional SNR Benchmark Problem*

Method	k-eff	ε_k(%)	ε_{IC}(%)	ε_{OC}(%)	ε_{RB}(%)	ε_{CR}(%)	CPU Time (sec)
DIF3D(NH2)	1.12753	0.34	-0.47	0.76	1.89	-1.51	0.8
DIF3D(NH3)	1.12683	0.27	-0.39	0.66	2.11	-0.96	0.8
DIF3D(NH4)	1.12529	0.14	-0.22	0.42	1.14	-0.44	0.9
DIF3D(6Δ)	1.12728	0.31	-0.42	0.72	0.83	-1.84	1.4
DIF3D(24Δ)	1.12475	0.09	-0.12	0.32	0.27	-0.51	7.4
Reference[a]	1.12375	--	--	--	--	--	--

*ε_{IC}, ε_{OC}, ε_{RB}, and ε_{CR} are the errors in the group- and region-averaged fluxes for the inner core, outer core, radial blanket, and control rod regions, respectively.

[a]The reference solution is obtained by Richardson extrapolation of DIF3D(24Δ) and DIF3D(96Δ) solutions.

5.1.2 Three-Dimensional Results

Results for the three-dimensional SNR benchmark problem are summarized in Table 5.2. The nodal calculations used the NH4 hex-plane approximation in combination with a cubic axial approximation [$N_Z \equiv 3$ in Eq. (3.29)]. The calculations with 8 and 18 axial mesh planes used 4 and 10 mesh planes, respectively, in the active core, and 2 and 4 mesh planes, respectively, in each axial blanket. Extrapolated results assuming an infinite number of axial mesh planes have been included in order to allow isolation of the errors due

to the axial approximations in the nodal and finite difference schemes. For example, these results show that the 0.16% eigenvalue error in the 8-plane nodal calculation involves contributions of 0.13% and 0.03% due to the hex-plane and axial approximations, respectively. (This hex-plane error is consistent with 0.12% error observed in the two-dimensional problem.) Similar analysis of the finite difference results shows that the axial contribution to the total eigenvalue error in the 18-plane and 36-plane calculations is 0.30% and 0.07 - 0.08%, respectively. Similar trends are observed in the flux errors, although there is some fortuitous cancellation of hex-plane and axial errors in the finite-difference results for the inner core and radial blanket. We conclude that the axial accuracy of the nodal scheme with 8 axial planes is superior to that of the finite difference approximation using 36 planes. Furthermore, although the overall accuracy of the 8-plane nodal calculation is superior to that of the 36-plane 6 triangles-per-hexagon finite difference results, the nodal calculation required a factor of 6 less computing time than this finite difference calculation.

Table 5.2 Summary of Results for the Three-Dimensional SNR Benchmark Problem[a]

Method	No. of Axial Planes	k-eff	ϵ_K(%)	ϵ_{IC}(%)	ϵ_{OC}(%)	ϵ_{RB}(%)	ϵ_{AB}(%)	ϵ_{CR}(%)	CPU Time (min)
DIF3D(NH4)	8	1.01150	0.16	-0.17	0.23	0.95	-0.30	-0.60	0.2
DIF3D(NH4)	18	1.01125	0.13	-0.18	0.22	0.96	-0.11	-0.44	0.6
DIF3D(NH4)	∞	1.01120	0.13	-0.18	0.22	0.96	-0.07	-0.39	--
DIF3D(6Δ)	18	1.01505	0.52	-0.18	0.52	0.22	-2.55	-2.56	0.6
DIF3D(6Δ)	36	1.01280	0.29	-0.27	0.42	0.47	-0.60	-1.72	1.6
DIF3D(6Δ)	∞	1.01205	0.22	-0.29	0.38	0.56	-0.06	-1.44	--
DIF3D(24Δ)	18	1.01342	0.35	-0.05	0.23	-0.20	-2.61	-1.48	3.1
DIF3D(24Δ)	36	1.01118	0.13	-0.04	0.13	0.05	-0.64	-0.64	6.0
DIF3D(24Δ)	∞	1.01043	0.05	-0.08	0.09	0.14	0.02	-0.36	--
Reference[a]	∞	1.00989	--	--	--	--	--	--	--

[a] ϵ_{IC}, ϵ_{OC}, ϵ_{RB}, ϵ_{AB}, and ϵ_{CR} are the errors in the group- and region-averaged fluxes for the inner core, outer core, radial blanket, axial blanket, and control rod regions, respectively.

[a] The reference solution is obtained by Richardson extrapolation of the DIF3D(6Δ) - 18 plane and DIF3D(24Δ) - 36 plane solutions.

5.2 The LCCEWG Benchmark Problem

The Large Core Code Evaluation Working Group (LCCEWG) benchmark problem[26] is a model of a 1000 MWe heterogeneous-core design with a lattice pitch of 16.33 cm. The core layout is shown in Figs. 5.1 and 5.2. Additional specifications for this problem are given in Ref. 27. Results summarized here include both beginning-of-life (BOL) and depletion calculations [using REBUS-3 (Ref. 5)] for two- and three-dimensional models with four energy groups. Detailed comparisons of 8-group BOL and depletion calculations using finite difference, nodal, and flux synthesis[4] neutronics solutions have been reported elsewhere.[27]

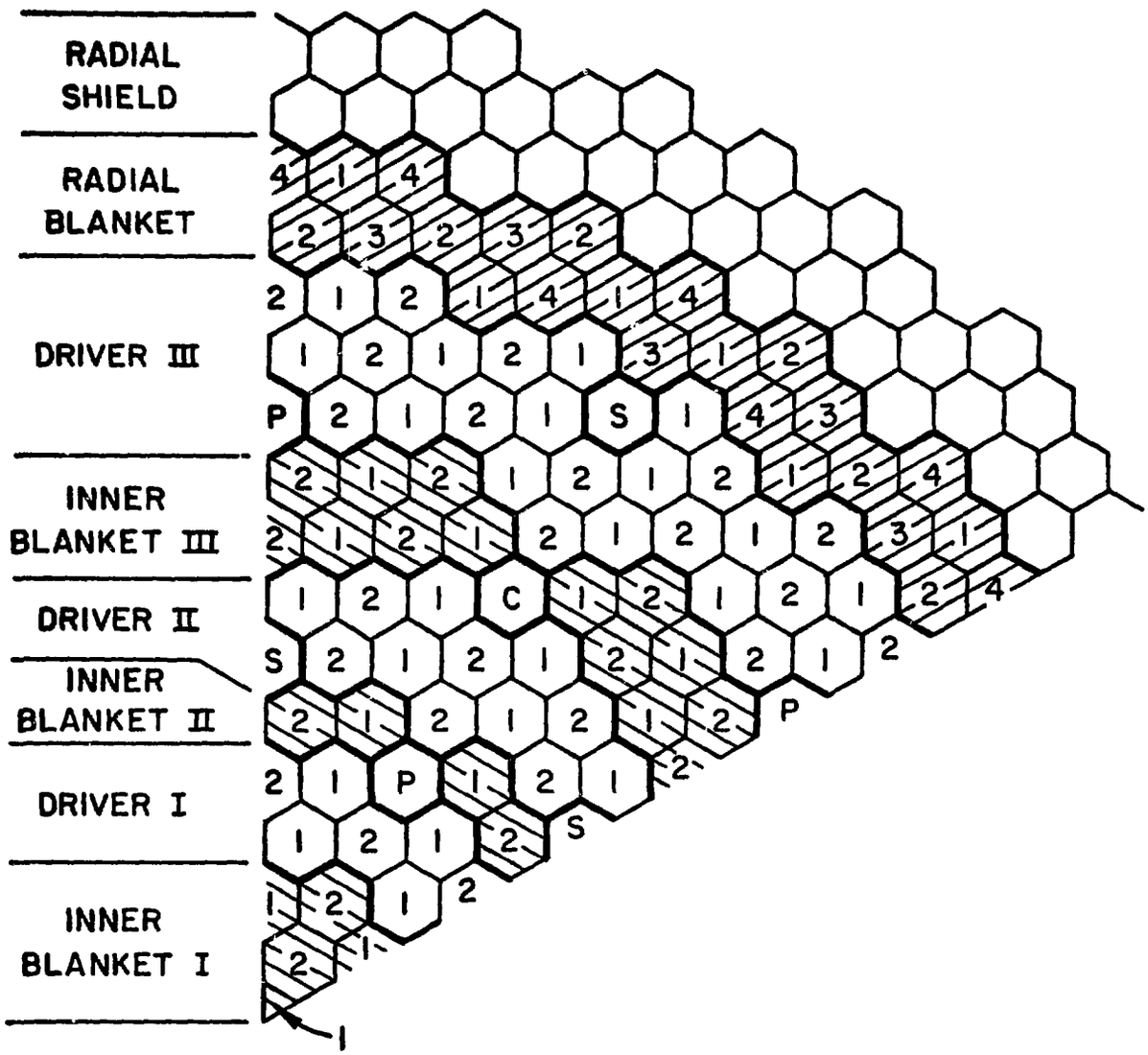

N BATCH LOADING SEQUENCE - ALL ASSEMBLIES LABELLED "N" ARE REPLACED AT THE END OF IRRADIATION CYCLE "N"

C PRIMARY CONTROL ROD USED FOR CRITICALITY ADJUSTMENTS DURING BURNUP

P PRIMARY CONTROL ROD

S SECONDARY CONTROL ROD

Fig. 5.1 Sixty-Degree Sector of the Core Layout for the LCCEWG Benchmark Problem

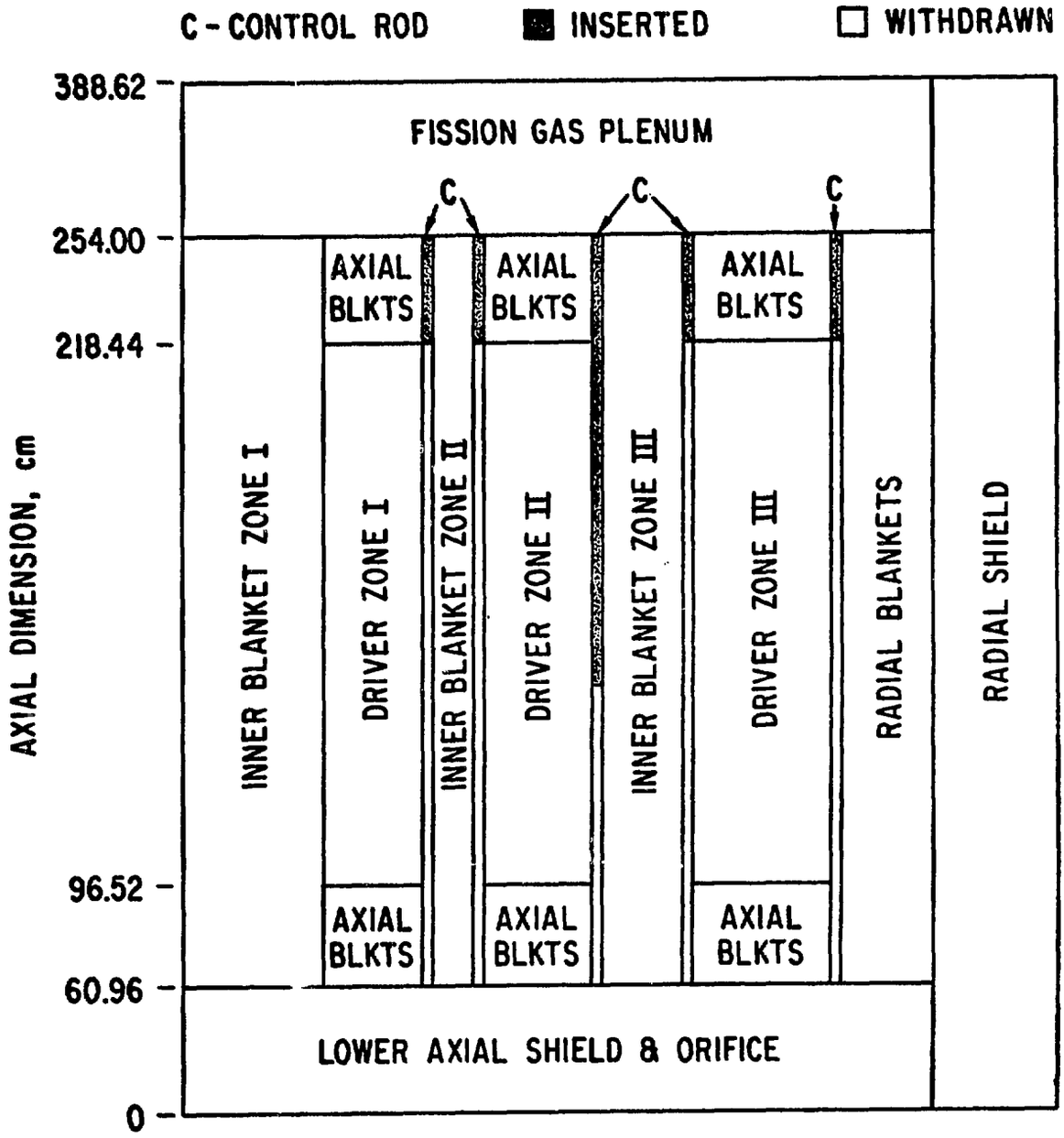

Fig. 3.2 Axial Dimensions for the LCCEWG Benchmark Problem

5.2.1 Two-Dimensional Results

Table 5.3 summarizes BOL results for the two-dimensional version of the LCCEWG benchmark problem. The regions used in computing the errors are defined by the zones shown in Fig. 5.1; thus there are three driver-fuel regions, three inner-blanket regions, and one radial blanket region. The average error in the driver fuel, for example, is calculated by averaging the errors over the three fuel regions. The nodal results demonstrate that the NH4 approximation is necessary in order to achieve acceptable accuracy in the blankets. Although the NH4 error in the driver fuel is slightly higher than the DIF3D(6Δ) error, the NH4 results for k-effective and the power densities in the blankets are significantly better than the DIF3D(6Δ) results. This improved accuracy is obtained with a reduction in computing time by a factor of 2.5 relative to the DIF3D(6Δ) approximation.

Table 5.3 Summary of BOL Results for the Two-Dimensional LCCEWG Benchmark Problem*

Method	k-eff	ϵ_k(%)	$\bar{\epsilon}_{DF}$(%)	$\bar{\epsilon}_{IB}$(%)	$\bar{\epsilon}_{RB}$(%)	CPU Time (sec)
DIF3D(NH2)	1.01064	0.08	1.54	7.53	3.13	1.9
DIF3D(NH3)	1.00957	-0.02	1.55	6.37	2.33	2.0
DIF3D(NH4)	1.01002	0.02	0.82	2.96	0.98	2.0
DIF3D(6Δ)	1.01323	0.34	0.69	5.50	3.31	4.9
DIF3D(24Δ)	1.01048	0.07	0.15	1.23	0.63	22.3
Reference[a]	1.00980	--	--	--	--	--

*$\bar{\epsilon}_{DF}$, $\bar{\epsilon}_{IB}$, and $\bar{\epsilon}_{RB}$ are the average errors in the region-averaged power densities over all regions contained in the driver fuel, internal blankets, and radial blanket, respectively.

[a]The reference solution is obtained by Richardson extrapolation of DIF3D(24Δ) and DIF3D(96Δ) solutions.

Depletion results[28] for the two-dimensional model are summarized in Table 5.4. The reactivity swings due to burnup over two non-equilibrium cycles are shown as well as average burnups and breeding ratios computed at the end of cycle 1 (EOC1). The average inner-blanket burnups computed using the NH4 approximation are more accurate than the DIF3D(6Δ) results, while the nodal burnup swings are as accurate as those computed using the DIF3D(24Δ) option. It is clear that the improved inner-blanket burnups are a direct consequence of the reduced inner-blanket errors shown in Table 5.3. The improved inner-blanket solutions, in combination with the accuracy of the eigenvalues computed using the nodal option, lead to very accurate predictions of the reactivity swing due to burnup.

Table 5.4 Summary of Depletion Results for the Two-Dimensional LCCEWG Benchmark Problem

	DIF3D(NH4)	DIF3D(6Δ)	DIF3D(24Δ)	DIF3D(96Δ)
k_{eff}(BOC1) - k_{eff}(EOC1)	0.0203	0.0219	0.0207	0.0205
k_{eff}(BOC2) - k_{eff}(EOC2)	0.0169	0.0179	0.0169	0.0166
EOC1				
Average Burnup (MWd/MT)				
Inner Core	2.99+4	2.99+4	3.01+4	3.01+4
Middle Core	3.11+4	3.12+4	3.12+4	3.13+4
Outer Core	2.68+4	2.67+4	2.67+4	2.66+4
Inner Blanket	2.05+3	2.00+3	2.08+3	2.10+3
Middle Blanket	4.94+3	4.79+3	4.98+3	5.04+3
Outer Blanket	3.12+3	3.05+3	3.15+3	3.17+3
Breeding Ratio	1.326	1.319	1.323	1.324

5.2.2 Three-Dimensional Results

Table 5.5 summarizes results for the three-dimensional LCCEWG problem. The average errors are calculated by averaging the errors for regions defined in the hex-plane by the zones shown in Fig. 5.1 and in the axial direction by the axial burnup regions. A total of 12 axial burnup regions are defined by 8 uniform (15.24 cm) axial mesh intervals in the active core and 2 uniform (17.78 cm) intervals in each axial blanket. The 14-plane nodal calculation used a single mesh plane per axial burnup region plus one additional mesh plane each in the lower axial shield and the fission gas plenum. The 28-plane and 56-plane meshes are defined by uniform refinement of the 14-plane mesh.

As for the three-dimensional SNR benchmark problem, results assuming an infinite number of axial planes are given in Table 5.5. Using these extrapolated results, it can be seen that the errors in eigenvalue due to the axial approximation are greater in the 56-plane finite difference calculations than in the 14-plane nodal calculation. Comparison of the 14-plane nodal and 56-plane DIF3D(6Δ) calculations shows that the nodal option produces somewhat larger (but very acceptable) errors in the driver fuel, but yields significantly smaller errors in eigenvalue and in the inner and radial blankets. The larger errors in the fuel may be due to the flat approximation [Eq. (3.61)] to the axial leakage. The increasing errors with decreasing axial mesh spacing observed in the nodal results for the driver fuel and inner blankets are not understood, although it is likely that this behavior is due to a fortuitous cancellation of hex-plane and axial errors and/or uncertainties in the reference solution. The nodal eigenvalue error is considerably larger than for the two-dimensional version of this problem. Again, this is in part due to the flat leakage approximation, but may also reflect the larger flux gradients in the three-dimensional model due to partially-inserted control rods. (The control rods are withdrawn in the two-dimensional model). Although

the overall accuracy of the 14-plane nodal calculation is superior to that of the 56-plane DIF3D(6Δ) calculation, the nodal calculation required a factor of 9 less computing time.

Table 5.5 Summary of BOL Results for the Three-Dimensional LCCEWG Benchmark Problem*

Method	No. of Axial Planes	k-eff	ϵ_k(%)	$\bar{\epsilon}_{DF}$(%)	$\bar{\epsilon}_{IB}$(%)	$\bar{\epsilon}_{RB}$(%)	$\bar{\epsilon}_{AB}$(%)	CPU Time (min)
DIF3D(NH4)	14	0.99846	0.15	1.4	3.1	0.8	2.3	1.1
DIF3D(NH4)	28	0.99829	0.13	1.6	3.2	0.7	1.6	2.5
DIF3D(NH4)	∞	0.99820	0.12	1.6	3.2	0.7	1.5	--
DIF3D(6Δ)	28	1.00329	0.63	0.8	4.2	3.4	5.3	5.3
DIF3D(6Δ)	56	1.00206	0.51	0.7	4.4	3.1	2.1	10.2
DIF3D(6Δ)	∞	1.00165	0.47	0.7	4.4	3.0	1.0	--
DIF3D(24Δ)	28	0.99978	0.28	0.5	1.1	1.3	4.9	30.5
DIF3D(24Δ)	56	0.99855	0.16	0.2	1.1	0.8	1.3	59.0
DIF3D(24Δ)	∞	0.99814	0.11	0.1	1.1	0.6	0.1	--
Reference[a]	∞	0.99697	--	--	--	--	--	--

*$\bar{\epsilon}_{DF}$, $\bar{\epsilon}_{IB}$, $\bar{\epsilon}_{RB}$, and $\bar{\epsilon}_{AB}$ are the average errors in the region-averaged power densities over all regions contained in the driver fuel, inner blankets, radial blanket, and axial blankets, respectively.

[a]The reference solution is obtained by Richardson extrapolation of the DIF3D(6Δ) - 28 plane and DIF3D(24Δ) - 56 plane solutions.

Table 5.6 summarizes computed burnup swings over the first half of a 388.5 day cycle. The burnup swing computed using the nodal option is very accurate as shown by the excellent agreement with the DIF3D(24Δ) result. Thus, as in two dimensions, the improved accuracy of the eigenvalues and blanket fluxes computed with the nodal option leads to significantly improved predictions of the reactivity swing due to burnup.

Table 5.6 Computed Burnup Swings for the Three-Dimensional LCCEWG Benchmark Problem*

Method	Number of Axial Planes	Burnup Swing (Δk)	Neutronics CPU Time (min)
DIF3D(NH4)	17	-0.00426	2.6
DIF3D(6Δ)	42	-0.00489	14.0
DIF3D(24Δ)	42	-0.00420	81.1

*Over the first half of a 388.5 day cycle.

From a practical viewpoint, the total dollar cost is an important measure of the computational efficiency of any numerical scheme proposed for the solution of large-scale reactor physics problems. The job cost typically includes contributions due to core storage and I/O activity in addition to the CPU time. Of course, the weights assigned to these contributions vary from one installation to another. Table 5.7 shows the core storage requirements, EXCP total (which is a measure of I/O activity), and dollar cost at ANL of several calculations for the three dimensional LCCEWG problem. The nodal storage requirements shown in Table 5.7 include the storage necessary for all coupling coefficients required during the depletion calculation. The reduced storage requirements for the nodal option are due primarily to the need to store coupling coefficients only for unique nodes as described in Section 3.5. The nodal calculation was run with all data for one energy group in core, while the finite difference calculations core-contained only a fraction of this data in an effort to reduce the total job cost. Thus the nodal EXCP count is significantly smaller. This reduced I/O activity, in combination with the smaller core storage requirements for the nodal option, leads to even greater reductions in dollar cost than those already observed in CPU time. For example, relative to the DIF3D(6Δ) calculation with 56 planes, the nodal calculation required a factor of 9 less CPU time with a reduction in dollar cost by a factor of nearly 12.

Table 5.7 Summary of Execution Statistics for the Three-Dimensional LCCEWG Problem*

Method	No. of Axial Planes	L_1	L_2	L_3	CPU Time (min)	EXCP Total ($\times 10^{-3}$)	Cost($)
DIF3D(NH4)	14	116	215	116	1.1	3.6	7.28
DIF3D(6Δ)	28	297	852	223	5.3	30.1	43.14
DIF3D(6Δ)	56	589	1693	215	10.2	65.4	85.27
DIF3D(24Δ)	28	1188	3412	340	30.5	292.5	336.72

*BOL configuration, 4 energy groups. The core storage does not include the storage required by the DIF3D load module.

L_1 ≡ core storage [K-(REAL*8) words] required to contain all data for one group.

L_2 ≡ core storage [K-(REAL*8) words] required to contain all data for all groups.

L_3 ≡ core storage [K-(REAL*8) words] actually used.

5.3 Calculations of Peak Power Densities

The accurate calculation of peak power densities using a nodal formulation is limited by the lack of information concerning the spatial distribution of the flux within the node. A simple procedure is used in the nodal option to compute more accurate peak power densities than those obtained by sampling only the available node-averaged values. The peak values are computed in two-dimensional problems by sampling both the surface-averaged and node-averaged values of the power density. This scheme is extended to three dimensions by assuming the flux is separable in the hex-plane and axial directions. Additional details of this procedure are provided in Appendix D.

Peak power densities calculated for the three-dimensional SNR benchmark problem are shown in Table 5.8. The finite-difference peak values are computed by sampling both the surface and cell-centered values of the power density. The surface values are obtained in a manner consistent with the mesh-centered finite difference formulation in DIF3D. The nodal results calculated using 8 axial planes agree with the reference solution to within 1.0%. Although the procedure used to compute peak values in the nodal option is particularly simple, the results in Table 5.8 demonstrate that the accuracy of this scheme is comparable to that achieved in fine-mesh finite difference calculations.

Table 5.8 Computed Peak Power Densities for the Three-Dimensional SNR Benchmark Problem*

Method	No. of Axial Planes	Peak Power Densities (watts/cm^3)			
		Inner Core	Outer Core	Radial Blanket	Axial Blanket
DIF3D(NH4)	8	3.031-6	2.896-6	2.683-7	1.754-7
DIF3D(NH4)	18	3.030-6	2.907-6	2.678-7	1.758-7
DIF3D(6Δ)	18	3.010-6	2.890-6	2.633-7	1.789-7
DIF3D(6Δ)	36	3.019-6	2.900-6	2.650-7	1.763-7
DIF3D(24Δ)	18	3.030-6	2.892-6	2.635-7	1.804-7
DIF3D(24Δ)	36	3.040-6	2.903-6	2.652-7	1.777-7
Reference[a]	∞	3.05 -6	2.90 -6	2.66 -7	1.77 -7

*The power densities are normalized to a total power of 1 watt over the third-core model.

[a]The reference solution is obtained by approximate extrapolation of the finite difference results.

5.4 Overview of the Numerical Results

The results presented in this section have shown the accuracy of the nodal scheme to be superior to that of the standard DIF3D finite difference option using six triangular mesh cells per hexagonal fuel assembly. For three-dimensonal calculations, the higher-order axial approximation in the nodal scheme permits the use of an axial mesh which is at least 4 times coarser than that used in a typical finite difference calculation. Particular improvement is seen in the average fluxes in the blanket region (where the largest finite difference errors typically occur) and in the computed values for k-effective. This enhanced accuracy leads in turn to more accurate predictions of inner blanket burnups, breeding ratios, and burnup reactivity swings.

Relative to the standard finite difference option, the improved accuracy of the nodal option is obtained in CPU times which are roughly 2 times smaller in two-dimensional applications and 8-10 times smaller in three-dimensional calculations. The reduced storage requirements for the nodal option can lead to even greater reductions in the total cost of a calculation. Thus, in

summary, the superior axial accuracy of the nodal scheme permits the use of a single axial mesh point per axial burnup region with a potential order-of-magnitude cost reduction relative to the standard DIF3D neutronics option. Although less dramatic cost reductions are obtained relative to the flux synthesis module SYN3D (Ref. 4), the nodal option most likely will supercede the flux synthesis option due to its increased accuracy and ease of use.

6. USER INFORMATION

The nodal option in DIF3D is executed in essentially the same manner as the standard finite difference option. This section highlights information of particular interest to users of the nodal option, and is thus intended to supplement the detailed documentation provided in Section 3 of Ref. 3 and in the descriptions of the BCD input files.

6.1 Code-Dependent Input - A.DIF3D

Calculational parameters, storage containers, and edit sentinels are specified via the BCD input file A.DIF3D. A description of this file is given in Appendix E. The edit sentinels on card type 04 and the convergence criteria on card type 05 are directly applicable to the nodal option.* The only entry on card type 06 which is used in the nodal option is the steady-state reactor power in columns 49-60. A.DIF3D card types 07, 08, and 09 are not relevant to the nodal option.

6.1.1 Data Management Options and Container Sizes - A.DIF3D Card Type 02

DIF3D uses the BPOINTER package[29] to manage the dynamic allocation of all variably-dimensioned arrays used in the code. These arrays are actually stored in two large blocks of workspace called container arrays. The lengths of the container arrays are specified on card type 02 of A.DIF3D. The FCM (fast core memory) container is stored in fast core memory on both one-level (e.g. IBM 370) and two-level (CDC 7600) computers. The ECM (extended core memory) container is in fast core memory on one-level computers and in large core memory (LCM) on two-level computers.

The specification of the FCM container length for the nodal option is straightforward. On one-level machines, a relatively small allocation (e.g. 10,000 words) is sufficient since only small arrays are stored in this container. On two-level computers such as the CDC 7600 computer, the length of the FCM container should be specified as the maximum number of words available in the small core memory. The number of FCM words actually used is given in the data management edit which appears immediately before the outer iteration history in the DIF3D output. A sample data management edit is shown in Fig. 6.1.

The length of the ECM container array determines the locations of the files shown in Fig. 6.1. The minimum ECM container length is given by the storage necessary to core-contain the group-independent files (e.g. fission source moments, composition map) plus 1-group ECM buffers for the group-dependent files stored on disk. Any additional available storage is used to

---

*Peak power densities and peak total fluxes included in the DIF3D edits are computed using the procedure described in Appendix D. The peak values are written on an interface file PKEDIT which, in the ANL modular version of DIF3D, is processed by the SUMMARY module.[3]

*** DIF3D (NODAL OPTION) STORAGE ALLOCATION ***

		FCM	ECM
NUMBER OF WORDS IN DATA STORAGE CONTAINER	=	6000	177000
MINIMUM NUMBER OF WORDS REQUIRED TO RUN THIS PROBLEM			
WITH ALL DATA FOR 1 GROUP IN CORE	=	5991	112319
WITH SCATTERING BAND OF FLUXES IN CORE	=	5991	176008
WITH ALL FILES IN CORE (DURING OUTER ITERATIONS)	=	5991	943664
WITH ALL FILES IN CORE (DURING EDIT OVERLAY)	=	5991	1032375

LOCATION OF SCRATCH FILES DURING OUTER ITERATIONS

FILE CONTENTS	NO. OF RECORDS	RECORD LENGTH	FILE LENGTH	LOCATION	RECORDS IN CORE
FLUX MOMENTS	20	10205	204100	DISK	11
NEW HEX-PLANE PARTIAL CURRENTS	20	12896	257920	DISK	1
NEW AXIAL PARTIAL CURRENTS	20	4396	87920	DISK	1
OLD HEX-PLANE PARTIAL CURRENTS	20	12896	257920	DISK	1
OLD AXIAL PARTIAL CURRENTS	20	4396	87920	DISK	1
CROSS SECTIONS	20	361	7220	DISK	1
NODAL COUPLING COEFFICIENTS	20	624	12480	DISK	1

LOCATION OF SCRATCH FILES DURING EDIT OVERLAY

FILE CONTENTS	NO. OF RECORDS	RECORD LENGTH	FILE LENGTH	LOCATION	RECORDS IN CORE
NODE-AVERAGE FLUXES	20	2197	43940	CORE	20
FLUX SHAPE COEFFICIENTS	20	18369	367380	DISK	1
FLUX MOMENTS	20	10205	204100	DISK	1
NEW HEX-PLANE PARTIAL CURRENTS	20	12896	257920	DISK	1
NEW AXIAL PARTIAL CURRENTS	20	4396	87920	DISK	1

TOTAL NUMBER OF WORDS USED FOR THIS PROBLEM	=	5991	176008

Fig. 6.1 Sample Data Management Edit for the Nodal Option

core-contain the scattering band of fluxes followed by as many of the group-dependent files shown in Fig. 6.1 as possible. Separate data management strategies are used during the outer iterations and in the edit overlay. Details of these strategies are given in Section 7.2.

The optimal choice of data management strategy (and thus the specification of the ECM container length) depends upon the relative weights assigned to core storage and I/O activity in computing job costs at a particular installation. Experience at ANL suggests that two-dimensional problems should be run using the container array sizes for all data in core during the edit overlay. The job cost for three-dimensional calculations at ANL is generally minimized when the scattering band of fluxes is core-contained. Note that the sample three-dimensional problem shown in Fig. 6.1 was run using this data management mode.

Execution is terminated immediately following the edit of the data management information if the minimum required storage exceeds the container lengths specified on A.DIF3D card type 02. The user can thus specify relatively small container arrays for the purpose of obtaining the data management edit, and then use the information in this edit to specify the appropriate container sizes for a subsequent run.

6.1.2 Nodal Option Parameters - A.DIF3D Card Type 10

The parameters for the nodal option are specified on card type 10 as shown in Appendix E. It is strongly recommended that the default values for these parameters be used.

6.1.3 Axial Coarse-Mesh Rebalance Boundaries - A.DIF3D Card Type 11

The coarse-mesh rebalance acceleration described in Section 4.3 requires specification of the axial boundaries which define the rebalance mesh. The choice of these boundaries represents a trade-off between the decreased number of outer iterations obtained with a relatively large number of axial rebalance regions and the increased computational overhead required for the solution of the rebalance equations. It is recommended that an axial rebalance mesh no greater than 35 cm be specified in the active core and axial blankets. In general, it is better to use a relatively fine axial rebalance mesh since any reduction in the number of outer iterations typically offsets the additional CPU time required for the solution of the increased number of rebalance equations. It is also important that the axial rebalance mesh be as uniform as possible since specification of adjacent rebalance regions with very different axial dimensions can cause the outer iterations to diverge.

6.2 Geometry Input - A.NIP3

The geometry of the computational model is described via the BCD input file A.NIP3. The card types discussed in the following sub-sections may require attention when using the nodal option. Descriptions of these card types are given in Appendix F.

6.2.1 Problem Geometry Specification - A.NIP3 Card Type 03

The nodal option is invoked by the following geometry-type sentinels:

110	Hexagonal,	Full Core
114	Hexagonal,	Sixth Core Symmetry
116	Hexagonal,	Third Core Symmetry
120	Hexagonal-z,	Full Core in Plane
124	Hexagonal-z,	Sixth Core Symmetry in Plane
126	Hexagonal-z,	Third Core Symmetry in Plane

6.2.2 External Boundary Conditions - A.NIP3 Card Type 04

The nodal option does not treat reflectional symmetry in the plane; all fractional-core models must be specified using rotational (periodic) symmetry boundary conditions in the hex-plane. Thus, when geometry types 114, 116, 124, or 126 are specified on card type 03, boundary condition type 7 must be specified in columns 13-18 of card type 04.

A single boundary condition type is imposed on all surfaces forming part of the outer reactor boundary in the hex-plane. This boundary-condition type is selected from appropriate external boundary conditions (i.e. either zero flux or extrapolated boundary conditions) specified in the x- and y-directions. Thus, consistent with obvious physical considerations, only one boundary condition type should be specified on the outer reactor boundary in the hex-plane.

6.2.3 Variable-Mesh Structure - A.NIP3 Card Type 09

As in the triangular-geometry models, the axial mesh spacings for hexagonal-z models are specified on card type 09. Results given in Section 5 have shown that the higher-order axial approximation in the nodal scheme permits the use of an axial mesh which is at least 4 times coarser than the 5 cm axial mesh typically used in finite difference calculations. For most burnup (REBUS-3) calculations, the axial mesh structure should coincide with the axial region assignments on the A.NIP3 type 30 cards.

6.2.4 Location of Regions - A.NIP3 Card Type 30

Hexagons are assigned to regions via the A.NIP3 type 30 cards described in Appendix F. Note that the hexagonal-geometry solution domains for sixth- and third-core symmetries are rotated 30 degrees from the respective domains used in the DIF3D triangular-geometry models. A special procedure has been implemented in the input processor GNIP4C (Ref. 3) to facilitate conversion of existing type 30 cards for most (but not all) finite difference models to those required for the nodal option. When hexagonal geometry and periodic boundary conditions are specified, GNIP4C will use the periodicity (rotational symmetry) to assign hexagons not referenced on type 30 cards (but included in the hexagonal-geometry solution domain) to appropriate regions. The procedure requires that the hexagons bisected by the triangular-geometry

fractional-core symmetry lines be assigned to regions in a manner consistent with rotationally symmetric boundary conditions. (Recall from the discussion in Section 6.2.2 that the nodal option treats only rotational symmetry in the plane). Thus, if the original triangular-geometry model was constructed using boundary conditions type 3 (reflectional symmetry) on A.NIP3 card type 04, the user must make certain that the region assignments are also consistent with the rotational symmetry assumed in mapping the triangular-geometry model to the hexagonal-geometry model. As an example, consider the following free-format A.NIP3 cards included in a finite difference deck:

```
03    70
04    3 2 3 2
30    REG1 3 2
30    REG2 3 12    .
```

The required specifications for the nodal option are

```
03    114
04    7 2 0 2
30    REG1 3 2
30    REG1 3 12    .
```

Note that the two region assignments (for ring 3, cells 2 and 12) must agree in the nodal deck since rotational symmetry is specified on card type 04. If this change in region assignments were not made, REG2 would be assigned a zero region volume since it lies outside the hexagonal-geometry region of solution shown in Appendix F. This would in turn give a fatal error in the REBUS-3 code. In summary, while the GNIP4C conversion procedure is very convenient for converting large, previously-created finite difference decks to the nodal option, the user must exercise some caution whenever it is invoked. For this reason, warning messages are printed indicating new region assignments generated by this procedure, as well as the names of any regions with zero volumes. Printer-plotter and graphics maps for the nodal option are edited using the triangular-geometry orientation; they may, therefore, be of marginal use in checking input.

6.2.5 Background Region Name - A.NIP3 Card Type 31

The user is encouraged not to specify a background region since this results in an unnecessary increase in the region of solution. If no type 31 card is present, external boundary conditions will be imposed along the outer reactor boundary as mentioned under card type 04.

6.3 Restart Procedure

Analogous to the procedure in the standard finite difference option, nodal calculations can be restarted by saving the NHFLUX interface file (logical unit number 23) and placing it in BLOCK=OLD for a subsequent run.

6.4 Limitations of the Nodal Option

The nodal option has the following limitations:

(1) Reflective boundary conditions are not permitted in the plane.

(2) Fixed source problems are not permitted.

(3) Adjoint calculations are not permitted.

(4) Internal black boundary conditions are not permitted.

(5) Up-scattering is not permitted.

7. PROGRAMMING INFORMATION

The information provided in this section is intended to assist users who wish to make changes in the nodal option or who wish to understand the flow of the calculation. Users faced with the task of making the DIF3D code operational at their installations should refer to Section 5 of Ref. 3.

7.1 Programming Structure

Figure 7.1 shows the structure of the DIF3D code block.* The subroutines preceded by an asterisk and the common blocks beginning with "NH" ("nodal hex") are used only when the nodal option is invoked. All common blocks appearing in the DIF3D code block are documented in the dummy subroutine BLOCKS included in the DIF3D source code.

Since the functions of the subroutines shown in Fig. 7.1 are described in the comment cards which appear at the beginning of each subroutine in the code, only a brief overview is provided here. The subroutine NHINIT called from SSINIT controls the preliminary processing required before the data management strategy can be determined in subroutines NHCORE and NHDISK. The preliminary calculations include redefining the spatial mesh in the ordering used in the nodal option, setting up pointers to partial currents, and determining the number of unique nodes for which coupling coefficients must be computed and stored. These tasks are discussed below in Sections 7.4.1, 7.4.2, and 7.4.3, respectively.

The nodal flux calculation (including the calculation of the coupling coefficients) is controlled by the primary overlay NHSST. Four secondary overlays are invoked from NHSST. The secondary overlay DNHCCC controls the calculation of the nodal coupling coefficients in two and three dimensions via calls to NHCC2D and NHCC3D. The transverse leakage coupling coefficients are calculated in NHTVLC, and the number of inner iterations (4-color checkerboard sweeps) is determined via calls to NHINNR.

The secondary overlay DNHSTT initializes the flux and partial current vectors by either reading a previously written NHFLUX interface file, or by assuming a spatially flat flux shape in each energy group. These initializations are performed by FXREAD and FXINIT, respectively. The initial fission source vector is then calculated via calls to FSINIT.

The secondary overlay DNHOUT controls the outer iterations in the nodal option. The roles of the five principal subroutines (OUTR1,...,OUTR5) called by this subroutine are shown in the flow chart in Fig. 4.1.

The final secondary overlay invoked by NHSST is DNHFIN, which performs some final tasks required before the DIF3D edit overlay (DSSTOU) is invoked. These operations include reordering the nodal fluxes in the GEODST ordering

*As discussed in Ref. 3, the DIF3D system consists of a collection of large independent code blocks logically connected by a small "driver" subroutine. The code block DIF3D performs the neutron flux and criticality calculations.

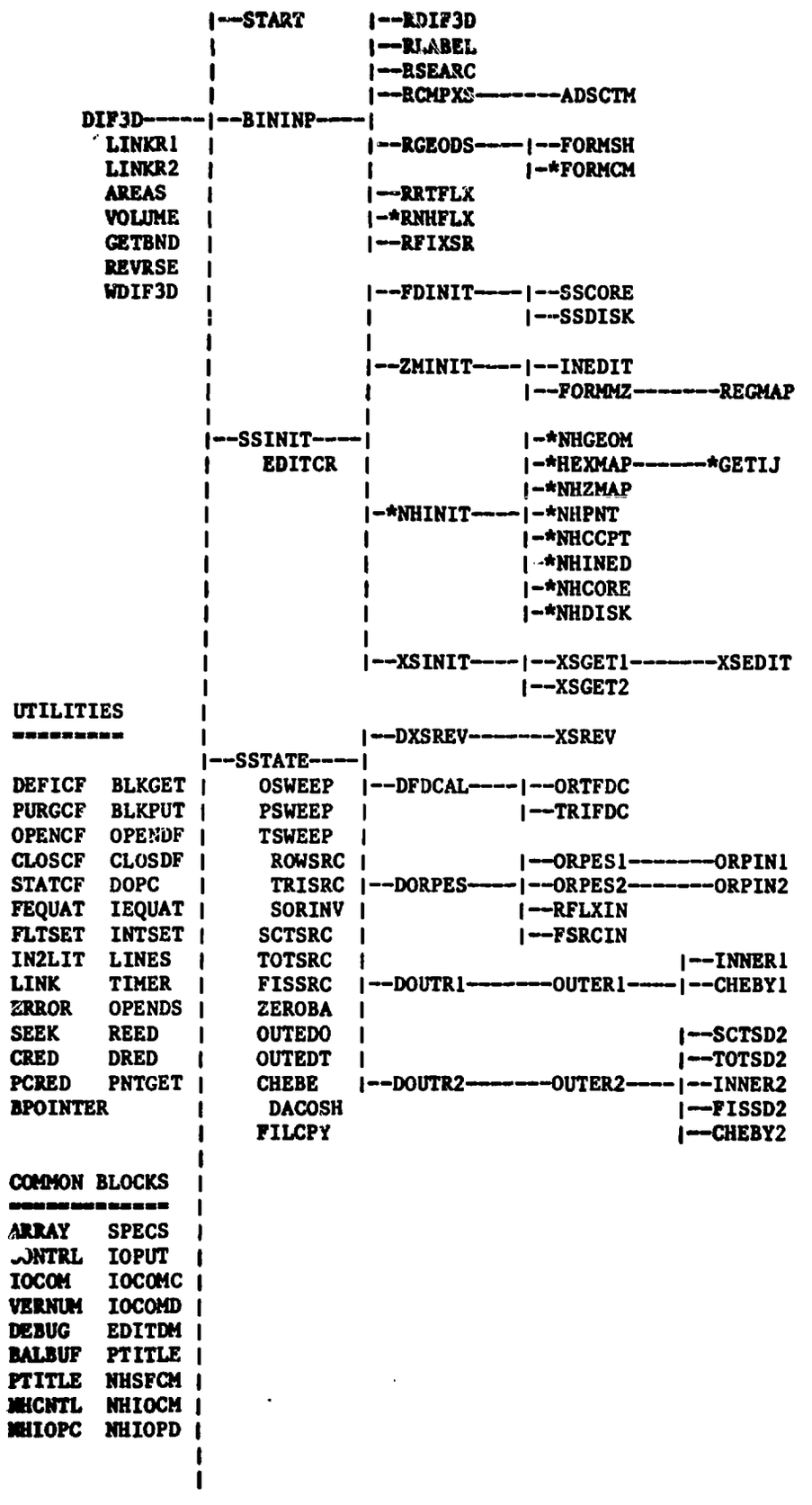

Fig. 7.1 Subroutine Map for the DIF3D Code Block

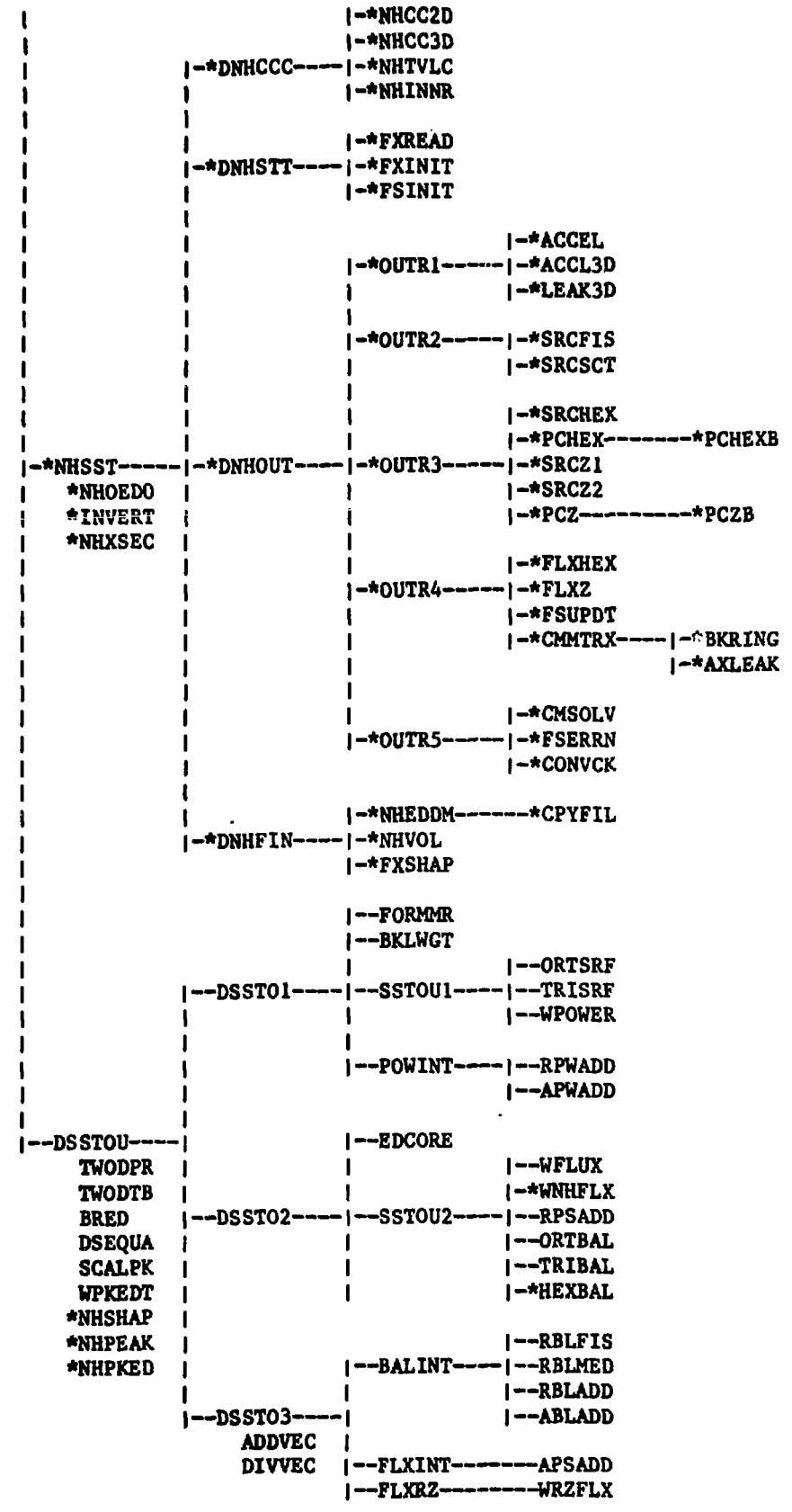

Fig 7.1 Subroutine Map for the DIF3D Code Block (Cont'd)

(see Section 7.4.1) and computing the coefficients required for the calculation of peak power densities and peak fluxes in the edit overlay.

Solution edits in the nodal option are performed using many of the same subroutines used in the finite difference option. Several subroutines have been added to the edit overlay (DSSTOU) to accommodate the nodal option. HEXBAL computes the leakage integrals in hexagonal geometry, and WNHFLX writes the interface file NHFLUX used to restart nodal calculations. The subroutines NHSHAP, NHPEAK, and NHPKED are used in computing the peak power densities and peak total fluxes in the nodal option.

7.2 Data Management Strategy

The data management strategy in the DIF3D nodal option is similar to that in the finite difference option. In the following discussion, the generic terms FCM (fast core memory) and ECM (extended core memory) refer to the two different container arrays employed by the BPOINTER package[29] in DIF3D. Both containers are in fast-core memory on one-level computers such as the IBM 370 series. On two-level computers, of which the CDC 7600 is the only example at present, the FCM container is in SCM (small-core memory) and the ECM container is in LCM (large-core memory). As in the finite difference options,[3] core files are allocated in the ECM container, and are therefore referred to as ECM files. The discussion in this section pertains to the allocation of ECM files and the transfer of data between ECM and disk files. The additional transfer of data between ECM and FCM required on the CDC 7600 computer is discussed in Section 7.3.

As mentioned in Section 6.1.1, the data management strategy is determined by the amount of ECM storage allocated on A.DIF3D card type 02. The minimum ECM storage requirement is given by the storage necessary to core-contain all group-independent files plus the storage for one-group ECM buffers for the group-dependent files stored on disk. Available storage beyond this minimum requirement is used first to ECM-contain the scattering band of fluxes, and then to contain as many of the group-dependent files as possible. This strategy is implemented in the subroutine NHCORE. Since all data (i.e. all mesh planes) for at least one group must be in ECM, there is no motivation to implement an algorithm analogous to the concurrent inner iteration strategy (CIIS) employed in the finite difference option.

The calculation of the peak power densities and peak fluxes in the nodal option requires several large files (FLXSHP, PWDSHP, and PEAKNH) that are not required during the outer iteration procedure. As a result, the storage required for the edit overlay may exceed that required for the outer iterations. For this reason, separate data management strategies are used for the eigenvalue calculation and the edit overlay. This situation is illustrated by the sample data management page shown in Fig. 6.1. The minimum storage requirement (all data for 1 group in ECM during the outer iterations) is calculated as described in the previous paragraph, subject to the additional constraint that the minimum amount of storage required by the edit overlay also be available. Once this minimum requirement is satisfied, an attempt is made to core-contain the scattering band of fluxes followed by the group-dependent files (flux-moments, new hex-plane partial currents, etc) in the order shown in Fig. 6.1. In determining the location of files during the edit overlay,

all required group-dependent files (with the exception of the cross section file, which retains its location during the outer iterations) are assumed to be on disk initially with 1-group ECM buffers. These files are then transferred to core in the order shown in Fig. 6.1 as storage permits. Note that it is possible for the partial current and flux moment files to be in core during the outer iterations and on disk during the edit overlay. In this case the subroutine CPYFIL (called from NHEDDM) is used to copy the file to the proper location for the edit overlay.

The scratch disk files used in the nodal option are listed in Table 7.1. Note that most of these files (e.g. FLXSHP, CCOEF, etc.) replace finite difference files which are not used in the nodal calculation. Data are transferred between these disk files and the corresponding ECM files shown in Table 7.2 via calls to the DIF3D data management routines[3] BLKGET and BLKPUT, which in turn call the standardized subroutines[29,30] DRED and DRIT specified by the Committee on Computer Code Coordination. Files for which no disk name is given in Table 7.2 are group-independent and are always contained in ECM. The remaining group-dependent ECM files are opened (via calls to OPENCF) with enough words to hold data for all groups if the file is core-contained. If the file is stored on disk, the corresponding ECM file is opened for only one group, and this space is used to buffer data as it is written one group at a time to and from the disk file. If the scattering band of fluxes is core-contained, the ECM file FLUX is opened with enough words to hold data for MAXSCT+1 groups, where MAXSCT is the maximum number of down-scatter groups.

Table 7.1 Scratch Disk Files Used in the Nodal Option

File Group Number	File Reference Number	SEEK Table File Name	Finite Difference File Name	Nodal File Name
2	1	RNDM01	PSIOLD	PSIOLD
3	2	RNDM02	PSINEW	PSINEW
5	3	RNDM03	PSIUP	FLXSHP
1	4	RNDM04	FDCOEF	CCOEF
2	5	RNDM05	FRNOLD	PCHOLD
3	6	RNDM06	FRNNEW	PCHNEW
4	7	RNDM07	FRNM1	PCZOLD
5	8	RNDM08	FRNM2	PCZNEW
4	9	RNDM09	SRCNEW	--
1	10	RNDM10	ZONMAP	--
6	11	RNDM11	CXSECT	CXSECT
4	12	RNDM12	FSRC	--
2	13	RNDM13	PSIGO	FLXOLD
3	14	RNDM14	PSIGN	FLXNEW

Table 7.2 Correspondence Between ECM and Disk Files in the Nodal Option

ECM File Name	Disk File Name	File Contents
NHMAP	--	Composition Map in Nodal Ordering
IPCPNT	--	Pointers to Hex-Plane Partial Currents
IHXPNT	--	Pointers to Mesh-Cells in Nodal Ordering
ICCPNT	--	Pointers to Nodal Coupling Coefficients
CMR	--	Storage for Coarse-Mesh Rebalance Matrix
XYLEAK	--	Axial Moments of Hex-Plane Leakage
FSRC	--	Fission Source Moments
FSRC1	--	FSRC From Previous Outer Iteration
FLUX	FLXNEW, FLXOLD	Nodal Flux Moments
PCURRH	PCHNEW	Hex-Plane Partial Currents
PCURRZ	PCZNEW	Axial Partial Currents
PCURH1	PCHOLD	PCURRH From Previous Outer Iteration
PCURZ1	PCZOLD	PCURRZ From Previous Outer Iteration
CXSECT	CXSECT	Cross Sections
CCOEF	CCOEF	Nodal Coupling Coefficients
VOLUME	--	Mesh-Cell Volumes in GEODST Ordering
ZONMAP	--	Composition Map in GEODST Ordering
PSINEW	PSINEW, PSIOLD	Nodal Fluxes in GEODST Ordering
FLXSHP	FLXSHP	Flux Shape Coefficients Used to Compute Peak Values in Edit Overlay
PWDSHP	--	Power-Density Shape Coefficients
PEAKNH	--	Nodal Peak Values by Mesh Cell

The ECM files listed in the upper section of Table 7.2 are defined (via calls to DEFICF) in subroutines NHINIT and NHCORE, while those files shown in the lower half are defined in subroutine NHEDDM and are used only in the DIF3D edit overlay. (The files VOLUME, PSINEW, and FLXSHP are calculated in the secondary overlay DNHFIN shown in Fig. 7.1). All disk files used in the nodal option are defined in subroutine NHDISK using calls to DEFIDF. The characteristics of the files shown in Table 7.2 are given by the calling arguments in DEFICF and DEFIDF, and thus will not be given here. Smaller arrays not shown in Table 7.2 are stored in the FCM container array via calls to the BPOINTER routine PUTM, and are described in the comment cards included in the subroutines in which they are used.

7.3 Additional Data Management Considerations for the CDC 7600 Computer

The CCCC subroutines[29,30] CRED and CRIT are used to transfer data between ECM and FCM on two-level computers such as the CDC 7600.* The use of these routines thus avoids direct addressing of extended core memory. The two-level implementation of the nodal option requires that one-group data for a single mesh plane plus all cross sections and coupling coefficients for a single group fit in the available fast core memory. The finite difference option also requires that all cross sections for a single group fit in FCM, but permits blocking on the mesh plane such that only pointwise data for one or more mesh lines need be stored in FCM. Full-core models of large fast reactor designs with at least 200 zones (material compositions) can be accommodated by the nodal option on the CDC 7600 computer.

The nodal two-level data management strategy is implemented in the following manner. The FCM array SCRFCM is used to store all data which is transferred between ECM and FCM. The pointers to the scratch sub-arrays held in SCRFCM are not fixed throughout the calculation, but are instead recalculated at various stages of the calculation in accordance with the FCM storage required at these points. The length of this array is thus determined as the maximum scratch FCM storage required at any point in the nodal calculation. This dynamic allocation procedure minimizes the size of the SCRFCM array since only data actually used at each stage of the calculation is stored in SCRFCM.

In order to further clarify this procedure, we consider for example the FCM storage required in subroutine OUTR4, which calls FLXHEX, FLXZ, FSUPDT, and CMMTRX (see Fig. 7.1). These latter subroutines, like all of the lowest-level nodal subroutines, process data for a single mesh plane at a time. Therefore, SCRFCM must contain all single-plane data used by the subroutines called by OUTR4. This situation is illustrated in Table 7.3. A total of 10 scratch arrays (e.g. IANPNT, IZNMAP, etc.) are used by FLXHEX, FLXZ, FSUPDT, and CMMTRX as these subroutines are called in order from within a loop over mesh planes. Data for the arrays IANPNT, IZNMAP, FLUX, and CXSECT are read for each plane from ECM into consecutive storage locations in SCRFCM as shown in Table 7.3. These arrays retain their locations in SCRFCM during the four calls required for each mesh plane. The arrays PCH and IPCPNT are read into SCRFCM and used during the execution of FLXHEX, but this same space is then used by the arrays XYLEAK, PCZ, and FSRC during execution of FLXZ and FSUPDT. CMMTRX then requires PCH, IPCPNT, and PCZ again, so these arrays are once again read into SCRFCM. The asterisk in front of these arrays denotes the fact that these arrays must be read prior to the call to CMMTRX. Arrays which are recalculated (e.g. the FLUX array in this example) are then written from SCRFCM back to ECM.

Tables such as that shown in Table 7.3 appear in the comment cards of the source code wherever this dynamic allocation of SCRFCM is used. The reader is reminded that this procedure is employed only in the two-level implementation

*Recall that the generic terms FCM and ECM refer to SCM (small core memory) and LCM (large core memory) on the CDC 7600 computer.

of the DIF3D nodal option. However, the SCRFCM array is used in the one-level implementation to store two scratch arrays (QSRC and BMATRX) used in OUTR3 and OUTR5.

Table 7.3 Allocation of Scratch Arrays in the FCM Array SCRFCM During Subroutine OUTR4 (Two-Level Implementation Only)

Subroutine →	FLXHEX	FLXZ	FSUPDT	CMMTRX
	(1) IANPNT	IANPNT	IANPNT	IANPNT
	(2) IZNMAP	IANMAP	IANMAP	IANMAP
	(3) FLUX	FLUX	FLUX	FLUX
	(4) CXSECT	CXSECT	CXSECT	CXSECT
	(5) PCH		(9) FSRC	(*) PCH
	(6) IPCPNT	(7) XYLEAK		(*) IPCPNT
		(8) PCZ		(*) PCZ
				(10) CMR

Before discussing the subroutines used to transfer data between ECM and FCM, it is necessary to discuss briefly the structure of the ECM files shown in Table 7.2. The ECM files are blocked into records such that each record consists of one-group data for a single mesh plane. Two exceptions to this rule are the cross section and coupling coefficient files in which a record contains all data for a single energy group. These latter files thus contain NGROUP records, while, for example, the group-dependent ECM flux file contains a total of NGROUP*KM records, where KM is the number of axial planes. The nodal two-level data management strategy thus involves the transfer of complete records of data between the ECM files and the SCRFCM array.

Data is transferred between ECM files and SCRFCM via calls to the utility routines PCRED, PCRIT, ICRED, and ICRIT. These routines, which are not used at present in the finite difference option, transfer a single record between an ECM file and SCRFCM on two-level computers using calls to the CCCC routines CRED and CRIT. They are also called in the one-level implementation, where they simply return the array pointer relative to the ECM container, which is stored in fast core memory on one-level computers. These functions are explained further in the comment cards appearing in the listing of subroutine PCRED.

The single exception to the above procedure occurs in the treatment of the group-independent file PWDSHP in the DIF3D edit overlay. This array involves a total of 32 words per node in three-dimensional calculations. Due to the large amount of data stored for each plane, data in this array are transferred between ECM and FCM in blocks which may correspond to some fraction of the nodes on the plane. The length of the sub-block is determined in NHCORE.

7.4 Additional Programming Details

7.4.1 Mesh-Cell Ordering

The two different mesh cell orderings used in the nodal option are illustrated in Fig. 7.2 for a two-dimensional sixth-core model with 6 rings of hexagons. The GEODST ordering refers to the ordering of hexagons employed in the CCCC geometry interface file GEODST (Ref. 30). This file is written by the input processor GNIP4C and subsequently processed by subroutine RGEODS in the DIF3D code block. In the GEODST ordering, the hexagons are numbered by rows, with "background" hexagons added to fill out the mesh such that all rows have the same number of hexagons. The second ordering shown in Fig. 7.2 is used during the nodal calculation controlled by the primary overlay NHSST. The hexagons are ordered starting with the central hexagon and then moving outward in a counterclockwise spiral. This ordering includes hexagons along only one of the two symmetry lines [the excluded hexagons are treated via periodic (rotational symmetry) boundary conditions], and does not require any background hexagons if all rings are full (as is the case in Fig. 7.2). The nodal ordering thus reduces storage requirements, and is better suited to the type of calculations (partial current sweeps, coarse-mesh rebalance on rings of hexagons) performed in the nodal option. The GEODST ordering is used in all interface files (e.g. RTFLUX, PWDINT, PKEDIT, etc.) written by the nodal option, with the exception of the nodal restart file NHFLUX, which is written in nodal ordering.

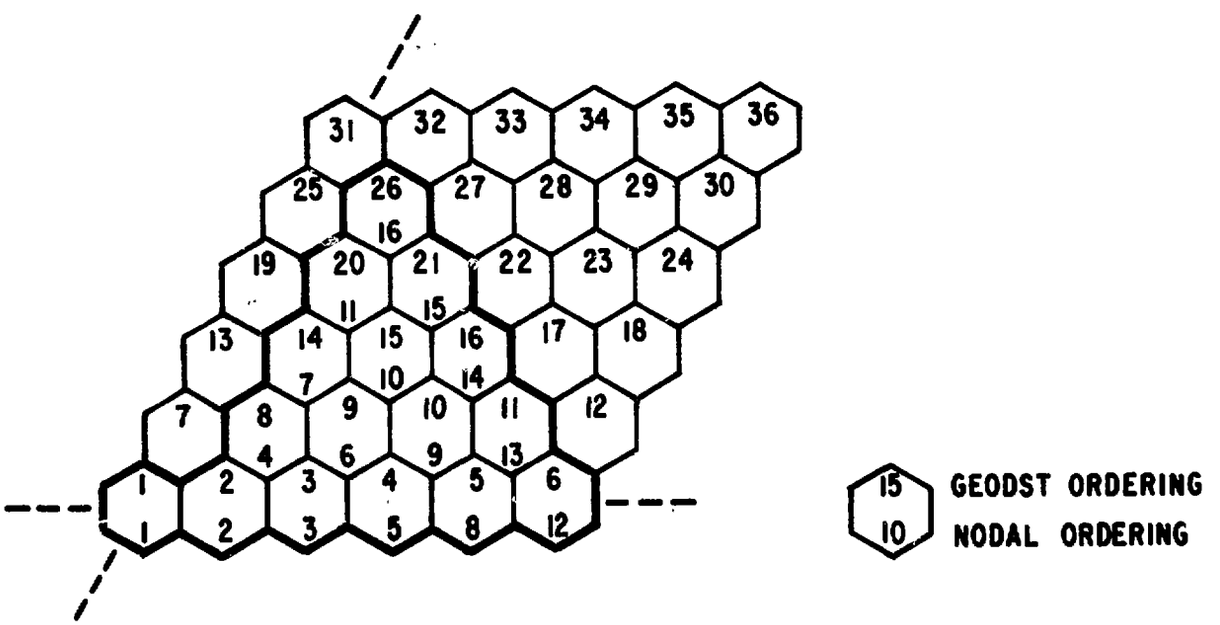

Fig. 7.2 GEODST and Nodal Mesh-Cell Orderings (Sixth-Core Symmetry)

The ECM file IHXPNT includes three separate records containing information related to the ordering of the mesh cells. The first record, an array IANPNT, contains pointers to "active" nodes, i.e. nodes which are included in the actual reactor model as opposed to the background nodes used to fill in the broken outer rings typical of LMFBR designs. Use of the pointers in IANPNT permits sweeps over active nodes only, without use of IF testing in the loop over mesh cells. The second record in IHXPNT is ICBPNT, which contains pointers to the active nodes in the four-color checkerboard ordering used in computing the hex-plane partial currents. The final record in IHXPNT is ITRMAP, a transformation map between the nodal and GEODST orderings. ITRMAP is used to reorder fluxes computed in the nodal overlay into the GEODST ordering used in the DIF3D edit overlay. IANPNT and ICBPNT are calculated in subroutine NHPNT, and ITRMAP is computed in HEXMAP. Since all mesh planes in the three-dimensional mesh must have the same outer hex-plane boundary, it is necessary to store these pointers only for a single plane.

7.4.2 Partial Current Ordering

The hex-plane and z-directed partial currents are stored in the ECM files PCURRH and PCURRZ, respectively. PCURRH contains NGROUP*KM records, where KM is the number of axial mesh planes. Each record contains a total of NPCHEX (=6*NHEX + NPCBDY) partial currents, where NHEX is the number of hexagons on a plane (including background nodes) and NPCBDY is the number of incoming partial currents on the outer hex-plane boundary. The six outgoing partial currents are stored consecutively for each node as shown in Eq. (2.82) and the nodes are ordered in the nodal ordering illustrated in Fig. 7.2. The 6*NHEX outgoing partial currents for the plane are followed by the NPCBDY incoming partial currents on the boundary. The file PCURRZ contains NGROUP*(KM+1) records, where KM+1 is the number of axial mesh boundaries. Each record consists of 2*NHEX partial currents: the NHEX partial currents in the negative z-direction plus the NHEX partial currents in the positive z-direction.

The efficient execution of the algorithms presented in Section 4 requires the use of pre-computed pointers to the six incoming hex-plane partial currents for each node. These incoming partial currents are either outgoing partial currents from neighboring nodes, incoming partial currents on the outer hex-plane boundary, or, in the case of fractional-core models (e.g. Fig. 7.2) with periodic boundary conditions, outgoing partial currents across surfaces along a periodic boundary. The pointers are stored in the ECM file ICCPNT, which consists of a single record of length 6*NHEX. For example, if IPIN=IPCPNT(J,K), then PCURRH(IPIN) is the incoming partial current on hex-plane surface J (J=1,...,6) for node K and the current energy group. A different set of pointers (stored in the FCM array IPCBDY) are used to compute incoming partial currents on the outer hex-plane boundary.

7.4.3 Storage of the Nodal Coupling Coefficients

As discussed in Section 3.5, nodal coupling coefficients are stored only for unique nodes characterized by material composition (CCCC zone) assignment and axial mesh spacing. The number of unique nodes is determined

in NHCORE via calls to NHCCPT. Pointers to unique nodes are stored in the ECM file ICCPNT. For example, if NTYP = ICCPNT(K), then (CCOEF(I,NTYP), I=1,...,13) contains the 13 coupling coefficients for the K-th node and the current energy group in three-dimensional calculations. The 13 unique coefficients are stored in the order shown in Eq. (B.32). In two-dimensional calculations, only 7 unique coefficients are required, and they are stored in the order shown in Eq. (A.51).

ACKNOWLEDGEMENTS

The author is indebted to Keith Derstine for his valuable assistance in the implementation of the nodal scheme in the DIF3D code, and for his critical review of the manuscript. Numerous discussions with Cy Adams, Greg Greenman, and Herb Henryson II are gratefully acknowledged. Bert Toppel provided the REBUS-3 calculations for the LCCEWG benchmark problem analyzed in Section 5. The superb efforts of Marge Ramirez in typing this report are greatly appreciated.

REFERENCES

1. R. W. Hardie, and W. W. Little, Jr., "3DB, A Three-Dimensional Diffusion Theory Burnup Code," BNWL-1204, Battelle-Pacific Northwest Laboratories, 1970.

2. D. R. Vondy, T. B. Fowler, and G. W. Cunningham, "VENTURE: A Code Block for Solving Multigroup Neutronics Problems Applying the Finite-Difference Diffusion-Theory Approximation to Neutron Transport," ORNL-5062, Oak Ridge National Laboratory, 1975.

3. K. L. Derstine, "DIF3D: A Code to Solve One-, Two-, and Three-Dimensional Finite-Difference Diffusion Theory Problems," ANL-82-64, Argonne National Laboratory, 1983.

4. C. H. Adams, "SYN3D: A Single Channel Spatial Flux Synthesis Code for Diffusion Theory Calculations," ANL-76-21, Argonne National Laboratory, 1976.

5. B. J. Toppel, "A User's Guide for the REBUS-3 Fuel Cycle Analysis Capability," ANL-83-2, Argonne National Laboratory, 1983.

6. A. F. Henry, "Refinements in Accuracy of Coarse-Mesh Finite-Difference Solution of the Group Diffusion Equations," in Numerical Reactor Calculations, p. 447, International Atomic Energy Agency, Vienna, 1972.

7. See for example: J. Dorning, "Modern Coarse-Mesh Methods - A Development of the '70's," Proceedings of the Topical Meeting on Computational Methods in Nuclear Engineering, Williamsburg, VA., Vol. 1, p. 3-2, American Nuclear Society, April, 1979.

8. J. J. Arkuszewski, and M. Makai, "Analytical Coarse Mesh Approximations for Solving Diffusion Equations in Hexagonal and Square Geometries," Proceedings of the International Topical Meeting on Advances in Mathematical Methods for the Solution of Nuclear Engineering Problems, Munich, Vol. 2, p. 89, American Nuclear Society/European Nuclear Society, April, 1981.

9. T. Duracz, "A Nodal Method in Hexagonal Geometry," Proceedings of the International Topical Meeting on Advances in Mathematical Methods for the Solution of Nuclear Engineering Problems, Munich, Vol. 1, p. 423, American Nuclear Society/European Nuclear Society, April, 1981.

10. R. D. Lawrence, "A Nodal Interface Current Method for Multigroup Diffusion Calculations in Hexagonal Geometry," Trans. Am. Nucl. Soc., 39, 461 (1981).

11. R. D. Lawrence, "A Nodal Method for Three-Dimensional Fast Reactor Calculations in Hexagonal Geometry," Proceedings of the Topical Meeting on Advances in Reactor Computations, Vol. II, p. 1030, Salt Lake City, American Nuclear Society, March, 1983.

12. Allan F. Henry, Nuclear-Reactor Analysis, MIT Press, Cambridge, Mass. (1975).

13. R. D. Lawrence, "A Nodal Method for the Solution of the Neutron Diffusion Equation in Hexagonal Geometry," Intra-Laboratory Memorandum, Argonne National Laboratory, February, 1981.

14. D. R. Ferguson and K. L. Derstine, "Optimized Iteration Strategies and Data Management Considerations for Fast Reactor Finite Difference Diffusion Theory Codes," Nucl. Sci. Engr., 64, 593 (1977).

15. H. Finnemann, F. Bennewitz, and M. R. Wagner, "Interface Current Techniques for Multidimensional Reactor Calculations," Atomkernenergie, 30, 123 (1977).

16. R. N. Sims and A. F. Henry, "A Coarse-Mesh Nodal Diffusion Method Based on Response Matrix Considerations," MITNE-197, Massachusetts Institute of Technology, 1977.

17. C. Maeder, "A Nodal Diffusion Method with Legendre Polynomials," Proceedings, Advances in Reactor Physics, Gatlinburg, Tennessee, p. 131, American Nuclear Society, April 1978.

18. G. Greenman, K. Smith, and A. F. Henry, "Recent Advances in an Analytic Nodal Method for Static and Transient Reactor Analysis," Proceedings of the Topical Meeting on Computational Methods in Nuclear Engineering, Williamsburg, VA., p. 3-49, American Nuclear Society, April, 1979.

19. R. A. Shober, "A Nodal Method for Fast Reactor Analysis," Proceedings of the Topical Meeting on Computational Methods in Nuclear Engineering, Williamsburg, VA., p. 3-33, American Nuclear Society, April, 1979.

20. R. D. Lawrence and J. J. Dorning, "A Nodal Green's Function Method for Multidimensional Neutron Diffusion Calculations," Nucl. Sci. Engr., 76, 218 (1980).

21. E. L. Wachpress, Iterative Solution of Elliptic Systems, Prentice-Hall, Inc., Englewood Cliffs, N.J. (1966).

22. R. Froehlich, "A Theoretical Foundation for Coarse-Mesh Variational Techniques," GA-7870, Gulf General Atomic, 1968.

23. M. R. Wagner, "GAUGE - A Two-Dimensional Few Group Neutron Diffusion - Depletion Program for a Uniform Triangular Mesh," GA-8307, Gulf General Atomic, 1968.

24. G. Buckel, K. Kufner, and B. Stehle, "Benchmark Calculations for a Sodium-Cooled Breeder Reactor by Two- and Three-Dimensional Diffusion Methods," Nucl. Sci. Engr. 64, 75 (1977).

25. "Benchmark Problem Book," ANL-7416, Supplement 3, Argonne National Laboratory, to appear, 1983.

26. J. W. Lewellen, private communication, 1982.

27. B. J. Toppel, C. H. Adams, R. D. Lawrence, H. Henryson II, and K. L. Derstine, "Validation of Alternative Methods and Data for a Benchmark Fast Reactor Depletion Calculation," Proceedings of the Topical Meeting on Advances in Reactor Physics and Core Thermal Hydraulics, (held in Kiamesha Lake, NY), NUREG/CP-0034, Vol. 1, p. 177, U.S. Nuclear Regulatory Commission, Washington, D.C., August 1982.

28. B. J. Toppel, private communication, 1982.

29. C. H. Adams, K. L. Derstine, H. Henryson II, R. P. Hosteny and B. J. Toppel, The Utility Subroutine Package Used by Applied Physics Export Codes, ANL-83-3, Argonne National Laboratory, 1983.

30. R. Douglas O'Dell, "Standard Interface Files and Procedures for Reactor Physics Codes, Version IV," LA-6941-MS, Los Alamos National Laboratory, 1977.

APPENDIX A
DERIVATION OF THE TWO-DIMENSIONAL RESPONSE MATRIX EQUATION

The purpose of this Appendix is to provide additional details of the steps leading from the expression [Eq. (2.80)] for the interface partial current to the final form [Eq. (2.85)] of the two-dimensional response matrix equation. Before doing so, however, it is necessary to give some additional details concerning the calculation of the expansion coefficients a^k_{gx3} and the term $E^k_{gx}(h/2)$ which appear in Eq. (2.80).

A.1 Calculation of the Expansion Coefficient a^k_{gx3}

The following expression [Eq. (2.41)] for a^k_{gx3} was derived in Section 2.4.1:

$$a^k_{gx3} \equiv E^k_{gx}(0), \tag{A.1}$$

where

$$E^k_{gx}(x) \equiv \phi^k_g(x,y_s(x)) + \phi^k_g(x,-y_s(x)) - 2\bar{\phi}^k_{gx}(x). \tag{A.2}$$

The final form of the equation for a^k_{gx3} was then derived by (1) developing a relationship [Eq. (2.43)] between $E^k_{gx}(x)$ and the leakage term $\ell^k_{gy}(x)$ defined in Eq. (2.42), (2) approximating $\ell^k_{gy}(x)$ as shown in Eq. (2.44), and (3) combining these results to obtain a final equation [Eq. (2.53)] for a^k_{gx3}. These steps are discussed in order in the following subsections.

A.1.1 The Relationship Between $E^k_{gx}(x)$ and $\ell^k_{gy}(x)$

As discussed in Section (2.4.1), the form of Eq. (A.2) suggests that $E^k_{gx}(x)$ can be related to the y-directed leakage defined by

$$\ell^k_{gy}(x) \equiv \frac{1}{2y_s(x)} \int_{-y_s(x)}^{y_s(x)} dy \; -D^k_g \frac{\partial^2}{\partial y^2} \phi^k_g(x,y)$$

$$= \frac{1}{2y_s(x)} \left[-D^k_g \frac{\partial}{\partial y} \phi^k_g(x,y) \right]_{y=-y_s(x)}^{y=y_s(x)}. \tag{A.3}$$

This relationship is derived by expanding $\phi_g^k(x,y)$ in a Taylor series around the point (x,0):

$$\phi_g^k(x,y) = \phi_g^k(x,0) + y \frac{\partial}{\partial y} \phi_g^k(x,y)\Big|_{y=0}$$

$$+ \frac{1}{2} y^2 \frac{\partial^2}{\partial y^2} \phi_g^k(x,y)\Big|_{y=0} + \frac{1}{6} y^3 \frac{\partial^3}{\partial y^3} \phi_g^k(x,y)\Big|_{y=0} + O(y^4). \qquad (A.4)$$

Evaluating Eq. (A.4) at $y=\pm y_s(x)$ and then summing the results yields

$$\phi_g^k(x,y_s(x)) + \phi_g^k(x,-y_s(x)) - 2\phi_g^k(x,0)$$

$$= [y_s(x)]^2 \frac{\partial^2}{\partial y^2} \phi_g^k(x,y)\Big|_{y=0} + O(h^4). \qquad (A.5)$$

Using Eq. (A.4),

$$\bar{\phi}_{gx}^k(x) \equiv \frac{1}{2y_s(x)} \int_{-y_s(x)}^{y_s(x)} dy\ \phi_g^k(x,y)$$

$$= \phi_g^k(x,0) + \frac{1}{6} [y_s(x)]^2 \frac{\partial^2}{\partial y^2} \phi_g^k(x,y)\Big|_{y=0} + O(h^4). \qquad (A.6)$$

Using Eq. (A.6) to eliminate $\phi_g^k(x,0)$ in Eq. (A.5) yields

$$E_{gx}^k(x) = \frac{2}{3} [y_s(x)]^2 \frac{\partial^2}{\partial y^2} \phi_g^k(x,y)\Big|_{y=0} + O(h^4). \qquad (A.7)$$

Since

$$\frac{\partial^2}{\partial y^2} \phi_g^k(x,y)\Big|_{y=0} = -\frac{1}{D_g^k} f_{gy}^k(x) + O(h^2),$$

Eq. (A.7) becomes

$$E^k_{gx}(x) = -\frac{1}{6D^k_g}\,[2y_s(x)]^2\,\mathfrak{L}^k_{gy}(x) + O(h^4). \tag{A.8}$$

This result was given as Eq. (2.43) in Section 2.4.3.

A.1.2 Approximation of $\mathfrak{L}^k_{gy}(x)$

The y-directed leakage is approximated by Eq. (2.44):

$$\mathfrak{L}^k_{gy}(x) \equiv \begin{cases} \mathfrak{L}^k_{gy-} & -h/2 < x < 0 \\ \mathfrak{L}^k_{gy+} & 0 < x < h/2 \end{cases}, \tag{A.9}$$

where $\mathfrak{L}^k_{gy-}$ and $\mathfrak{L}^k_{gy+}$ are half-node averages defined in Eqs. (2.45). The initial steps in the derivation leading to expressions for these averages are given by Eqs. (2.46) through (2.51). We continue this derivation here by substituting Eq. (2.49) into Eq. (2.50b) to yield

$$\begin{aligned} \bar{J}^k_{gu}(+h/2) - \bar{J}^k_{gv}(-h/2) = -2\,\frac{D^k_g}{h}\Bigg\{ & \frac{1}{2}\,[\phi^k_g(x,y_s(x)) + \phi^k_g(x,-y_s(x))]_{x=h/2} \\ & - \frac{1}{2}\,[\phi^k_g(x,y_s(x)) + \phi^k_g(x,-y_s(x))]_{x=0} \\ & + \frac{2}{\sqrt{3}} \int_0^{h/2} dx \left[\frac{\partial}{\partial y}\,\phi^k_g(x,y)\right]^{y=y_s(x)}_{y=-y_s(x)} \Bigg\} \end{aligned} \tag{A.10}$$

From Eqs. (A.2) and (2.51b):

$$\phi^k_g(x,y_s(x)) + \phi^k_g(x,-y_s(x)) = E^k_{gx}(x) + 2\bar{\phi}^k_{gx}(x) \tag{A.11}$$

$$-D_g^k \int_0^{h/2} dx \left[\frac{\partial}{\partial y}\,\phi_g^k(x,y)\right]_{y=-y_s(x)}^{y=y_s(x)} = \frac{1}{2}\,v^k\,\mathfrak{f}_{gy+}^k = \frac{\sqrt{3}}{4}\,h^2\,\mathfrak{f}_{gy+}^k . \qquad (A.12)$$

Substituting Eqs. (A.11) and (A.12) into Eq. (A.10) yields

$$\bar{J}_{gu}^k(+h/2) - \bar{J}_{gv}^k(-h/2) = \frac{-D_g^k}{h}\left\{[E_{gx}^k(h/2) - E_{gx}^k(0)] + 2[\bar{\phi}_{gx}^k(+h/2) - \bar{\phi}_{gx}^k(0)]\right\} + h\,\mathfrak{f}_{gy+}^k . \qquad (A.13)$$

Neglecting the $O(h^4)$ error in Eq. (A.8):

$$E_{gx}^k(h/2) = -\frac{h^2}{18D_g^k}\,\mathfrak{f}_{gy+}^k \qquad (A.14)$$

$$E_{gx}^k(0) \equiv \frac{1}{2}\,[E_{gx}^k(0^-) + E_{gx}^k(0^+)] = -\frac{h^2}{9D_g^k}\,[\mathfrak{f}_{gy-}^k + \mathfrak{f}_{gy+}^k] . \qquad (A.15)$$

Substituting Eqs. (A.14) and (A.15) into Eq. (A.13) and simplifying yields

$$\bar{J}_{gu}^k(+h/2) - \bar{J}_{gv}^k(-h/2) = \frac{h}{18}\,[17\,\mathfrak{f}_{gy+}^k - 2\,\mathfrak{f}_{gy-}^k] - \frac{2D_g^k}{h}\,[\bar{\phi}_{gx}^k(+h/2) - \bar{\phi}_{gx}^k(0)] . \qquad (A.16a)$$

Substituting Eq. (2.49) into Eq. (2.50a), using Eq. (2.51a), and then following the above procedure leads to the analogous equation

$$\bar{J}^k_{gv}(+h/2) - \bar{J}^k_{gu}(-h/2) = \frac{h}{18}\,[17\,\bar{\varepsilon}^k_{gy-} - 2\,\bar{\varepsilon}^k_{gy+}]$$

$$- \frac{2D^k_g}{h}\,[\bar{\phi}^k_{gx}(-h/2) - \bar{\phi}^k_{gx}(0)]. \qquad \text{(A.16b)}$$

Solving for Eqs. (A.16) for $\bar{\varepsilon}^k_{gy-}$ and $\bar{\varepsilon}^k_{gy+}$ yields

$$\bar{\varepsilon}^k_{gy-} = \frac{6}{95}\,\{\frac{2}{h}\,[\bar{J}^k_{gu}(+h/2) - \bar{J}^k_{gv}(-h/2)] + \frac{4D^k_g}{h^2}\,[\bar{\phi}^k_{gx}(+h/2) - \bar{\phi}^k_{gx}(0)]$$

$$+ \frac{17}{h}\,[\bar{J}^k_{gv}(+h/2) - \bar{J}^k_{gu}(-h/2)] + \frac{34D^k_g}{h^2}\,[\bar{\phi}^k_{gx}(-h/2) - \bar{\phi}^k_{gx}(0)]\}. \qquad \text{(A.17a)}$$

$$\bar{\varepsilon}^k_{gy+} = \frac{6}{95}\,\{\frac{17}{h}\,[\bar{J}^k_{gu}(+h/2) - \bar{J}^k_{gv}(-h/2)] + \frac{34D^k_g}{h^2}\,[\bar{\phi}^k_{gx}(+h/2) - \bar{\phi}^k_{gx}(0)]$$

$$+ \frac{2}{h}\,[\bar{J}^k_{gv}(+h/2) - \bar{J}^k_{gu}(-h/2)] + \frac{4D^k_g}{h^2}\,[\bar{\phi}^k_{gx}(-h/2) - \bar{\phi}^k_{gx}(0)]\}. \qquad \text{(A.17b)}$$

A.1.3 Final Form of the Equation for a^k_{gx3}

Substituting Eqs. (A.17) into Eq. (2.52) yields

$$a^k_{gx3} = -\frac{2}{15}\,\frac{h}{D^k_g}\,[\bar{L}^k_{gu} + \bar{L}^k_{gv}] - \frac{4}{15}\,[\bar{\phi}^k_{gx}(+h/2) + \bar{\phi}^k_{gx}(-h/2) - 2\bar{\phi}^k_{gx}(0)], \qquad \text{(A.18)}$$

where

$$\bar{L}^k_{gu} \equiv \bar{J}^k_{gu}(+h/2) - \bar{J}^k_{gu}(-h/2)$$

$$\bar{L}^k_{gv} \equiv \bar{J}^k_{gv}(+h/2) - \bar{J}^k_{gv}(-h/2).$$

Using Eq. (2.33),

$$\bar{\phi}^k_{gx}(0) \cong \frac{36}{26}\bar{\phi}^k_g - \frac{5}{26}\left[\bar{\phi}^k_{gx}(+h/2) + \bar{\phi}^k_{gx}(-h/2)\right] + \frac{3}{52}a^k_{gx3}. \qquad (A.19)$$

Substituting Eq. (A.19) into Eq. (A.18), and then solving for a^k_{gx3} yields

$$a^k_{gx3} = -\frac{26}{189}\frac{h}{D^k_g}\left[\bar{L}^k_{gu} + \bar{L}^k_{gv}\right] - \frac{8}{21}\left[\bar{\phi}^k_{gx}(+h/2) + \bar{\phi}^k_{gx}(-h/2) - 2\bar{\phi}^k_g\right]. \qquad (A.20)$$

This final result for a^k_{gx3} was given as Eq. (2.53) in Section 2.4.3.

A.2 Calculation of $E^k_{gx}(h/2)$

An expression for $E^k_{gx}(h/2)$ is obtained by substituting Eq. (A.17b) into Eq. (A.14), using Eq. (A.19) to eliminate $\bar{\phi}^k_{gx}(0)$, and then simplifying the result:

$$E^k_{gx}(h/2) = -\frac{1}{285}\frac{h}{D^k_g}\left\{17\left[\bar{J}^k_{gu}(+h/2) - \bar{J}^k_{gv}(-h/2)\right] - 2\left[\bar{J}^k_{gv}(+h/2) - \bar{J}^k_{gu}(-h/2)\right]\right\}$$

$$- \frac{1}{1235}\left[179\,\bar{\phi}^k_{gx}(+h/2) + 49\,\bar{\phi}^k_{gx}(-h/2) - 228\,\bar{\phi}^k_g\right] + \frac{1}{130}a^k_{gx3}. \qquad (A.21)$$

A.3 The Response Matrix Equation

An expression for the outgoing surface-averaged partial current across the surface in the positive x-direction was given as Eq. (2.80):

$$J^{out,k}_{gx}(+h/2) = -\frac{D^k_g}{h}\left[a^k_{gx1} + \frac{36}{13}a^k_{gx2} + \frac{7}{26}a^k_{gx3} + \frac{1}{2}a^k_{gx4} + E^k_{gx}(h/2)\right]$$

$$+ \bar{J}^{in,k}_{gx}(+h/2). \qquad (A.22)$$

It is convenient to introduce constants β_1 and β_2 (which are either zero or one) in order to distinguish the approximations obtained for N=2,3, or 4 in Eq. (2.33), i.e.

$$\bar{J}^{out,k}_{gx}(+h/2) = -\frac{D^k_g}{h}\left\{a^k_{gx1} + \frac{36}{13}a^k_{gx2} + \left[\frac{7}{26}a^k_{gx3} + E^k_{gx}(h/2)\right]\beta_1 + \frac{1}{2}\beta_2\, a^k_{gx4}\right\} + \bar{J}^{in,k}_{gx}(+h/2), \tag{A.23}$$

where

$$\begin{aligned} N=2 &\Rightarrow \beta_1 \equiv 0, \quad \beta_2 \equiv 0 \\ N=3 &\Rightarrow \beta_1 \equiv 1, \quad \beta_2 \equiv 0 \\ N=4 &\Rightarrow \beta_1 \equiv 1, \quad \beta_2 \equiv 1. \end{aligned} \tag{A.24}$$

Note that consistent with Eq. (A.1), $E^k_{gx}(x)$ does not enter into the calculation for N=2 in Eq. (2.33).

The derivation of the final form of the response matrix equation follows the five steps described in Section 2.6. We repeat these steps in more detail here:

(1) Using Eqs. (2.34a) and (2.34b) yields

$$a^k_{gx1} + \frac{36}{13}a^k_{gx2} = \frac{49}{13}\bar{\phi}^k_{gx}(+h/2) + \frac{23}{13}\bar{\phi}^k_{gx}(-h/2) - \frac{72}{13}\bar{\phi}^k_g. \tag{A.25}$$

Combining Eqs. (A.20) and (A.21) yields

$$\begin{aligned} \frac{7}{26}a^k_{gx3} + E^k_{gx}(h/2) = &-\frac{1299}{5187}\bar{\phi}^k_{gx}(+h/2) - \frac{753}{5187}\bar{\phi}^k_{gx}(-h/2) \\ &+ \frac{2052}{5187}\bar{\phi}^k_g - \frac{4}{105}\frac{h}{D^k_g}\left[\bar{L}^k_{gu} + \bar{L}^k_{gv}\right] \\ &- \frac{17}{285}\frac{h}{D^k_g}\left[\bar{J}^k_{gu}(+h/2) - \bar{J}^k_{gv}(-h/2)\right] \\ &- \frac{2}{285}\frac{h}{D^k_g}\left[\bar{J}^k_{gv}(+h/2) - \bar{J}^k_{gu}(-h/2)\right]. \end{aligned} \tag{A.26}$$

Using Eq. (2.59b) yields

$$\frac{1}{2} a^k_{gx4} = -12\ \bar{\phi}^k_{gx1} + \frac{8}{3}\ [\bar{\phi}^k_{gx}(+h/2) - \bar{\phi}^k_{gx}(-h/2)]. \tag{A.27}$$

Substituting Eqs. (A.25), (A.26), and (A.27) into Eq. (A.23) and collecting terms yields

$$\begin{aligned}
\bar{J}^{out,k}_{gx}(+h/2) = -\frac{D^k_g}{h} \{ &[\frac{49}{13} - \frac{1299}{5187}\beta_1 + \frac{8}{3}\beta_2]\ \bar{\phi}^k_{gx}(+h/2) \\
&+ [\frac{23}{13} - \frac{753}{5187}\beta_1 + \frac{8}{3}\beta_2]\ \bar{\phi}^k_{gx}(-h/2) \\
&- [\frac{72}{13} - \frac{2052}{5187}\beta_1]\ \bar{\phi}^k_g - 12\,\beta_2\,\phi^k_{gx1}\} \\
&+ \frac{4}{105}\ [\bar{L}^k_{gu} + \bar{L}^k_{gv}] + \frac{17}{285}\ [\bar{J}^k_{gu}(+h/2) - \bar{J}^k_{gv}(-h/2)] \\
&+ \frac{2}{285}\ [\bar{J}^k_{gv}(+h/2) - \bar{J}^k_{gu}(-h/2)] + \bar{J}^{in,k}_{gx}(+h/2).
\end{aligned} \tag{A.28}$$

(2) The nodal flux $\bar{\phi}^k_g$ is obtained from Eq. (2.74):

$$\bar{\phi}^k_g = \frac{h}{h\Sigma^{r,k}_g}\ \bar{Q}^k_g - \frac{2}{3h\Sigma^{r,k}_g}\ [\bar{L}^k_{gx} + \bar{L}^k_{gu} + \bar{L}^k_{gv}], \tag{A.29}$$

while the flux moment ϕ^k_{gx1} satisfies Eq. (2.70) [with a^k_{gx1} evaluated using Eq. (2.34a)]:

$$\begin{aligned}
\phi^k_{gx1} = &\frac{h}{\alpha^k_{g1}}\ Q^k_{gx1} - \frac{2}{3\alpha^k_{g1}}\ [\bar{T}^k_{gx} + \bar{T}^k_{gu} - \bar{T}^k_{gv}] \\
&+ \frac{40}{9\alpha^k_{g1}}\ \frac{D^k_g}{h}\ [\bar{\phi}^k_{gx}(+h/2) - \bar{\phi}^k_{gx}(-h/2)],
\end{aligned} \tag{A.30}$$

where

$$\alpha_{g1}^{k} \equiv h\Sigma_{g}^{r,k} + 32\,\frac{D_{g}^{k}}{h}\,. \tag{A.31}$$

Substituting Eqs. (A.29) and (A.30) into Eq. (A.28) and collecting terms yields

$$\begin{aligned}\bar{J}_{gx}^{out,k}(+h/2) = -\{&\tfrac{1}{2}\,\tau_1\,\bar{\phi}_{gx}^{k}(+h/2) + \tfrac{1}{2}\,\tau_2\,\bar{\phi}_{gx}^{k}(-h/2) + \tau_3\,[\bar{L}_{gx}^{k} + \bar{L}_{gu}^{k} + \bar{L}_{gv}^{k}]\\ &+ \tau_4\,[\bar{L}_{gu}^{k} + \bar{L}_{gv}^{k}] + \tau_5\,[\bar{J}_{gu}^{k}(+h/2) - \bar{J}_{gv}^{k}(-h/2)]\\ &+ \tau_6\,[\bar{J}_{gv}^{k}(+h/2) - \bar{J}_{gu}^{k}(-h/2)] + \tau_7\,[\bar{T}_{gx}^{k} + \bar{T}_{gu}^{k} - \bar{T}_{gv}^{k}]\}\\ &+ \tau_8\,\bar{Q}_{g}^{k} + \tau_9\,Q_{gx1}^{k} + \bar{J}_{gx}^{in,k}(+h/2),\end{aligned} \tag{A.32}$$

where

$$\tau_1 \equiv \frac{2D_{g}^{k}}{h}\left\{\frac{49}{13} - \frac{1299}{5187}\,\beta_1 + \left[\frac{8}{3} - \frac{160}{3}\,\kappa_{g1}^{k}\right]\beta_2\right\} \tag{A.33a}$$

$$\tau_2 \equiv \frac{2D_{g}^{k}}{h}\left\{\frac{23}{13} - \frac{753}{5187}\,\beta_1 - \left[\frac{8}{3} - \frac{160}{3}\,\kappa_{g1}^{k}\right]\beta_2\right\} \tag{A.33b}$$

$$\tau_3 \equiv \frac{2}{3}\,\kappa_{g0}^{k}\left[\frac{72}{13} - \frac{2052}{5187}\,\beta_1\right] \tag{A.33c}$$

$$\tau_4 \equiv -\frac{4}{105}\,\beta_1 \tag{A.33d}$$

$$\tau_5 \equiv -\frac{17}{285}\,\beta_1 \tag{A.33e}$$

$$\tau_6 \equiv -\frac{2}{285}\,\beta_1 \tag{A.33f}$$

$$\tau_7 \equiv 8\,\kappa_{g1}^k\,\beta_2 \tag{A.33g}$$

$$\tau_8 \equiv \frac{3h}{2}\,\tau_3 \tag{A.33h}$$

$$\tau_9 \equiv \frac{3h}{2}\,\tau_7, \tag{A.33i}$$

and

$$\kappa_{g0}^k \equiv \frac{D_g^k/h}{h\Sigma_g^{r,k}} \tag{A.34a}$$

$$\kappa_{g1}^k \equiv \frac{D_g^k/h}{\alpha_{g1}^k}\ . \tag{A.34b}$$

(3) The surface-averaged fluxes, net currents, and leakages on the right hand side of Eq. (A.32) are eliminated in favor of partial currents using the relationships

$$\bar{\phi}_{gx}^k(\pm h/2) = 2\,[\bar{J}_{gx}^{out,k}(\pm h/2) + \bar{J}_{gx}^{in,k}(\pm h/2)] \tag{A.35a}$$

$$\bar{J}_{gx}^k(+h/2) = \bar{J}_{gx}^{out,k}(+h/2) - \bar{J}_{gx}^{in,k}(+h/2) \tag{A.35b}$$

$$\bar{J}_{gx}^k(-h/2) = \bar{J}_{gx}^{in,k}(-h/2) - \bar{J}_{gx}^{out,k}(-h/2) \tag{A.35c}$$

$$\bar{L}_{gx}^k = \bar{J}_{gx}^{out,k}(+h/2) - \bar{J}_{gx}^{in,k}(+h/2) + \bar{J}_{gx}^{out,k}(-h/2) - \bar{J}_{gx}^{in,k}(-h/2) \tag{A.35d}$$

$$\bar{T}_{gx}^k = \bar{J}_{gx}^{out,k}(+h/2) - \bar{J}_{gx}^{in,k}(+h/2) - \bar{J}_{gx}^{out,k}(-h/2) + \bar{J}_{gx}^{in,k}(-h/2). \tag{A.35e}$$

Analogous expressions are used to eliminate the corresponding u- and v-direction terms. Substituting Eqs. (A.35) into Eq. (A.32) and then collecting terms yields

$$[a_1\ a_2\ a_3\ a_4\ a_3\ a_2]\ \underline{J}_g^{out,k} = [b_1\ b_2] \begin{bmatrix} \bar{Q}_g^k \\ Q_{gx1}^k \end{bmatrix}$$

$$+ [c_1\ c_2\ c_3\ c_4\ c_3\ c_2]\ \underline{J}_g^{in,k}\ , \qquad \text{(A.36)}$$

where $\underline{J}_g^{out,k}$ and $\underline{J}_g^{in,k}$ are column vectors containing the six outgoing and six incoming partial currents, respectively, for the k-th node, e.g.

$$\underline{J}_g^{out,k} \equiv \text{col}\ [J_{gx}^{out,k}(+h/2),\ J_{gu}^{out,k}(+h/2),\ J_{gv}^{out,k}(+h/2),\ J_{gx}^{out,k}(-h/2),$$

$$J_{gu}^{out,k}(-h/2),\ J_{gv}^{out,k}(-h/2)]. \qquad \text{(A.37)}$$

The constants introduced in Eq. (A.36) are defined as follows:

$$a_1 \equiv 1 + \tau_1 + \tau_3 + \tau_7 \qquad \text{(A.38a)}$$

$$a_2 \equiv \tau_3 + \tau_4 + \tau_5 + \tau_7 \qquad \text{(A.38b)}$$

$$a_3 \equiv \tau_3 + \tau_4 + \tau_6 - \tau_7 \qquad \text{(A.38c)}$$

$$a_4 \equiv \tau_2 + \tau_3 - \tau_7 \qquad \text{(A.38d)}$$

$$b_1 \equiv \tau_8 \qquad \text{(A.39a)}$$

$$b_2 \equiv \tau_9 \qquad \text{(A.39b)}$$

$$c_1 \equiv 1 - \tau_1 + \tau_3 + \tau_7 \tag{A.40a}$$

$$c_2 \equiv a_2 \tag{A.40b}$$

$$c_3 \equiv a_3 \tag{A.40c}$$

$$c_4 \equiv -\tau_2 + \tau_3 - \tau_7 \, . \tag{A.40d}$$

(4) Five additional equations similar to Eq. (A.36) can be obtained by applying successive 60° rotational transformations to Eq. (A.36). These equations can be combined with Eq. (A.36) to yield

$$[A_g^k] \, \underline{J}_g^{out,k} = [B_g^k] \, \underline{Q}_g^k + [C_g^k] \, \underline{J}_g^{in,k} \, , \tag{A.41}$$

where

$$\underline{Q}_g^k \equiv \text{col} \, [\bar{Q}_g^k, \, Q_{gxl}^k, \, Q_{gul}^k, \, Q_{gvl}^k] \tag{A.42}$$

$$[A_g^k] \equiv \begin{bmatrix} a_1 & a_2 & a_3 & a_4 & a_3 & a_2 \\ a_2 & a_1 & a_2 & a_3 & a_4 & a_3 \\ a_3 & a_2 & a_1 & a_2 & a_3 & a_4 \\ a_4 & a_3 & a_2 & a_1 & a_2 & a_3 \\ a_3 & a_4 & a_3 & a_2 & a_1 & a_2 \\ a_2 & a_3 & a_4 & a_3 & a_2 & a_1 \end{bmatrix} \tag{A.43}$$

$$[B_g^k] \equiv \begin{bmatrix} b_1 & b_2 & 0 & 0 \\ b_1 & 0 & b_2 & 0 \\ b_1 & 0 & 0 & b_2 \\ b_1 & -b_2 & 0 & 0 \\ b_1 & 0 & -b_2 & 0 \\ b_1 & 0 & 0 & -b_2 \end{bmatrix} \tag{A.44}$$

and

$$[C_g^k] \equiv \begin{bmatrix} c_1 & c_2 & c_3 & c_4 & c_3 & c_2 \\ c_2 & c_1 & c_2 & c_3 & c_4 & c_3 \\ c_3 & c_2 & c_1 & c_2 & c_3 & c_4 \\ c_4 & c_3 & c_2 & c_1 & c_2 & c_3 \\ c_3 & c_4 & c_3 & c_2 & c_1 & c_2 \\ c_2 & c_3 & c_4 & c_3 & c_2 & c_1 \end{bmatrix} . \tag{A.45}$$

Note that $[A_g^k]$ and $[C_g^k]$ are symmetric matrices with structures consistent with the 60° transformations used to generate the u- and v-direction analogs of Eq. (A.36). The negative entries in $[B_g^k]$ appear since Q_{gx1}^k is an odd spatial moment over the interval $x\varepsilon[-h/2,+h/2]$.

(5) The final form of the response matrix equation is obtained by inverting $[A_g^k]$ in Eq. (A.41) to yield

$$\underline{J}_g^{out,k} = [P_g^k]\ \underline{Q}_g^k + [R_g^k]\ \underline{J}_g^{in,k} , \tag{A.46}$$

where

$$[P_g^k] \equiv [A_g^k]^{-1}\ [B_g^k] \tag{A.47}$$

$$[R_g^k] \equiv [A_g^k]^{-1}\ [C_g^k]. \tag{A.48}$$

The structures of the response matrix $[R_g^k]$ and the source matrix $[P_g^k]$ can be deduced from symmetry considerations:

$$[R_g^k] \equiv \begin{bmatrix} r & t_{60} & t_{120} & t_{180} & t_{120} & t_{60} \\ t_{60} & r & t_{60} & t_{120} & t_{180} & t_{120} \\ t_{120} & t_{60} & r & t_{60} & t_{120} & t_{180} \\ t_{180} & t_{120} & t_{60} & r & t_{60} & t_{120} \\ t_{120} & t_{180} & t_{120} & t_{60} & r & t_{60} \\ t_{60} & t_{120} & t_{180} & t_{120} & t_{60} & r \end{bmatrix} \tag{A.49}$$

$$[P_g^k] = \begin{bmatrix} p_0 & p_1 & p_2 & -p_2 \\ p_0 & p_2 & p_1 & p_2 \\ p_0 & -p_2 & p_2 & p_1 \\ p_0 & -p_1 & -p_2 & p_2 \\ p_0 & -p_2 & -p_1 & -p_2 \\ p_0 & p_2 & -p_2 & -p_1 \end{bmatrix} . \qquad \text{(A.50)}$$

The entries in these matrices have the following physical interpretations:

$r \equiv$ reflection coefficient

$t_{60} \equiv$ transmission coefficient between two surfaces oriented at 60°

$t_{120} \equiv$ transmission coefficient between two surfaces oriented at 120°

$t_{180} \equiv$ transmission coefficient between two surfaces oriented at 180°

$p_0 \equiv$ zero-moment source coefficient specifying contribution to an outgoing partial current from the node-averaged group source term

$p_1 \equiv$ first-moment source coefficient specifying contribution to an outgoing partial current in a given direction from the first-moment group source term in the same direction

$p_2 \equiv$ first-moment source coefficient specifying contribution to an outgoing partial current in a given direction from the first-moment group source term in a different direction.

Note that these coefficients are defined for a single energy group g, and include only effects due to in-group diffusion and removal. Group to group transfer due to fission and in-scatter are included in the source term Q_g^k appearing in Eq. (A.46). The entries of $[R_g^k]$ and $[P_g^k]$ are computed in the following manner. Let $\underline{m}^T$ denote the first row of the inverse of the $[A_g^k]$ matrix defined in Eq. (A.43). Comparison of Eqs. (A.48) and (A.47) with Eqs. (A.49) and (A.50) yields

$$r = \underline{m}^T [c_1\ c_2\ c_3\ c_4\ c_3\ c_2]^T \tag{A.51a}$$

$$t_{60} = \underline{m}^T [c_2\ c_1\ c_2\ c_3\ c_4\ c_3]^T \tag{A.51b}$$

$$t_{120} = \underline{m}^T [c_3\ c_2\ c_1\ c_2\ c_3\ c_4]^T \tag{A.51c}$$

$$t_{180} = \underline{m}^T [c_4\ c_3\ c_2\ c_1\ c_2\ c_3]^T \tag{A.51d}$$

$$p_0 = \underline{m}^T [b_1\ b_1\ b_1\ b_1\ b_1\ b_1]^T \tag{A.51e}$$

$$p_1 = \underline{m}^T [b_2\ 0\ 0\ -b_2\ 0\ 0]^T \tag{A.51f}$$

$$p_2 = \underline{m}^T [0\ b_2\ 0\ 0\ -b_2\ 0]^T. \tag{A.51g}$$

Inspection of Eqs. (A.33) shows that the 7 coefficients given in Eqs. (A.51) depend only upon the diffusion coefficient D_g^k and the removal cross section $\Sigma_g^{r,k}$ in the k-th node and g-th energy group. Hence these coefficients are computed and stored only for unique nodes characterized by their material composition assignment.

APPENDIX B
DERIVATION OF THE THREE-DIMENSIONAL RESPONSE MATRIX EQUATION

In this Appendix we provide additional details of the steps leading from the expressions [Eqs. (3.50) and (3.51)] for the interface partial currents to the final form [Eq. (3.58)] of the three-dimensional response matrix equation.

As in Section A.3 of Appendix A, Eq. (3.50) is rewritten in the form

$$J_{gx}^{out,k}(+h/2) = -\frac{D_g^k}{h}\left\{a_{gx1}^k + \frac{36}{13}a_{gx2}^k + \left[\frac{7}{26}a_{gx3}^k + E_{gx}^k(h/2)\right]\beta_1 + \frac{1}{2}\beta_2\, a_{gx4}^k\right\} + \tilde{J}_{gx}^{in,k}(+h/2), \tag{B.1}$$

where the constants β_1 and β_2 are defined in Eq. (A.24). Similarly, an additional constant β_3 is introduced in order to distinguish the approximations obtained for $N_z = 2,3$ in Eq. (3.29). The expression [Eq. (3.51)] for the outgoing surface-averaged partial current across the surface in the positive z-direction is then

$$J_{gz}^{out,k}(+\Delta z^k/2) = -\frac{D_g^k}{\Delta z^k}\left[a_{gz1}^k + 3a_{gz2}^k + \frac{1}{2}\beta_3\, a_{gz3}^k\right] + J_{gz}^{in,k}(+\Delta z^k/2), \tag{B.2}$$

where

$$\begin{aligned} N_z = 2 &\Rightarrow \beta_3 \equiv 0 \\ N_z = 3 &\Rightarrow \beta_3 \equiv 1. \end{aligned} \tag{B.3}$$

The derivation of the final form of the three-dimensional response matrix equation follows the five steps described in Section 3.5. We repeat these steps in more detail here, making use of the results derived in Appendix A.

(1) The elimination of the expansion coefficients in Eq. (B.1) is discussed in Section A.3. The result is identical to the two-dimensional result given in Eq. (A.28).

The elimination of the expansion coefficients in Eq. (B.2) proceeds in the following manner. Using Eqs. (3.30a) and (3.30b) yields:

$$a^k_{gz1} + 3a^k_{gz2} = 4\bar{\phi}^k_{gz}(+\Delta z^k/2) + 2\bar{\phi}^k_{gz}(-\Delta z^k/2) - 6\bar{\phi}^k_g \,. \tag{B.4}$$

Using Eq. (3.37) yields:

$$\frac{1}{2}\, a^k_{gz3} = -60\ \phi^k_{gz1} + 5[\bar{\phi}^k_{gz}(+\Delta z^k/2) - \bar{\phi}^k_{gz}(-\Delta z^k/2)]. \tag{B.5}$$

Substituting Eqs. (B.4) and (B.5) into Eq. (B.2) and collecting terms yields

$$\begin{aligned}\bar{J}^{out,k}_{gz}(+\Delta z^k/2) = -\frac{D^k_g}{\Delta z^k}\{&[4 + 5\beta_3]\ \bar{\phi}^k_{gz}(+\Delta z^k/2) \\ &+ [2 - 5\beta_3]\ \bar{\phi}^k_{gz}(-\Delta z^k/2) - 6\bar{\phi}^k_g - 60\beta_3\ \phi^k_{gz1}\} \\ &+ \bar{J}^{in,k}_{gz}(+\Delta z^k/2).\end{aligned} \tag{B.6}$$

(2) The nodal flux $\bar{\phi}^k_g$ is obtained from Eq. (3.38):

$$\bar{\phi}^k_g = \frac{1}{\Sigma^{r,k}_g}\,\bar{Q}^k_g - \frac{2}{3h\Sigma^{r,k}_g}\,[\bar{L}^k_{gx} + \bar{L}^k_{gu} + \bar{L}^k_{gv}] - \frac{1}{\Delta z^k\ \Sigma^{r,k}_g}\,\bar{L}^k_{gz}, \tag{B.7}$$

while the flux moments ϕ^k_{gx1} and ϕ^k_{gz1} satisfy Eqs. (3.39) and (3.44) [with a^k_{gx1} and a^k_{gz1} evaluated using Eqs. (2.34a) and (3.30a)]:

$$\begin{aligned}\phi^k_{gx1} = \frac{h}{\alpha^k_{g1}}\,[Q^k_{gx1} - \frac{1}{\Delta z^k}\,L^k_{gzx1}] - \frac{2}{3\alpha^k_{g1}}\,[\bar{T}^k_{gx} + \bar{T}^k_{gu} - \bar{T}^k_{gv}] \\ + \frac{40}{9\alpha^k_{g1}}\,\frac{D^k_g}{h}\,[\bar{\phi}^k_{gx}(+h/2) - \bar{\phi}^k_{gx}(-h/2)],\end{aligned} \tag{B.8}$$

$$\phi_{gz1}^{k} = \frac{1}{\Sigma_g^{r,k}} [Q_{gz1}^{k} - \frac{2}{3h} L_{gxyz1}^{k}] - \frac{1}{2} \frac{1}{\Delta z^{k} \Sigma_g^{r,k}} \bar{T}_{gz}^{k}$$

$$- \frac{D_g^{k}}{\Delta z^{k}} \frac{1}{\Delta z^{k} \Sigma_g^{r,k}} [\bar{\phi}_{gz}^{k}(+\Delta z^{k}/2) - \bar{\phi}_{gz}^{k}(-\Delta z^{k}/2)]. \qquad (B.9)$$

Substitution of Eqs. (B.7) and (B.8) into Eq. (A.28) and collecting terms yields

$$\bar{J}_{gx}^{out,k}(+h/2) = - \{\frac{1}{2} \tau_1 \bar{\phi}_{gx}^{k}(+h/2) + \frac{1}{2} \tau_2 \bar{\phi}_{gx}^{k}(-h/2) + \tau_3 [\bar{L}_{gx}^{k} + \bar{L}_{gu}^{k} + \bar{L}_{gv}^{k}]$$

$$+ \tau_{10} \bar{L}_{gz}^{k} + \tau_4 [\bar{L}_{gu}^{k} + \bar{L}_{gv}^{k}]$$

$$+ \tau_5 [\bar{J}_{gu}^{k}(+h/2) - \bar{J}_{gv}^{k}(-h/2)]$$

$$+ \tau_6 [\bar{J}_{gv}^{k}(+h/2) - \bar{J}_{gu}^{k}(-h/2)] + \tau_7 [\bar{T}_{gx}^{k} + \bar{T}_{gu}^{k} - \bar{T}_{gv}^{k}]\}$$

$$+ \tau_8 \bar{Q}_g^{k} + \tau_9 [Q_{gx1}^{k} - \frac{1}{\Delta z^{k}} L_{gxy1}^{k}] + \bar{J}_{gx}^{in,k}(+h/2), \qquad (B.10)$$

where τ_1 through τ_9 are defined in Eqs. (A.33), and

$$\tau_{10} \equiv \frac{1}{\Delta z^{k}} \tau_8 . \qquad (B.11)$$

Substituting Eqs. (B.7) and (B.9) into Eq. (B.6) and collecting terms yields

$$J_{gz}^{out,k}(+\Delta z^k/2) = -\{\frac{1}{2}\tau_{z1}\,\bar{\phi}_{gz}^{k}(+\Delta z^k/2) + \frac{1}{2}\tau_{z2}\,\bar{\phi}_{gz}^{k}(-\Delta z^k/2)$$

$$+ \tau_{z3}\,\bar{L}_{gz}^{k} + \tau_{z4}\,[\bar{L}_{gx}^{k} + \bar{L}_{gu}^{k} + \bar{L}_{gv}^{k}] + \tau_{z5}\,\bar{T}_{gz}^{k}\}$$

$$+ \tau_{z6}\,\bar{Q}_{g}^{k} + \tau_{z7}\,[Q_{gz1}^{k} - \frac{2}{3h}\,L_{gxyz1}^{k}] + \bar{J}_{gz}^{in,k}(+\Delta z^k/2), \qquad (B.12)$$

where

$$\tau_{z1} \equiv \frac{2D_g^k}{\Delta z^k}\{4 + [5 + 60\,\kappa_{gz0}^{k}]\,\beta_3\} \qquad (B.13a)$$

$$\tau_{z2} \equiv \frac{2D_g^k}{\Delta z^k}\{2 - [5 + 60\,\kappa_{gz0}^{k}]\,\beta_3\} \qquad (B.13b)$$

$$\tau_{z3} \equiv 6\,\kappa_{gz0}^{k} \qquad (B.13c)$$

$$\tau_{z4} \equiv \frac{2}{3}\frac{\Delta z^k}{h}\,\tau_{z3} \qquad (B.13d)$$

$$\tau_{z5} \equiv 30\,\kappa_{gz0}^{k}\,\beta_3 \qquad (B.13e)$$

$$\tau_{z6} \equiv \Delta z^k\,\tau_{z3} \qquad (B.13f)$$

$$\tau_{z7} \equiv 60\,\Delta z^k\,\kappa_{gz0}^{k}, \qquad (B.13g)$$

and

$$\kappa_{gz0}^{k} \equiv \frac{D_g^k/\Delta z^k}{\Delta z^k\,\Sigma_g^{r,k}}\,. \qquad (B.14)$$

(3) The surface-averaged fluxes, net currents, and leakages on the right hand sides of Eqs. (B.10) and (B.12) are eliminated in favor of partial currents using the relationships shown in Eqs. (A.35) and their u-, v-, and z-direction analogs. Equations (B.10) and (B.11) can then be written as

$$[a_1\ a_2\ a_3\ a_4\ a_3\ a_2\ a_5\ a_5]\ \underline{J}_g^{out,k} = [b_1\ b_2] \begin{bmatrix} \bar{Q}_g^k \\ Q_{gx1}^k - \frac{1}{\Delta z^k} L_{gzx1}^k \end{bmatrix}$$

$$+ [c_1\ c_2\ c_3\ c_4\ c_3\ c_2\ c_5\ c_5]\ \underline{J}_g^{in,k} \qquad \text{(B.15)}$$

and

$$[a_6\ a_6\ a_6\ a_6\ a_6\ a_6\ a_7\ a_8]\ \underline{J}_g^{out,k} = [b_3\ b_4] \begin{bmatrix} \bar{Q}_g^k \\ Q_{gz1}^k - \frac{2}{3h} L_{gxyz1}^k \end{bmatrix}$$

$$+ [c_6\ c_6\ c_6\ c_6\ c_6\ c_6\ c_7\ c_8]\ \underline{J}_g^{in,k}, \qquad \text{(B.16)}$$

respectively, where $\underline{J}_g^{out,k}$ and $\underline{J}_g^{in,k}$ are column vectors containing the eight outgoing and eight incoming partial currents, respectively, for the k-th node, e.g.

$$\underline{J}_g^{out,k} \equiv \text{col}\ [\bar{J}_{gx}^{out,k}(+h/2),\ J_{gu}^{out,k}(+h/2),\ J_{gv}^{out,k}(+h/2),\ J_{gx}^{out,k}(-h/2),$$

$$J_{gu}^{out,k}(-h/2),\ J_{gv}^{out,k}(-h/2),\ J_{gz}^{out,k}(+\Delta z^k/2),\ J_{gz}^{out,k}(-\Delta z^k/2)]. \qquad \text{(B.17)}$$

Those constants introduced in Eqs. (B.15) and (B.16) that are not given in Eqs. (A.38) through (A.40) are defined as follows:

$$a_5 \equiv \tau_{10} \qquad \text{(B.18a)}$$

$$a_6 \equiv \tau_{z4} \qquad \text{(B.18b)}$$

$$a_7 \equiv 1 + \tau_{z1} + \tau_{z3} + \tau_{z5} \tag{B.18c}$$

$$a_8 \equiv \tau_{z2} + \tau_{z3} - \tau_{z5} \tag{B.18d}$$

$$b_3 \equiv \tau_{z6} \tag{B.19a}$$

$$b_4 \equiv \tau_{z7} \tag{B.19b}$$

$$c_5 \equiv \tau_{10} \tag{B.20a}$$

$$c_6 \equiv \tau_{z4} \tag{B.20b}$$

$$c_7 \equiv 1 - \tau_{z1} + \tau_{z3} + \tau_{z5} \tag{B.20c}$$

$$c_8 \equiv - \tau_{z2} + \tau_{z3} - \tau_{z5}. \tag{B.20d}$$

(4) Five additional equations similar to Eq. (B.15) can be obtained by applying successive 60° rotational transformations to Eq. (B.15). Calculation of $\bar{J}_{gz}^{out,k}(-\Delta z^k/2)$ yields an additional equation similar to Eq. (B.16). These additional equations can be combined with Eqs. (B.15) and (B.16) to yield

$$[A_g^k]\ \underline{J}_g^{out,k} = [B_g^k]\ \{\underline{Q}_g^k - \underline{L}_g^k\} + [C_g^k]\ \underline{J}_g^{in,k}, \tag{B.21}$$

where

$$\underline{Q}_g^k \equiv \text{col}\ [\bar{Q}_g^k,\ Q_{gx1}^k,\ Q_{gu1}^k,\ Q_{gv1}^k,\ Q_{gz1}^k] \tag{B.22}$$

$$\underline{L}_g^k \equiv \text{col}\ [0,\ \frac{1}{\Delta z^k} L_{gzx1}^k,\ \frac{1}{\Delta z^k} L_{gzu1}^k,\ \frac{1}{\Delta z^k} L_{gzv1}^k,\ \frac{2}{3h} L_{gxyz1}^k] \tag{B.23}$$

$$[A_g^k] \equiv \begin{bmatrix} a_1 & a_2 & a_3 & a_4 & a_3 & a_2 & a_5 & a_5 \\ a_2 & a_1 & a_2 & a_3 & a_4 & a_3 & a_5 & a_5 \\ a_3 & a_2 & a_1 & a_2 & a_3 & a_4 & a_5 & a_5 \\ a_4 & a_3 & a_2 & a_1 & a_2 & a_3 & a_5 & a_5 \\ a_3 & a_4 & a_3 & a_2 & a_1 & a_2 & a_5 & a_5 \\ a_2 & a_3 & a_4 & a_3 & a_2 & a_1 & a_5 & a_5 \\ a_6 & a_6 & a_6 & a_6 & a_6 & a_6 & a_7 & a_8 \\ a_6 & a_6 & a_6 & a_6 & a_6 & a_6 & a_8 & a_7 \end{bmatrix} \qquad \text{(B.24)}$$

$$[B_g^k] \equiv \begin{bmatrix} b_1 & b_2 & 0 & 0 & 0 \\ b_1 & 0 & b_2 & 0 & 0 \\ b_1 & 0 & 0 & b_2 & 0 \\ b_1 & -b_2 & 0 & 0 & 0 \\ b_1 & 0 & -b_2 & 0 & 0 \\ b_1 & 0 & 0 & -b_2 & 0 \\ b_3 & 0 & 0 & 0 & b_4 \\ b_3 & 0 & 0 & 0 & -b_4 \end{bmatrix} \qquad \text{(B.25)}$$

and

$$[C_g^k] \equiv \begin{bmatrix} c_1 & c_2 & c_3 & c_4 & c_3 & c_2 & c_5 & c_5 \\ c_2 & c_1 & c_2 & c_3 & c_4 & c_3 & c_5 & c_5 \\ c_3 & c_2 & c_1 & c_2 & c_3 & c_4 & c_5 & c_5 \\ c_4 & c_3 & c_2 & c_1 & c_2 & c_3 & c_5 & c_5 \\ c_3 & c_4 & c_3 & c_2 & c_1 & c_2 & c_5 & c_5 \\ c_2 & c_3 & c_4 & c_3 & c_2 & c_1 & c_5 & c_5 \\ c_6 & c_6 & c_6 & c_6 & c_6 & c_6 & c_7 & c_8 \\ c_6 & c_6 & c_6 & c_6 & c_6 & c_6 & c_8 & c_7 \end{bmatrix}. \qquad \text{(B.26)}$$

(5) The final form of the three-dimensional response matrix equation is obtained by inverting $[A_g^k]$ in Eq. (B.21) to yield

$$\underline{J}_g^{out,k} = [P_g^k] \{\underline{Q}_g^k - \underline{L}_g^k\} + [R_g^k] \underline{J}_g^{in,k}, \qquad \text{(B.27)}$$

where

$$[P_g^k] \equiv [A_g^k]^{-1} [B_g^k] \qquad \text{(B.28)}$$

$$[R_g^k] \equiv [A_g^k]^{-1} [C_g^k]. \qquad \text{(B.29)}$$

The structures of the response matrix $[R_g^k]$ and the source matrix $[P_g^k]$ can be deduced from symmetry considerations:

$$[R_g^k] \equiv \left[\begin{array}{cccccc|cc} r & t_{60} & t_{120} & t_{180} & t_{120} & t_{60} & t_{90}^{z\to xy} & t_{90}^{z\to xy} \\ t_{60} & r & t_{60} & t_{120} & t_{180} & t_{120} & t_{90}^{z\to xy} & t_{90}^{z\to xy} \\ t_{120} & t_{60} & r & t_{60} & t_{120} & t_{180} & t_{90}^{z\to xy} & t_{90}^{z\to xy} \\ t_{180} & t_{120} & t_{60} & r & t_{60} & t_{120} & t_{90}^{z\to xy} & t_{90}^{z\to xy} \\ t_{120} & t_{180} & t_{120} & t_{60} & r & t_{60} & t_{90}^{z\to xy} & t_{90}^{z\to xy} \\ t_{60} & t_{120} & t_{180} & t_{120} & t_{60} & r & t_{90}^{z\to xy} & t_{90}^{z\to xy} \\ \hline t_{90}^{xy\to z} & t_{90}^{xy\to z} & t_{90}^{xy\to z} & t_{90}^{xy\to z} & t_{90}^{xy\to z} & t_{90}^{xy\to z} & r^z & t_{180}^z \\ t_{90}^{xy\to z} & t_{90}^{xy\to z} & t_{90}^{xy\to z} & t_{90}^{xy\to z} & t_{90}^{xy\to z} & t_{90}^{xy\to z} & t_{180}^z & r^z \end{array}\right]$$

$$\equiv \begin{bmatrix} [R_{gxy}^k] & [R_{gxyz}^k] \\ [R_{gzxy}^k] & [R_{gz}^k] \end{bmatrix} , \qquad \text{(B.30)}$$

$$[P_g^k] \equiv \left[\begin{array}{ccccc} p_0 & p_1 & p_2 & -p_2 & 0 \\ p_0 & p_2 & p_1 & p_2 & 0 \\ p_0 & -p_2 & p_2 & p_1 & 0 \\ p_0 & -p_1 & -p_2 & p_2 & 0 \\ p_0 & -p_2 & -p_1 & -p_2 & 0 \\ p_0 & p_2 & -p_2 & -p_1 & 0 \\ \hline p_0^z & 0 & 0 & 0 & p_1^z \\ p_0^z & 0 & 0 & 0 & -p_1^z \end{array}\right] \equiv \begin{bmatrix} [P_{gxy}^k] \\ [P_{gz}^k] \end{bmatrix} . \qquad \text{(B.31)}$$

The additional entries in the three-dimensional forms of $[R_g^k]$ and $[P_g^k]$ have the following physical interpretations:

$t_{90}^{z\to xy}$ ≡ transmission coefficient from an axial surface to a hex-plane surface

$t_{90}^{xy\to z}$ ≡ transmission coefficient from a hex-plane surface to an axial surface

r^z ≡ reflection coefficient for axial surfaces

t_{180}^z ≡ transmission coefficient between axial surfaces

p_0^z ≡ axial zero-moment source coefficient specifying contribution to an outgoing partial current on an axial surface from the node-averaged group source term.

p_1^z ≡ axial first-moment source coefficient specifying contribution to an outgoing partial current on an axial surface from the axial first-moment group source term.

The entries of $[R_g^k]$ and $[P_g^k]$ are computed in the following manner. Let $\underline{m}_1^T$ and $\underline{m}_7^T$ denote the first and seventh rows of the inverse of the $[A_g^k]$ matrix defined in Eq. (B.24). Comparison of Eqs. (B.29) and (B.28) with Eqs. (B.30) and (B.31) yields

$$r = \underline{m}_1^T [c_1\ c_2\ c_3\ c_4\ c_3\ c_2\ c_5\ c_5]^T \tag{B.32a}$$

$$t_{60} = \underline{m}_1^T [c_2\ c_1\ c_2\ c_3\ c_4\ c_3\ c_5\ c_5]^T \tag{B.32b}$$

$$t_{120} = \underline{m}_1^T [c_3\ c_2\ c_1\ c_2\ c_3\ c_4\ c_5\ c_5]^T \tag{B.32c}$$

$$t_{180} = \underline{m}_1^T [c_4\ c_3\ c_2\ c_1\ c_2\ c_3\ c_5\ c_5]^T \tag{B.32d}$$

$$t_{90}^{z\to xy} = \underline{m}_1^T [c_5\ c_5\ c_5\ c_5\ c_5\ c_5\ c_7\ c_8]^T \tag{B.32e}$$

$$t_{90}^{xy+z} = \underline{m}_7^T [c_1\ c_2\ c_3\ c_4\ c_3\ c_2\ c_6\ c_6]^T \tag{B.32f}$$

$$r_z = \underline{m}_7^T [c_5\ c_5\ c_5\ c_5\ c_5\ c_5\ c_7\ c_8]^T \tag{B.32g}$$

$$t_{180}^{z} = \underline{m}_7^T [c_5\ c_5\ c_5\ c_5\ c_5\ c_5\ c_8\ c_7]^T \tag{B.32h}$$

$$p_0 = \underline{m}_1^T [b_1\ b_1\ b_1\ b_1\ b_1\ b_1\ b_3\ b_3]^T \tag{B.32i}$$

$$p_1 = \underline{m}_1^T [b_2\ 0\ 0\ -b_2\ 0\ 0\ 0\ 0]^T \tag{B.32j}$$

$$p_2 = \underline{m}_1^T [0\ b_2\ 0\ 0\ -b_2\ 0\ 0\ 0]^T \tag{B.32k}$$

$$p_0^z = \underline{m}_7^T [b_1\ b_1\ b_1\ b_1\ b_1\ b_1\ b_3\ b_3]^T \tag{B.32l}$$

$$p_1^z = \underline{m}_7^T [0\ 0\ 0\ 0\ 0\ 0\ b_4\ -b_4]^T. \tag{B.32m}$$

Thus, in three dimensions, a total of 13 coefficients are computed and stored for each unique node characterized by its material composition assignment and axial mesh spacing.

APPENDIX C
APPROXIMATION OF THE LEAKAGE MOMENTS

In this Appendix we provide additional details concerning the approximation of the leakage moments which appear in the three-dimensional response matrix equation, and then summarize results for a model problem study designed to isolate the errors associated with these approximations.

C.1 Calculation of the Leakage Moments

As discussed in Section 3.6, the leakage moments are calculated using the approximations

$$L^k_{gz}(x,y) \cong \bar{L}^k_{gz} \tag{C.1}$$

$$L^k_{gxy}(z) \cong \rho^k_{gxy}(z), \qquad z \in \Delta z^k, \tag{C.2}$$

where

$$\rho^k_{gxy}(z) \equiv \bar{L}^k_{gxy} + \rho^k_{gxy1}\, f_{z1}(z) + \rho^k_{gxy2}\, f_{z2}(z), \quad z\in[z_1, z_2]. \tag{C.3}$$

The expansion coefficients ρ^k_{gxy1} and ρ^k_{gxy2} are calculated using the constraints given in Eqs. (3.66). The results are

$$\rho^k_{gxy1} \equiv \frac{2}{3h}\frac{V^k}{d}\{[2\Delta z^{k-} + \Delta z^k][\Delta z^{k-} + \Delta z^k][\bar{L}^{k+}_{gxy} - \bar{L}^k_{gxy}]$$

$$+ [\Delta z^k + \Delta z^{k+}][\Delta z^k + 2\Delta z^{k+}][\bar{L}^k_{gxy} - \bar{L}^{k-}_{gxy}]\} \tag{C.4a}$$

$$\rho^k_{gxy2} \equiv \frac{2\Delta z^k}{3h}\frac{V^k}{d}\{[\Delta z^{k-} + \Delta z^k][\bar{L}^{k+}_{gxy} - \bar{L}^k_{gxy}]$$

$$- [\Delta z^k + \Delta z^{k+}][\bar{L}^k_{gxy} - \bar{L}^{k-}_{gxy}]\}, \tag{C.4b}$$

where d is defined in Eq. (3.69c). Substituting Eq. (C.4a) into Eq. (3.67) yields the final result for L^{k}_{gxyl} shown in Eq. (3.68).

For nodes adjacent to an outer reactor boundary (with vacuum boundary conditions), the quadratic leakage approximation is constructed such that

$$L^{\ell}_{gxy}(\Delta z^{\ell}/2) \equiv 0, \tag{C.5}$$

where ℓ denotes a node adjacent to an outer axial boundary such that the local coordinate $\Delta z^{\ell}/2$ denotes the nodal surface which forms part of this boundary. Equation (C.5) is used since, for a zero flux boundary condition, the transverse gradient of the flux evaluated on the surface is identically zero. For the case in which a zero incoming partial current boundary condition is imposed, the transverse gradient is <u>not</u> zero; hence Eq. (C.5) is only approximate, although we expect this approximation to be sufficiently accurate for systems in which the extrapolation length is small. The quadratic expansion coefficients for these surface nodes can be calculated using Eqs. (C.4); the boundary condition given in Eq. (C.5) is satisfied by setting to zero the axial mesh spacing (e.g. Δz^{k+}) and the average hex-plane leakage (e.g. L^{k+}_{gxy}) for "nodes" lying outside the outer reactor boundary.

C.2 Model Problem Study of the Errors Associated with the Leakage Approximations

A simple homogeneous model problem was analyzed in order to assess the effect of the approximations introduced in Eqs. (C.1) and (C.2) on the overall accuracy of the three-dimensional nodal scheme. The model problem consists of a central hexagon surrounded by two full rings of hexagons, with an axial height of 200 cm and a lattice pitch of 20 cm. Zero flux boundary conditions are imposed on all external surfaces. Two-group cross sections typical of a light water reactor were used in the calculations; these cross sections are given in Table C.1.

Table C.1 Two-Group Cross Sections for the Model Problem

Group g	D_g	Σ^r_g	$\nu\Sigma^f_g$	$\Sigma^s_{1\to2}$	χ_g
1	1.5	0.0023	0.0	0.06	1.0
2	0.4	0.2	0.218	--	0.0

Since the solution to this homogeneous problem is separable in the hex-plane and axial directions, i.e.

$$\phi_g^k(x,y,z) \equiv \frac{1}{V^k} \frac{\phi_{gxy}^k(x,y)\ \phi_{gz}^k(z)}{\bar{\phi}_g^k} ,$$

the following exact expressions for the leakage moments are obtained:

$$L_{gzxl}^k \equiv \left[\frac{\bar{L}_{gz}^k}{\bar{\phi}_g^k}\right] \phi_{gxl}^k , \qquad (C.6)$$

$$L_{gxyzl}^k \equiv \left[\frac{\bar{L}_{gxy}^k}{\bar{\phi}_g^k}\right] \phi_{gzl}^k . \qquad (C.7)$$

Thus the differences in the solutions computed using these exact results and the approximations given in Eqs. (C.1) and (C.2) provide a measure of the errors introduced by the leakage approximations.

Table C.2 shows the results of eigenvalue calculations using the indicated approximations to the leakages. All nodal calculations were done using a 20 cm axial mesh spacing. The eigenvalue for calculation number 5 was obtained using Richardson extrapolation of DIF3D finite difference results, and is thus assumed to be the exact solution to the diffusion equation for this problem.

Table C.2 Computed Eigenvalues for the Model Problem

Calculation Number	Approximation to $L_{gz}^k(x,y)$	Approximation to $L_{gxy}^k(z)$	Eigenvalue (k-eff)
1	Flat	Flat	0.96989
2	Flat	Quadratic	0.96935
3	Flat	Exact	0.96934
4	Exact	Quadratic	0.96907
5	(Extrapolated finite difference solution)		0.96842

Table C.3 lists the eigenvalue errors associated with these leakage approximations. The bases for these error estimates are also shown. Note that a flat approximation to $L^k_{gxy}(z)$ [obtained with $\rho^k_{gxy1} \equiv \rho^k_{gxy2} \equiv 0$ in Eq. (C.3)] introduces an error of 0.00055, but this error is essentially eliminated by the use of the quadratic approximation. The total error in the reference nodal calculation [i.e. using Eqs. (C.1) and (C.2)] is 0.00096 relative to the extrapolated finite difference solution. This error thus includes contributions (0.00001 and 0.00028, respectively) due to the quadratic approximation of $L^k_{gxy}(z)$ and the flat approximation of $L^k_{gz}(x,y)$. The difference (0.00067) between the total error and these leakage contributions is due to the remaining hex-plane approximations [specifically, Eqs. (2.33), (2.43), and (2.44)]. (Results not included in in Table C.2 have shown that the error due to the axial polynomial approximation [Eq. (3.29)] is negligable). This difference is consistent with results obtained for the two-dimensional version of this problem.

Table C.3 Error Contributions for the Model Problem

Source of Error	Basis[a]	Error Contribution
Flat Approximation to $L^k_{gxy}(z)$	$k_1 - k_3$	+ 0.00055
Quadratic Approximation to $L^k_{gxy}(z)$	$k_2 - k_3$	+ 0.00001
Flat Approximation to $L^k_{gz}(x,y)$	$k_2 - k_4$	+ 0.00028
All Approximations in Reference Nodal Calculation[b]	$k_2 - k_5$	+ 0.00096

[a] e.g. k_1 is the eigenvalue computed in calculation number 1 of Table C.2.

[b] The reference nodal calculation is calculation number 2 of Table C.2.

The results of this model problem study suggest the following conclusions:

(1) The error associated with the quadratic approximation to $L^k_{gxy}(z)$ is very small relative to the overall error in the nodal calculation. This quadratic approximation leads to a dramatic improvement in accuracy relative to the flat approximation to $L^k_{gxy}(z)$.

(2) The flat approximation to $L^k_{gz}(x,y)$ introduces a significant contribution (0.00028) to the overall error (0.00096) in the nodal calculation. The results confirming the accuracy of the quadratic approximation to $L^k_{gxy}(z)$ suggest that an analogous approximation (discussed in Section 3.6) to $L^k_{gz}(x,y)$ could essentially eliminate this error.

APPENDIX D
CALCULATION OF PEAK POWER DENSITIES

One drawback of the nodal approach is the lack of information concerning the spatial distribution of the flux within the node. This information is required during the edit overlay in order to compute peak power densities and fluxes in each node. A simple procedure is used in the nodal option to compute more accurate peak power densities and fluxes than those obtained by sampling the available node-averaged values. In two dimensions, this procedure involves sampling surface-averaged values on the six surfaces of the k-th node; the surface fluxes are readily obtained from the available interface partial currents:

$$\bar{\phi}_g^k(S_i) = 2\,[J_g^{out,k}(S_i) + J_g^{in,k}(S_i)], \quad i = 1,\ldots,6. \tag{D.1}$$

The notation introduced here differs from that used in Sections 2 and 3. In particular, the six surfaces are numbered beginning with the surface in the positive x-direction and then moving counterclockwise around the hexagon. The surface-averaged values of the power density are

$$\bar{P}^k(S_i) \equiv \sum_{g=1}^{G} PC_g^k\, \bar{\phi}_g^k(S_i), \quad i = 1,\ldots,6, \tag{D.2}$$

where PC_g^k is a power conversion factor. The peak power density in the k-th node is

$$\bar{P}^{k,max} \equiv \max_i \bar{P}^k(S_i), \quad i = 0,\ldots,6, \tag{D.3}$$

where

$$\bar{P}^k(S_0) \equiv \sum_{g=1}^{G} PC_g^k\, \bar{\phi}_g^k . \tag{D.4}$$

An analogous procedure (with $PC_g^k \equiv 1$) is used to compute the peak total fluxes edited by DIF3D.

This procedure is extended to three dimensions by assuming the flux within the node is separable in the hex-plane and axial directions:

$$\phi_g^k(x,y,z) \equiv \bar{\phi}_{gxy}^k(x,y)\ \psi_{gz}^k(z), \tag{D.5}$$

$$\psi_{gz}^k(z) \equiv \frac{\bar{\phi}_{gz}^k(z)}{\bar{\phi}_g^k},$$

where, consistent with the notation in Section 3.2,

$$\bar{\phi}_{gxy}^k(x,y) \equiv \frac{1}{\Delta z^k} \int_{-\Delta z^k/2}^{\Delta z^k/2} dz\ \phi_g^k(x,y,z) \tag{D.6}$$

$$\bar{\phi}_{gz}^k(z) \equiv \frac{\Delta z^k}{V^k} \int_{-h/2}^{h/2} dx \int_{-y_s(x)}^{y_s(x)} dy\ \phi_g^k(x,y,z). \tag{D.7}$$

Using Eq. (D.5) the axial dependence of the hex-plane-averaged flux on the six hex-plane surfaces is given by

$$\phi_g^k(S_i,z) = \bar{\phi}_{gxy}^k(S_i)\ \psi_{gz}^k(z), \tag{D.8}$$

where $\bar{\phi}_{gxy}^k(S_i)$, the surface-averaged fluxes on the six hex-plane surfaces, are computed as in Eq. (D.1). The axial shape function is evaluated using Eq. (3.29):

$$\psi_{gz}^k(z) = 1 + \sum_{n=1}^{N_z} \frac{a_{gzn}^k}{\bar{\phi}_g^k} f_{zn}(z). \tag{D.9}$$

The coefficients a_{gz1}^k, a_{gz2}^k, and a_{gz3}^k are computed using Eqs. (3.30a), (3.30b), and (3.37) respectively. Using Eq. (D.8),

$$P^k(S_i,z) = \sum_{g=1}^{G} PC_g^k \, \bar{\phi}_{gxy}^k(S_i) \, \psi_{gz}^k(z). \qquad (D.10)$$

The peak power density in the k-th node is computed by evaluating Eq. (D.10) at J+1 equally-spaced axial elevations

$$z_j \equiv -\Delta z^k/2 + \frac{j}{J} \Delta z^k, \quad j = 0,\ldots,J, \quad J \equiv 10.$$

The peak density is thus

$$\bar{P}^{k,max} \equiv \max_{i,j} P^k(S_i,z_j), \quad i = 0,\ldots,6, \quad j = 0,\ldots,J, \qquad (D.11)$$

where

$$\bar{P}^k(S_0,z) \equiv \sum_{g=1}^{G} PC_g^k \, \bar{\phi}_g^k \, \psi_{gz}^k(z). \qquad (D.12)$$

As shown by the results presented in Section 5.3, the accuracy of this simple scheme is comparable to that of a fine-mesh finite difference calculation. Sampling the surface-averaged values offers a distinct advantage in two-dimensional fast reactor calculations since the peak values in the inner and radial blankets occur at the core-blanket interface. Adequate accuracy is obtained in the driver fuel regions due to the relatively small dimensions of the hexagonal fuel assemblies. The validity of the separability assumption used in extending this scheme to three dimensions depends upon the degree of heterogeneity in the axial direction. Although it is clear that this approximation will not be very accurate in the vicinity of inserted control rods, it is likely that this assumption will be valid in the region away from control rods and blankets where the driver-fuel peak power density typically occurs. If the computed peak-to-average value in a node is unrealistically high (greater than 5), it is assumed that the separability approximation is not valid, and the peak value in the node is computed by sampling only the node- and surface-averaged values. This "fixup" has been required only for nodes in control assemblies for the test problems studied to date.

APPENDIX E
DESCRIPTION OF THE BCD INPUT FILE A.DIF3D

```
C*****************************************************************************
C                                                                              -
C                        REVISED 1/20/82                                       -
C                                                                              -
CF          A.DIF3D                                                            -
CE          ONE-, TWO-, AND THREE-DIMENSIONAL DIFFUSION THEORY                 -
CE          MODULE-DEPENDENT BCD INPUT                                         -
C                                                                              -
CN                       THIS BCD DATASET MAY BE WRITTEN EITHER               -
CN                       IN FREE FORMAT (UNFORM=A.DIF3D) OR                   -
CN                       ACCORDING TO THE FORMATS SPECIFIED FOR EACH          -
CN                       CARD TYPE (DATASET=A.DIF3D).                         -
CN                                                                            -
CN                       COLUMNS 1-2 MUST CONTAIN THE CARD TYPE NUMBER.       -
CN                                                                            -
CN                       A BLANK OR ZERO FIELD GIVES THE DEFAULT OPTION       -
CN                       INDICATED.                                           -
CN                                                                            -
CN                       NON-DEFAULTED DATA ITEMS ON THE A.DIF3D              -
CN                       DATA SET ALWAYS OVERRIDE THE CORRESPONDING           -
CN                       DATA ON THE RESTART DATA SET DIF3D.                  -
CN                       ENTER -1 TO RESET DATA ON THE RESTART DATA SET       -
CN                       DIF3D BACK TO THEIR DEFAULT VALUES.                  -
C                                                                              -
C*****************************************************************************

C------------------------------------------------------------------------------
CR          PROBLEM TITLE (TYPE 01)                                            -
C                                                                              -
CL    FORMAT-----(I2,4X,11A6)                                                  -
C                                                                              -
CD    COLUMNS          CONTENTS...IMPLICATIONS, IF ANY                         -
CD    =======    ==========================================================   -
CD    1-2        01                                                            -
CD                                                                             -
CD    7-72       ANY ALPHANUMERIC CHARACTERS (1 CARD ONLY).                    -
C                                                                              -
C------------------------------------------------------------------------------

C------------------------------------------------------------------------------
CR          STORAGE AND DUMP SPECIFICATIONS (TYPE 02)                          -
C                                                                              -
CL    FORMAT-----(I2,4X,3I6)                                                   -
C                                                                              -
CD    COLUMNS          CONTENTS...IMPLICATIONS, IF ANY                         -
CD    =======    ==========================================================   -
```

```
CD     1-2        02                                                      -
CD                                                                        -
CD     7-12       POINTR CONTAINER ARRAY SIZE IN FAST CORE MEMORY (FCM)   -
CD                IN REAL*8 WORDS (DEFAULT=10000).                        -
CD                                                                        -
CD     13-18      POINTR CONTAINER ARRAY SIZE IN EXTENDED CORE            -
CD                MEMORY (ECM) IN REAL*8 WORDS (DEFAULT=30000).           -
CD                                                                        -
CD     19-24      POINTR DEBUGGING EDIT.                                  -
CD                0...NO DEBUGGING PRINTOUT (DEFAULT).                    -
CD                1...DEBUGGING DUMP PRINTOUT.                            -
CD                2...DEBUGGING TRACE PRINTOUT.                           -
CD                3...BOTH DUMP AND TRACE PRINTOUT.                       -
C                                                                         -
C-------------------------------------------------------------------------

C-------------------------------------------------------------------------
CR           PROBLEM CONTROL PARAMETERS (TYPE 03)                         -
C                                                                         -
CL     FORMAT-----(I2,4X,11I6)                                            -
C                                                                         -
CD     COLUMNS            CONTENTS...IMPLICATIONS, IF ANY                -
CD     =======    ========================================================-
CD     1-2        03                                                      -
CD                                                                        -
CD     7-12       PROBLEM TYPE.                                           -
CD                0...K-EFFECTIVE PROBLEM (DEFAULT).                      -
CD                1...FIXED SOURCE PROBLEM.                               -
CD                                                                        -
CD     13-18      SOLUTION TYPE.                                          -
CD                0...REAL SOLUTION (DEFAULT).                            -
CD                1...ADJOINT SOLUTION.                                   -
CD                2...BOTH REAL AND ADJOINT SOLUTION.                     -
CD                                                                        -
CD     19-24      CHEBYSHEV ACCELERATION OF OUTER ITERATIONS.             -
CD                0...YES, ACCELERATE THE OUTER ITERATIONS (DEFAULT).     -
CD                1...NO ACCELERATION.                                    -
CD                                                                        -
CD     25-30      MINIMUM PLANE-BLOCK (RECORD) SIZE IN REAL*8 WORDS FOR   -
CD                I/O TRANSFER IN THE CONCURRENT INNER ITERATION          -
CD                STRATEGY. THE DEFAULT (=4500) IS HIGHLY RECOMMENDED.    -
CD                                                                        -
CD     31-36      OUTER ITERATION CONTROL.                                -
CD               -3...BYPASS DIF3D MODULE.                                -
CD               -2...PERFORM NEUTRONICS EDITS ONLY.                      -
CD               -1...PERFORM NEUTRONICS EDITS AND CALCULATE OPTIMUM      -
CD                    OVERRELAXATION FACTORS ONLY.                        -
CD           .GE.0...MAXIMUM NUMBER OF OUTER ITERATIONS (DEFAULT=30).     -
CD                                                                        -
CD     37-42      RESTART FLAG.                                           -
CD                0...THIS IS NOT A RESTART (DEFAULT).                    -
```

```
CD              1...THIS IS A RESTART PROBLEM.                          -
CD                                                                      -
CD      43-48   JOB TIME LIMIT, MAXIMUM (CP AND PP(OR WAIT)) PROCESSOR -
CD              SECONDS (DEFAULT=1000000000).                           -
CD                                                                      -
CD      49-54   NUMBER OF UPSCATTER ITERATIONS PER OUTER ITERATION      -
CD              (DEFAULT=5).  PERTINENT TO UPSCATTER PROBLEMS ONLY.     -
CD                                                                      -
CD      55-60   CONCURRENT ITERATION EFFICIENCY OPTION.                 -
CD              0...PERFORM THE ESTIMATED NO. OF INNER ITERATIONS FOR   -
CD                  EACH GROUP.                                         -
CD              1...AVOID THE LAST PASS OF INNER ITERATIONS IN THOSE    -
CD                  GROUPS FOR WHICH THE NO. OF ITERATIONS IN THE LAST -
CD                  PASS ARE LESS THAN A CODE DEPENDENT THRESHOLD.      -
CD                                                                      -
CD      61-66   ACCELERATION OF OPTIMUM OVERRELAXATION FACTOR           -
CD              CALCULATION.                                            -
CD              0...NO ACCELERATION (DEFAULT).                          -
CD              1...ASYMPTOTIC SOURCE EXTRAPOLATION OF POWER ITERATIONS-
CD                  USED TO ESTIMATE THE SPECTRAL RADIUS OF EACH INNER -
CD                  (WITHIN GROUP) ITERATION MATRIX.                    -
CD      67-72   OPTIMUM OVERRELAXATION FACTOR ESTIMATION ITERATION      -
CD              CONTROL. THE DEFAULT (=50) IS STRONGLY RECOMMENDED.     -
C                                                                       -
CN              THE MAXIMUM NUMBER OF OUTER ITERATIONS SENTINEL         -
CN              SPECIFIES THE NUMBER OF OUTERS THAT CAN BE PERFORMED    -
CN              (COLS. 31-36) EACH TIME THE DIF3D MODULE IS INVOKED.    -
CN                                                                      -
CN              THE DIF3D TERMINATION PROCEDURE WILL ALWAYS:            -
CN                   1...(RE)WRITE THE APPROPRIATE FLUX FILES           -
CN                       (RTFLUX OR ATFLUX).                            -
CN                   2...(RE)WRITE THE RESTART FILE DIF3D.              -
CN              TO FACILITATE AUTOMATIC RESTART, THE RESTART FLAG       -
CN              ON THE DIF3D RESTART CONTROL FILE WILL BE TURNED ON     -
CN              AUTOMATICALLY UPON DETECTION OF:                        -
CN                   1...MAXIMUM NUMBER OF OUTER ITERATIONS.            -
CN                   2...TIME LIMIT.                                    -
CN                                                                      -
CN                                                                      -
CN              TO RESTART THE FLUX CALCULATION:                        -
CN              EITHER                                                  -
CN                                                                      -
CN                  PROVIDE THE RESTART DATA SET DIF3D AND              -
CN                  THE APPROPRIATE FLUX DATA SET (RTFLUX OR ATFLUX)    -
CN                  AND SPECIFY THEM UNDER "BLOCK=OLD" IN THE BCD       -
CN                  INPUT DATA                                          -
CN              OR                                                      -
CN                   1...SET THE RESTART FLAG (COLS. 37-42) TO 1 ON     -
CN                       THE TYPE 03 CARD. THIS PERMITS IMMEDIATE       -
CN                       RESUMPTION OF OUTER ITERATION ACCELERATION.    -
CN                   2...INCLUDE THE LATEST K-EFFECTIVE ESTIMATE        -
CN                       (COLS. 13-24) AND THE DOMINANCE RATIO          -
CN                       ESTIMATE ON THE TYPE 06 CARD (COLS. 61-72).    -
```

```
CN                    3...INCLUDE THE OPTIMUM OVERRELAXATION FACTORS    -
CN                        FOR EACH GROUP (TYPE 07 CARD).                -
CN                    4...PROVIDE THE APPROPRIATE FLUX DATA SET (RTFLUX -
CN                        OR ATFLUX) AND SPECIFY IT UNDER "BLOCK=OLD"   -
CN                        IN THE BCD INPUT DATA.                        -
CN                                                                      -
CN              A NON-ZERO TIME LIMIT (COLS. 43-48) OVERRIDES           -
CN              THE ACTUAL TIME LIMIT DETERMINED INTERNALLY             -
CN              BY SYSTEM ROUTINES IN THE ANL AND LBL PRODUCTION        -
CN              IMPLEMENTATIONS                                         -
CN                                                                      -
CN              THE TIME LIMIT PARAMETER (COLS. 43-48) IS PERTINENT     -
CN              TO EACH ENTRY TO THE DIF3D MODULE.                      -
CN                                                                      -
CN              IT IS RECOMMENDED THAT AN ODD NUMBER OF UPSCATTER       -
CN              ITERATIONS BE SPECIFIED (COLS. 49-54) TO AVOID          -
CN              ADDITIONAL I/O OVERHEAD.                                -
CN                                                                      -
CN              THE USER IS CAUTIONED TO MONITOR THE POINT-WISE         -
CN              FISSION SOURCE CONVERGENCE TO ENSURE THAT MONOTONIC     -
CN              CONVERGENCE IS OBTAINED WHEN THE EFFICIENCY OPTION      -
CN              (COLS. 55-60) IS ACTIVATED.                             -
CN                                                                      -
CN              THE OPTIMUM OVERRELAXATION FACTOR ACCELERATION OPTION   -
CN              IS PRIMARILY INTENDED FOR PROBLEMS KNOWN TO HAVE HIGH   -
CN              (>1.8) OPTIMUM OVERRELAXATION FACTORS.                  -
CN                                                                      -
CN              ITERATION CONTROL (COLS. 67-72) OF THE OPTIMUM          -
CN              OVERRELAXATION FACTOR ESTIMATION IS PRIMARILY INTENDED  -
CN              FOR USE IN CONJUNCTION WITH THE ASYMPTOTIC ACCELERATION-
CN              OPTION (COLS. 61-66).                                   -
C                                                                       -
C-----------------------------------------------------------------------

C-----------------------------------------------------------------------
CR          EDIT OPTIONS (TYPE 04)                                      -
C                                                                       -
CL    FORMAT-----(I2,4X,10I6)                                           -
C                                                                       -
CD    COLUMNS          CONTENTS...IMPLICATIONS, IF ANY                  -
CD    =======  ========================================================-
CD    1-2      04                                                       -
CD                                                                      -
CD    7-12     PROBLEM DESCRIPTION EDIT (IN ADDITION TO USER INPUT      -
CD             SPECIFICATIONS WHICH ARE ALWAYS EDITED.                  -
CD             0...NO EDITS (DEFAULT).                                  -
CD             1...PRINT EDITS.                                         -
CD             2...WRITE EDITS TO AUXILIARY OUTPUT FILE.                -
CD             3...WRITE EDITS TO BOTH PRINT AND AUXILIARY OUTPUT FILE-
CD                                                                      -
CD    13-18    GEOMETRY (REGION TO MESH INTERVAL) MAP EDIT.             -
```

```
CD              0...NO EDITS (DEFAULT).                                  -
CD              1...PRINT EDITS.                                         -
CD              2...WRITE EDITS TO AUXILIARY OUTPUT FILE.                -
CD              3...WRITE EDITS TO BOTH PRINT AND AUXILIARY OUTPUT FILE-
CD                                                                       -
CD    19-24     GEOMETRY (ZONE TO MESH INTERVAL) MAP EDIT.               -
CD              0...NO EDITS (DEFAULT).                                  -
CD              1...PRINT EDITS.                                         -
CD              2...WRITE EDITS TO AUXILIARY OUTPUT FILE.                -
CD              3...WRITE EDITS TO BOTH PRINT AND AUXILIARY OUTPUT FILE-
CD                                                                       -
CD    25-30     MACROSCOPIC CROSS SECTION EDIT.                          -
CD              ENTER TWO DIGIT NUMBER SP WHERE                          -
CD                                                                       -
CD              S CONTROLS THE SCATTERING AND PRINCIPAL CROSS SECTIONS   -
CD              P CONTROLS THE PRINCIPAL CROSS SECTIONS EDIT ONLY.       -
CD                                                                       -
CD              THE INTEGERS S AND P SHOULD BE ASSIGNED ONE OF THE       -
CD              FOLLOWING VALUES (LEADING ZEROES ARE IRRELEVANT).        -
CD              0...NO EDITS (DEFAULT).                                  -
CD              1...PRINT EDITS.                                         -
CD              2...WRITE EDITS TO AUXILIARY OUTPUT FILE.                -
CD              3...WRITE EDITS TO BOTH PRINT AND AUXILIARY OUTPUT FILE-
CD                                                                       -
CD    31-36     BALANCE EDITS                                            -
CD              ENTER 3 DIGIT NUMBER GBR WHERE                           -
CD                                                                       -
CD              G CONTROLS GROUP BALANCE EDITS INTEGRATED OVER THE       -
CD              REACTOR                                                  -
CD              B CONTROLS REGION BALANCE EDIT BY GROUP                  -
CD              R CONTROLS REGION BALANCE EDIT TOTALS                    -
CD                (INCLUDING NET PRODUCTION AND ENERGY MEDIANS)          -
CD                                                                       -
CD              THE INTEGERS G, B, AND R SHOULD BE ASSIGNED ONE OF THE   -
CD              FOLLOWING VALUES (LEADING ZEROES ARE IRRELEVANT)         -
CD              0...NO EDITS (DEFAULT).                                  -
CD              1...PRINT EDITS.                                         -
CD              2...WRITE EDITS TO AUXILIARY OUTPUT FILE.                -
CD              3...WRITE EDITS TO BOTH PRINT AND AUXILIARY OUTPUT FILE-
CD                                                                       -
CD    37-42     POWER EDITS                                              -
CD              ENTER 2 DIGIT NUMBER RM WHERE                            -
CD                                                                       -
CD              R CONTROLS REGION POWER AND AVERAGE POWER DENSITY EDITS-
CD              M CONTROLS POWER DENSITY BY MESH INTERVAL EDIT (PWDINT)-
CD                                                                       -
CD              THE INTEGERS R AND M SHOULD BE ASSIGNED                  -
CD              ONE OF THE FOLLOWING VALUES (LEADING ZEROES ARE          -
CD              IRRELEVANT)                                              -
CD              0...NO EDITS (DEFAULT).                                  -
CD              1...PRINT EDITS.                                         -
CD              2...WRITE EDITS TO AUXILIARY OUTPUT FILE.                -
```

```
CD              3...WRITE EDITS TO BOTH PRINT AND AUXILIARY OUTPUT FILE-
CD                                                                     -
CD    43-48     FLUX EDITS                                             -
CD              ENTER 3 DIGIT INTEGER RMB WHERE                        -
CD                                                                     -
CD              R CONTROLS FLUX EDIT BY REGION AND GROUP               -
CD                INCLUDING GROUP AND REGION TOTALS                    -
CD              M CONTROLS TOTAL (GROUP INTEGRATED) FLUX EDIT          -
CD                BY MESH INTERVAL                                     -
CD              B CONTROLS TOTAL FLUX EDIT BY MESH INTERVAL AND GROUP  -
CD                (RTFLUX OR ATFLUX)                                   -
CD                                                                     -
CD              THE INTEGERS R, M, AND B SHOULD BE ASSIGNED            -
CD              ONE OF THE FOLLOWING VALUES (LEADING ZEROES ARE        -
CD              IRRELEVANT)                                            -
CD              0...NO EDITS (DEFAULT).                                -
CD              1...PRINT EDITS.                                       -
CD              2...WRITE EDITS TO AUXILIARY OUTPUT FILE.              -
CD              3...WRITE EDITS TO BOTH PRINT AND AUXILIARY OUTPUT FILE-
CD                                                                     -
CD    49-54     ZONE AVERAGED (REAL) FLUX EDIT.                        -
CD              0...NO EDITS (DEFAULT).                                -
CD              1...PRINT EDITS.                                       -
CD              2...WRITE EDITS TO AUXILIARY OUTPUT FILE.              -
CD              3...WRITE EDITS TO BOTH PRINT AND AUXILIARY OUTPUT FILE-
CD                                                                     -
CD    55-60     REGION AVERAGED FLUX EDIT.                             -
CD              0...NO EDITS (DEFAULT).                                -
CD              1...PRINT EDITS.                                       -
CD              2...WRITE EDITS TO AUXILIARY OUTPUT FILE.              -
CD              3...WRITE EDITS TO BOTH PRINT AND AUXILIARY OUTPUT FILE-
CD                                                                     -
CD    61-66     STANDARD INTERFACE FILES TO BE WRITTEN IN ADDITION     -
CD              TO RTFLUX AND/OR ATFLUX.                               -
CD              0...NONE (DEFAULT).                                    -
CD              1...WRITE PWDINT.                                      -
CD              2...WRITE RZFLUX.                                      -
CD              3...WRITE BOTH PWDINT AND RZFLUX.                      -
CD                                                                     -
CD    67-72     MASTER DIF3D EDIT SENTINEL DURING CRITICALITY SEARCHES -
CD             -1...SUPPRESS ALL DIF3D EDITS EXCEPT THE ITERATION      -
CD                 HISTORY AND ERROR DIAGNOSTICS                       -
CD              0...EDIT INPUT DATA ON 1ST SEARCH PASS, OUTPUT         -
CD                 INTEGRALS UPON CONVERGENCE OR UPON ACHIEVING THE    -
CD                 MAXIMUM SEARCH PASS LIMIT.                          -
CD              N...ALSO INVOKE SPECIFIED DIF3D EDITS EVERY N-TH       -
CD                 SEARCH PASS.                                        -
C                                                                      -
CN              MULTI-DIGIT EDIT SPECIFICATION EXAMPLES.               -
CN                                                                     -
CN              ENTERING THE INTEGER 201 IN COLUMNS 31-36 YIELDS       -
CN              THE GROUP BALANCE EDIT ON THE AUXILIARY FILE AND       -
```

```
CN              THE REGION BALANCE EDIT ON THE PRIMARY PRINT FILE.      -
CN                                                                      -
CN              ENTERING THE INTEGER 30 IN COLUMNS 31-36 YIELDS         -
CN              THE REGION BALANCE EDIT BY GROUP ON BOTH THE PRINT AND  -
CN              THE AUXILIARY OUTPUT FILES.                             -
C                                                                       -
C-----------------------------------------------------------------------

C-----------------------------------------------------------------------
CR          CONVERGENCE CRITERIA (TYPE 05)                              -
C                                                                       -
CL    FORMAT------(I2,10X,3E12.5)                                       -
C                                                                       -
CD    COLUMNS           CONTENTS...IMPLICATIONS, IF ANY                 -
CD    =======   ===========================================           -
CD    1-2       05                                                      -
CD                                                                      -
CD    13-24     EIGENVALUE CONVERGENCE CRITERION FOR STEADY STATE       -
CD              CALCULATION (DEFAULT VALUE = 1.0E-7 IS RECOMMENDED).    -
CD                                                                      -
CD    25-36     POINTWISE FISSION SOURCE CONVERGENCE CRITERION          -
CD              FOR STEADY STATE SHAPE CALCULATION                      -
CD              (DEFAULT VALUE = 1.0E-5 IS RECOMMENDED).                -
CD                                                                      -
CD    37-48     AVERAGE FISSION SOURCE CONVERGENCE CRITERION            -
CD              FOR STEADY STATE SHAPE CALCULATION                      -
CD              (DEFAULT VALUE = 1.0E-5 IS RECOMMENDED).                -
C                                                                       -
CN              IN UPSCATTERING PROBLEMS IT IS RECOMMENDED THAT         -
CN              THE EIGENVALUE CONVERGENCE CRITERION (COLS. 13-24)      -
CN              BE .1 TIMES THE POINTWISE FISSION SOURCE CONVERGENCE    -
CN              CRITERION (COLS. 25-36).                                -
C                                                                       -
C-----------------------------------------------------------------------

C-----------------------------------------------------------------------
CR          OTHER FLOATING POINT DATA (TYPE 06)                         -
C                                                                       -
CL    FORMAT------(I2,10X,5E12.5)                                       -
C                                                                       -
CD    COLUMNS           CONTENTS...IMPLICATIONS, IF ANY                 -
CD    =======   ===========================================           -
CD    1-2       06                                                      -
CD                                                                      -
CD    13-24     K-EFFECTIVE OF REACTOR (DEFAULT IS OBTAINED FROM        -
CD              THE APPROPRIATE RTFLUX OR ATFLUX FILE, IF PRESENT.      -
CD              OTHERWISE DEFAULT = 1.0).                               -
CD                                                                      -
CD    25-36     ANY POINTWISE FISSION SOURCE WILL BE NEGLECTED IN THE   -
CD              POINTWISE FISSION SOURCE CONVERGENCE TEST IF IT IS       -
```

```
CD              LESS THAN THIS FACTOR TIMES THE R.M.S. FISSION          -
CD              SOURCE (DEFAULT VALUE = .001 IS RECOMMENDED).           -
CD                                                                      -
CD    37-48     ERROR REDUCTION FACTOR TO BE ACHIEVED BY EACH SERIES    -
CD              OF INNER ITERATIONS FOR EACH GROUP DURING A SHAPE       -
CD              CALCULATION - STRONGLY RECOMMENDED THAT THE DEFAULT     -
CD              VALUE OF (.04) BE USED.                                 -
CD                                                                      -
CD    49-60     STEADY STATE REACTOR POWER (WATTS). (DEFAULT = 1.0).    -
CD                                                                      -
CD    61-72     DOMINANCE RATIO (FOR RESTART JOBS ONLY).                -
C                                                                       -
CN              K-EFFECTIVE SPECIFICATIONS (COLS. 13-24):               -
CN                   1...FOR K-EFFECTIVE PROBLEMS, SUPPLY ESTIMATED     -
CN                       K-EFFECTIVE OF REACTOR.                        -
CN                   2...FOR RESTARTED K-EFFECTIVE PROBLEMS, SUPPLY     -
CN                       LATEST K-EFFECTIVE ESTIMATE SUPPLIED ON THE    -
CN                       ITERATION HISTORY EDIT.                        -
CN                   3...FOR SOURCE PROBLEMS, SUPPLY K-EFFECTIVE OF     -
CN                       THE REACTOR.                                   -
CN              DEFAULT IS OBTAINED FROM THE APPROPRIATE RTFLUX OR      -
CN              ATFLUX FILE, IF PRESENT.  OTHERWISE DEFAULT=1.0 .       -
C                                                                       -
CN              NON-MONOTONIC POINTWISE FISSION SOURCE CONVERGENCE      -
CN              IS USUALLY INDICATIVE OF THE NEED TO TIGHTEN THE ERROR  -
CN              REDUCTION FACTOR(COLS. 37-48).  THIS IS FREQUENTLY TRUE-
CN              IN TRIANGULAR GEOMETRY PROBLEMS WHERE A VALUE OF .01 IS-
CN              USUALLY SUFFICIENT TO OBTAIN MONOTONIC CONVERGENCE.     -
C-----------------------------------------------------------------------

C-----------------------------------------------------------------------
CR          OPTIMUM OVERRELAXATION FACTORS (TYPE 07)                    -
C                                                                       -
CL    FORMAT-----(I2,10X,5E12.5)                                        -
C                                                                       -
CD    COLUMNS          CONTENTS...IMPLICATIONS, IF ANY                  -
CD    =======   ========================================================-
CD    1-2       07                                                      -
CD                                                                      -
CD    13-24     OPTIMUM OVERRELAXATION FACTOR FOR GROUP 1.              -
CD                                                                      -
CD    25-36     OPTIMUM OVERRELAXATION FACTOR FOR GROUP 2.              -
CD                                                                      -
CD    37-48     OPTIMUM OVERRELAXATION FACTOR FOR GROUP 3.              -
CD                                                                      -
CD    49-60     OPTIMUM OVERRELAXATION FACTOR FOR GROUP 4.              -
CD                                                                      -
CD    61-72     OPTIMUM OVERRELAXATION FACTOR FOR GROUP 5.              -
C                                                                       -
CN              REPEAT 5 VALUES PER CARD FOR AS MANY TYPE 07 CARDS      -
CN              AS ARE NEEDED.                                          -
```

```
CN              PROBLEM EIGENVALUE WILL BE ESTIMATED. IN THIS CASE, IT -
CN              IS RECOMMENDED TO INCREASE THE NUMBER OF ITERATIONS IN -
CN              COLS. 7-12 TO AT LEAST 10.                            -
C                                                                     -
C---------------------------------------------------------------------

C---------------------------------------------------------------------
CR          SN TRANSPORT OPTIONS (TYPE 09)                            -
C                                                                     -
CL    FORMAT------(I2,4X,2I6,6X,E12.4)                              -
C                                                                     -
CD    COLUMNS           CONTENTS...IMPLICATIONS, IF ANY               -
CD    =======   ===========================================================
CD    1-2       09                                                    -
CD                                                                    -
CD    7-12      SN ORDER.                                             -
CD                                                                    -
CD    13-18     MAXIMUM ALLOWED NUMBER OF LINE SWEEPS PER LINE PER    -
CD              INNER ITERATION (DEFAULT=10).                         -
CD                                                                    -
CD    25-36     LINE SWEEP CONVERGENCE CRITERION (DEFAULT=1.0E-4).    -
C                                                                     -
CN              TO INVOKE THE DIF3D TRANSPORT OPTION, THE TYPE 09 CARD -
CN              MUST BE PRESENT WITH A NONZERO SN ORDER. FOR THE TIME -
CN              BEING, USERS MUST ALSO CONTINUE TO 'PRELIB' TO        -
CN              DATASET 'C116.B99983.MODLIB' TO INVOKE THIS OPTION.   -
C---------------------------------------------------------------------

C---------------------------------------------------------------------
CR          PARAMETERS FOR NODAL HEXAGONAL GEOMETRY OPTION (TYPE 10)  -
C                                                                     -
CL    FORMAT------(I2,4X,5I6)                                       -
C                                                                     -
CD    COLUMNS           CONTENTS...IMPLICATIONS, IF ANY               -
CD    =======   ===========================================================
CD    1-2       10                                                    -
CD                                                                    -
CD    7-12      ORDER OF NODAL APPROXIMATION IN HEX-PLANE.            -
CD              2...NH2 APPROXIMATION.                                -
CD              3...NH3 APPROXIMATION.                                -
CD              4...NH4 APPROXIMATION (DEFAULT).                      -
CD                                                                    -
CD    13-18     ORDER OF NODAL APPROXIMATION IN Z-DIRECTION.          -
CD              2...QUADRATIC APPROXIMATION.                          -
CD              3...CUBIC APPROXIMATION (DEFAULT).                    -
CD                                                                    -
CD    19-24     COARSE-MESH REBALANCE ACCELERATION CONTROL.           -
CD             -1...NO COARSE-MESH REBALANCE ACCELERATION.           -
CD           .GE.0...NUMBER OF COARSE-MESH REBALANCE ITERATIONS PER  -
CD                   OUTER ITERATION (DEFAULT=2).                    -
```

```
CN                                                                      -
CN              THE OPTIMUM OVERRELAXATION FACTORS ARE NORMALLY         -
CN              OBTAINED FROM THE RESTART INSTRUCTIONS PRINTED          -
CN              IMMEDIATELY AFTER THE DIF3D ITERATION HISTORY EDIT.     -
CN              IN THE RESTART INSTRUCTIONS, THE FACTORS ARE ALWAYS     -
CN              EDITTED IN THE --REAL PROBLEM-- ORDERING AND SHOULD BE  -
CN              ENTERED ON THE TYPE 07 CARD --EXACTLY-- AS EDITTED      -
CN              IN THE RESTART INSTRUCTIONS.                            -
CN                                                                      -
CN              THE PERMISSIBLE FACTOR RANGE IS BOUNDED BY 1.0 AND 2.0  -
CN              INCLUSIVE. A ZERO OR BLANK FACTOR ENTRY DEFAULTS        -
CN              TO 1.0. FACTORS ARE COMPUTED FOR THOSE GROUPS HAVING    -
CN              A FACTOR OF 1.0; FACTORS GREATER THAN 1.0 ARE NOT       -
CN              RECOMPUTED.                                             -
CN                                                                      -
CN              TYPE 07 CARDS ARE PRIMARILY INTENDED FOR RESTART JOBS   -
CN              ONLY (STRONGLY RECOMMENDED).                            -
C                                                                       -
C-----------------------  ---------------------------------------------

C-----------------------------------------------------------------------
CR          NEAR CRITICAL SOURCE PROBLEM ASYMPTOTIC EXTRAPOLATION       -
CR          PARAMETERS (TYPE 08)                                        -
C                                                                       -
CC          ***** WARNING...SELECT THIS OPTION ONLY IF THE  *****       -
CC          ***** ASYMPTOTIC EXTRAPOLATION IS REQUIRED FOR  *****       -
CC          ***** THIS PROBLEM.                            *****       -
C                                                                       -
CL    FORMAT-----(I2,4X,I6,E12.5)                                       -
C                                                                       -
CD    COLUMNS           CONTENTS...IMPLICATIONS, IF ANY                 -
CD    =======   ========================================================-
CD    1-2       08                                                      -
CD                                                                      -
CD    7-12      NUMBER OF OUTER (POWER) ITERATIONS PERFORMED PRIOR TO   -
CD              ASYMPTOTIC EXTRAPOLATION OF NEAR CRITICAL SOURCE        -
CD              PROBLEM (DEFAULT=5).                                    -
CD                                                                      -
CD    13-24     EIGENVALUE OF THE HOMOGENEOUS PROBLEM CORRESPONDING     -
CD              TO THE NEAR CRITICAL SOURCE PROBLEM. THIS EIGENVALUE    -
CD              MUST BE LESS THAN ONE.                                  -
CD                                                                      -
CD    25-30     INITIAL FLUX GUESS SENTINEL.                            -
CD              0...FLAT FLUX GUESS=1.0 (DEFAULT)                       -
CD              1...FLAT FLUX GUESS=0.0                                 -
C                                                                       -
CN              THE TYPE 08 CARD IS REQUIRED TO ACTIVATE AN ALTERNATE   -
CN              SPECIAL ACCELERATION SCHEME FOR NEAR CRITICAL           -
CN              SOURCE PROBLEMS.                                        -
CN                                                                      -
CN              IF COLS. 13-24 ARE ZERO OR BLANK, THE HOMOGENEOUS       -
```

```
CD     25-30      ASYMPTOTIC SOURCE EXTRAPOLATION OF OUTER ITERATIONS.   -
CD                0...APPLY ASYMPTOTIC SOURCE EXTRAPOLATION TO OUTER     -
CD                    ITERATIONS (DEFAULT).                              -
CD                1...NO ASYMPTOTIC SOURCE EXTRAPOLATION.                -
CD                                                                       -
CD     31-36      NUMBER OF AXIAL PARTIAL CURRENT SWEEPS PER GROUP       -
CD                PER OUTER ITERATION (DEFAULT=2).                       -
C                                                                        -
CN                THE TYPE 10 CARD IS PERTINENT ONLY WHEN THE NODAL      -
CN                HEXAGONAL GEOMETRY OPTION (A.NIP3 TYPE 03 CARD         -
CN                GEOMETRY-TYPE SENTINEL VALUES BETWEEN 110 AND 128)     -
CN                IS SPECIFIED.                                          -
CN                                                                       -
CN                IT IS RECOMMENDED THAT THE DEFAULT VALUES FOR THE      -
CN                ORDER OF THE NODAL APPROXIMATION IN THE HEX-PLANE       -
CN                (COLS. 7-12) AND FOR THE ORDER OF THE NODAL APPROXI-    -
CN                MATION IN THE Z-DIRECTION (COLS. 13-18) BE SPECIFIED.   -
C                                                                        -
C--------------------------------------------------------------------------

C--------------------------------------------------------------------------
CR          AXIAL COARSE-MESH REBALANCE BOUNDARIES FOR NODAL             -
CR          HEXAGONAL GEOMETRY OPTION (TYPE 11)                          -
C                                                                        -
CL     FORMAT-----(I2,10X,3(I6,E12.5))                                   -
C                                                                        -
CD     COLUMNS          CONTENTS...IMPLICATIONS, IF ANY                  -
CD     =======    ========================================================-
CD     1-2        11                                                     -
CD                                                                       -
CD     13-18      NUMBER OF AXIAL COARSE-MESH REBALANCE INTERVALS.       -
CD                                                                       -
CD     19-30      UPPER Z-COORDINATE.                                    -
CD                                                                       -
CD     31-36      NUMBER OF AXIAL COARSE-MESH REBALANCE INTERVALS.       -
CD                                                                       -
CD     37-48      UPPER Z-COORDINATE.                                    -
CD                                                                       -
CD     49-54      NUMBER OF AXIAL COARSE-MESH REBALANCE INTERVALS.       -
CD                                                                       -
CD     55-66      UPPER Z-COORDINATE.                                    -
C                                                                        -
CN                THE TYPE 11 CARD IS PERTINENT ONLY WHEN THE THREE-     -
CN                DIMENSIONAL NODAL HEXAGONAL GEOMETRY OPTION (A.NIP3    -
CN                TYPE 03 CARD GEOMETRY-TYPE SENTINEL VALUES BETWEEN     -
CN                120 AND 128) IS SPECIFIED.                             -
CN                                                                       -
CN                IF NO TYPE 11 CARDS ARE PRESENT, THE AXIAL COARSE-MESH -
CN                REBALANCE INTERVALS ARE DEFINED BY THE Z-COORDINATE    -
CN                VALUES SPECIFIED ON A.NIP3 CARD 09.                    -
CN                                                                       -
CN                BOUNDARIES ARE SPECIFIED VIA NUMBER PAIRS.             -
```

```
CN              EACH NUMBER PAIR IS OF THE FORM (N(I), Z(I)). THERE    -
CN              ARE N(I) AXIAL COARSE-MESH REBALANCE INTERVALS BETWEEN -
CN              Z(I-1) AND Z(I), WHERE Z(0) IS THE LOWER REACTOR       -
CN              BOUNDARY IN THE Z-DIRECTION. NUMBER PAIRS MUST BE      -
CN              GIVEN IN ORDER OF INCREASING MESH COORDINATES. ALL     -
CN              AXIAL COARSE-MESH REBALANCE BOUNDARIES MUST COINCIDE   -
CN              WITH THE MESH LINES WHICH BOUND MESH INTERVALS.        -
C-------------------------------------------------------------------------
CEOF
```

APPENDIX F
DESCRIPTION OF SELECTED CARD TYPES IN THE BCD INPUT FILE A.NIP3

```
C*****************************************************************-
C                                                                 -
C                      PREPARED 8/28/75 AT ANL                    -
C                      LAST REVISED 03/25/82                      -
C                                                                 -
CF          A.NIP3                                                -
CE          NEUTRONICS MODEL INPUT FOR CODES WHICH REQUIRE CCCC    -
CE          INTERFACE FILES                                       -
C                                                                 -
CN                     THIS BCD DATA SET MAY BE WRITTEN EITHER     -
CN                     IN FREE FORMAT (UNFORM=A.NIP3) OR ACCORDING TO -
CN                     THE FORMATS SPECIFIED FOR EACH CARD TYPE    -
CN                     (DATASET=A.NIP3).                          -
CN                                                                -
CN                     COLUMNS 1-2 MUST CONTAIN THE CARD TYPE     -
CN                     NUMBER.                                    -
CN                                                                -
CN                     UNLESS OTHERWISE STATED, BLANKS ARE NOT    -
CN                     MEANINGFUL IN A6 LABEL FIELDS.             -
C                                                                 -
C                                                                 -
CN                 ***  CARD TYPE DIRECTORY  ***                  -
CN                                                                -
CN     TYPE                       CONTENTS                        -
CN     ====    ==================================================  -
CN      01     PROBLEM TITLE                                      -
CN      02     INPUT PROCESSING SPECIFICATIONS                    -
CN      03     PROBLEM GEOMETRY                                   -
CN      04     EXTERNAL BOUNDARY CONDITIONS                       -
CN      05     EXTERNAL BOUNDARY CONDITION CONSTANTS              -
CN      06     REGION BOUNDARIES FOR ORTHOGONAL GEOMETRIES        -
CN      07     AREA SPECIFICATIONS                                -
CN      09     VARIABLE-MESH STRUCTURE                            -
CN      10     INTERNAL BLACK ABSORBER CONDITIONS                 -
CN      11     INTERNAL BLACK ABSORBER CONDITION CONSTANTS        -
CN      12     FINITE-GEOMETRY TRANSVERSE DISTANCES               -
CN      13     MATERIAL SPECIFICATIONS                            -
CN      14     COMPOSITION (ZONE) SPECIFICATIONS                  -
CN      15     REGION/COMPOSITION CORRESPONDENCE                  -
CN      19     REGION OR MESH DISTRIBUTED INHOMOGENEOUS SOURCE    -
CN      21     SEARCH EDIT OPTIONS AND CONVERGENCE CRITERIA       -
CN      22     SEARCH PARAMETER DATA                              -
CN      23     CONCENTRATION MODIFIERS FOR CRITICALITY SEARCH     -
CN      24     MESH MODIFIERS FOR CRITICALITY SEARCH              -
CN      25     BUCKLING MODIFIERS FOR CRITICALITY SEARCH          -
CN      26     ALPHA MODIFIERS FOR CRITICALITY SEARCH             -
CN      29     HEXAGON DIMENSION                                  -
CN      30     REGION DEFINITIONS FOR ARRAYS OF HEXAGONS          -
```

```
CN      31      BACKGROUND REGION FOR ARRAYS OF HEXAGONS                -
CN      34      COMPOSITION- AND GROUP-DEPENDENT BUCKLINGS               -
CN      35      DIRECTIONAL DIFFUSION COEF. SCHEME                       -
CN      36      DIRECTIONAL DIFFUSION COEF./COMPOSITION CORRESPONDENCE   -
CN      37      FISSION ENERGY CONVERSION FACTORS                        -
CN      38      CAPTURE ENERGY CONVERSION FACTORS                        -
CN      39      NUCLIDE SET ASSIGNMENTS                                  -
CN      40      SOURCE EDIT, SYNTHESIS TRIAL FUNCTION SOURCE             -
CN      41      NATURAL DECAY INHOMOGENEOUS SOURCE                       -
CN      42      SOURCE SPECTRA                                           -
CN      43      GRAPHICS OUTPUT CONTROL                                  -
C                                                                        -
C************************************************************************-
                                                                         -
                                                                         -
C------------------------------------------------------------------------
CR          PROBLEM GEOMETRY SPECIFICATION (TYPE 03)                     -
C                                                                        -
CL    FORMAT-----(I2,10X,I6)                                             -
C                                                                        -
CD    COLUMNS           CONTENTS...IMPLICATIONS, IF ANY.                 -
CD    =======   ========================================================-
CD    1-2       03                                                       -
CD                                                                       -
CD    13-18     GEOMETRY TYPE.                                           -
CD              10...SLAB                                                -
CD              20...CYLINDER                                            -
CD              30...SPHERE                                              -
CD              40...X-Y                                                 -
CD              44...X-Y-Z                                               -
CD              50...R-Z                                                 -
CD              60...R-THETA                                             -
CD              62...R-THETA-Z                                           -
CD              64...THETA-R                                             -
CD              66...THETA-R-Z                                           -
CD              70...TRIANGULAR, RHOMBIC BOUNDARY, CORE CENTER AT        -
CD                   60 DEGREE ANGLE (SIXTH CORE SYMMETRY).              -
CD              72...TRIANGULAR, RECTANGULAR BOUNDARY, HALF CORE         -
CD                   SYMMETRY.                                           -
CD              74...TRIANGULAR, RHOMBIC BOUNDARY, CORE CENTER AT        -
CD                   120 DEGREE ANGLE (THIRD CORE SYMMETRY).             -
CD              76...TRIANGULAR, 60 DEGREE TRIANGULAR BOUNDARY,          -
CD                   SIXTH CORE SYMMETRY.                                -
CD              78...TRIANGULAR, RECTANGULAR BOUNDARY, QUARTER           -
CD                   CORE SYMMETRY.                                      -
CD              80...TRIANGULAR, RECTANGULAR BOUNDARY, FULL CORE.        -
CD              90...TRIANGULAR-Z, RHOMBIC BOUNDARY IN PLANE, CORE       -
CD                   CENTER LINE AT 60 DEGREE ANGLE.                     -
CD              92...TRIANGULAR-Z, RECTANGULAR BOUNDARY IN PLANE,        -
CD                   HALF CORE SYMMETRY IN PLANE.                        -
CD              94...TRIANGULAR-Z, RHOMBIC BOUNDARY IN PLANE, CORE       -
CD                   CENTER LINE AT 120 DEGREE ANGLE.                    -
```

```
CD              96...TRIANGULAR-Z, 60 DEGREE TRIANGULAR BOUNDARY       -
CD                   IN PLANE.                                         -
CD              98...TRIANGULAR-Z, RECTANGULAR BOUNDARY IN PLANE,      -
CD                   QUARTER CORE SYMMETRY IN PLANE.                   -
CD             100...TRIANGULAR-Z, RECTANGULAR BOUNDARY IN PLANE,      -
CD                   FULL CORE IN PLANE.                               -
CD             110...HEXAGONAL, FULL CORE.                             -
CD             114...HEXAGONAL, SIXTH CORE SYMMETRY.                   -
CD             116...HEXAGONAL, THIRD CORE SYMMETRY.                   -
CD             120...HEXAGONAL-Z, FULL CORE IN PLANE.                  -
CD             124...HEXAGONAL-Z, SIXTH CORE SYMMETRY IN PLANE.        -
CD             126...HEXAGONAL-Z, THIRD CORE SYMMETRY IN PLANE.        -
CD                                                                     -
C                                                                      -
CN              THE HEXAGONAL AND HEXAGONAL-Z GEOMETRY OPTIONS MAY     -
CN              NOT BE AVAILABLE IN ALL VERSIONS OF DIF3D.             -
C                                                                      -
C-----------------------------------------------------------------------
                                                                       -
                                                                       -
C-----------------------------------------------------------------------
CR          EXTERNAL BOUNDARY CONDITIONS (TYPE 04)                     -
C                                                                      -
CL    FORMAT-----(I2,10X,616)                                          -
C                                                                      -
CD    COLUMNS          CONTENTS...IMPLICATIONS, IF ANY                 -
CD    =======  ========================================================-
CD    1-2      04                                                      -
CD                                                                     -
CD    13-18    BOUNDARY CONDITION AT LOWER "X" BOUNDARY OF REACTOR.    -
CD                                                                     -
CD    19-24    BOUNDARY CONDITION AT UPPER "X" BOUNDARY OF REACTOR.    -
CD                                                                     -
CD    25-30    BOUNDARY CONDITION AT LOWER "Y" BOUNDARY OF REACTOR.    -
CD                                                                     -
CD    31-36    BOUNDARY CONDITION AT UPPER "Y" BOUNDARY OF REACTOR.    -
CD                                                                     -
CD    37-42    BOUNDARY CONDITION AT LOWER Z BOUNDARY OF REACTOR.      -
CD                                                                     -
CD    43-48    BOUNDARY CONDITION AT UPPER Z BOUNDARY OF REACTOR.      -
CD                                                                     -
CD                                                                     -
CD             2...PHI=0.                                              -
CD             3...PHI PRIME=0.                                        -
CD             4...D * PHI PRIME + A * PHI = 0.                        -
CD             6...REPEATING (PERIODIC) WITH OPPOSITE FACE.            -
CD             7...REPEATING (PERIODIC) WITH NEXT ADJACENT BOUNDARY    -
CD                 (SEE DISCUSSION BELOW).                             -
CD             8...INVERTED REPEATING ALONG THIS FACE                  -
CD                 (180 DEGREE ROTATION).                              -
CD             9...INCOMING ANGULAR FLUX ZERO (TRANSPORT ONLY).        -
CD             10..REFLECTIVE (TRANSPORT ONLY).                        -
```

```
CD              11..PERIODIC (TRANSPORT ONLY).                          -
CD              12..WHITE (TRANSPORT ONLY).                             -
CD                                                                      -
C                                                                       -
CN              PHI PRIME IS THE DERIVATIVE OF THE FLUX IN THE          -
CN              DIRECTION OF THE REACTOR OUTWARD NORMAL. D IS THE       -
CN              DIFFUSION COEFFICIENT IN THE MESH INTERVAL              -
CN              IMMEDIATELY INSIDE THE REACTOR BOUNDARY. IF COLS.       -
CN              43-48 ARE 4 AND NO TYPE 05 CARD IS SUPPLIED TO SPECIFY -
CN              THE CONSTANT A, THE VALUE 0.46920 WILL BE USED BY       -
CN              DEFAULT.                                                -
CN                                                                      -
CN              CONDITIONS 2-8 APPLY TO DIFFUSION THEORY PROBLEMS,      -
CN              AND 9-12 APPLY TO TRANSPORT THEORY PROBLEMS.            -
CN                                                                      -
CN              "X" REPRESENTS THE FIRST DIMENSION COORDINATE (X IN     -
CN              X-Y GEOMETRY, R IN R-Z, ETC.). "Y" REPRESENTS THE       -
CN              SECOND DIMENSION COORDINATE (Y IN X-Y GEOMETRY, Z IN    -
CN              R-Z, ETC.). WHEN THE MODEL IS THREE-DIMENSIONAL, THE    -
CN              THIRD DIMENSION IS ALWAYS Z.                            -
CN                                                                      -
CN              REPEATING CONDITIONS (6,7,8) ARE ONLY APPLICABLE TO     -
CN              THE FIRST TWO DIMENSIONS.                               -
CN                                                                      -
CN              NOTE FOR REPEATING CONDITION 7.  LET XL DENOTE THE      -
CN              LOWER "X" BOUNDARY, XU DENOTE THE UPPER "X" BOUNDARY,   -
CN              YL DENOTE THE LOWER "Y" BOUNDARY AND YU DENOTE THE      -
CN              UPPER Y BOUNDARY.  FOR REPEATING BOUNDARY CONDITIONS    -
CN              (CONDITION 7), THE SEQUENCE OF BOUNDARIES IMPLIED BY    -
CN              THE TERM "NEXT ADJACENT BOUNDARY" IS XL, YL, XU, YU.    -
CN              OF THE TWO BOUNDARIES INVOLVED, THE ONE APPEARING       -
CN              FIRST IN THE SEQUENCE IS ASSIGNED THE BOUNDARY          -
CN              CONDITION (7), THE SECOND IS IGNORED.  FOR EXAMPLE,     -
CN              IF XL AND YL ARE THE PERIODIC BOUNDARIES, COLS. 13-18   -
CN              MUST CONTAIN A 7, COLS. 25-30 WILL BE IGNORED.          -
C                                                                       -
C-----------------------------------------------------------------------
                                                                        -
                                                                        -
C-----------------------------------------------------------------------
CR          VARIABLE-MESH STRUCTURE (TYPE 09)                           -
C                                                                       -
CL    FORMAT-----(I2,9X,A1,3(I6,E12.5))                                 -
C                                                                       -
CD    COLUMNS           CONTENTS...IMPLICATIONS, IF ANY                 -
CD    =======   ===========================================================
CD    1-2       09                                                      -
CD                                                                      -
CD    12        COORDINATE DIRECTION.                                   -
CD              X..."X" COORDINATE DIRECTION.                           -
CD              Y..."Y" COORDINATE DIRECTION.                           -
CD              Z...Z-COORDINATE DIRECTION.                             -
```

```
CD                                                                      -
CD    13-18     NUMBER OF INTERVALS.                                    -
CD                                                                      -
CD    19-30     UPPER COORDINATE.                                       -
CD                                                                      -
CD    31-36     NUMBER OF INTERVALS.                                    -
CD                                                                      -
CD    37-48     UPPER COORDINATE.                                       -
CD                                                                      -
CD    49-54     NUMBER OF INTERVALS.                                    -
CD                                                                      -
CD    55-66     UPPER COORDINATE.                                       -
C                                                                       -
CN              NOTE THAT A Z IN COL. 12 IS PERTINENT ONLY IF THE       -
CN              GEOMETRY IS THREE-DIMENSIONAL.                          -
CN                                                                      -
CN              "X" REPRESENTS THE FIRST DIMENSION COORDINATE (X IN     -
CN              X-Y GEOMETRY, R IN R-Z, ETC.). "Y" REPRESENTS THE       -
CN              SECOND DIMENSION COORDINATE (Y IN X-Y GEOMETRY, Z IN    -
CN              R-Z, ETC.). WHEN THE MODEL IS THREE-DIMENSIONAL, THE    -
CN              THIRD DIMENSION IS ALWAYS Z.                            -
C                                                                       -
CN              IN GEOMETRIES INVOLVING AN ANGULAR DIMENSION (THETA)    -
CN              THE ANGULAR VARIABLE MUST BE GIVEN IN RADIANS.          -
CN                                                                      -
CN              EACH NUMBER PAIR IS OF THE FORM (N(I), X(I)). THERE     -
CN              ARE N(I) INTERVALS BETWEEN X(I-1) AND X(I), WHERE X(0)  -
CN              IS THE LOWER REACTOR BOUNDARY IN THIS DIRECTION.        -
CN              NUMBER PAIRS MUST BE GIVEN IN ORDER OF INCREASING       -
CN              MESH COORDINATES. ALL REGION BOUNDARIES MUST COINCIDE   -
CN              WITH THE MESH LINES THAT BOUND MESH INTERVALS.          -
C                                                                       -
C-----------------------------------------------------------------------
                                                                        -
                                                                        -
C-----------------------------------------------------------------------
CR          LOCATIONS OF REGIONS FOR TRIANGULAR, TRIANGULAR-Z,          -
CR          HEXAGONAL, AND HEXAGONAL-Z GEOMETRIES (TYPE 30)             -
C                                                                       -
CL    FORMAT-----(I2,4X,A6,3I6,2E12.5)                                  -
C                                                                       -
CD    COLUMNS          CONTENTS...IMPLICATIONS, IF ANY                  -
CD    =======  ========================================================-
CD    1-2      30                                                       -
CD                                                                      -
CD    7-12     REGION LABEL (REPEATED ON ADDITIONAL TYPE 30 CARDS).     -
CD                                                                      -
CD    13-18    HEXAGONAL RING NUMBER WHERE REGION IS LOCATED.           -
CD                                                                      -
CD    19-24    STARTING HEXAGON POSITION FOR THIS REGION.               -
CD                                                                      -
CD    25-30    FINAL HEXAGON POSITION FOR THIS REGION.                  -
```

```
CD                                                                      -
CD    31-42     LOWER Z BOUNDARY OF REGION.                             -
CD                                                                      -
CD    43-54     UPPER Z BOUNDARY OF REGION.                             -
CD                                                                      -
C                                                                       -
CN              REGION LABELS MUST BE NON-BLANK.                        -
CN                                                                      -
CN              IF THE STARTING POSITION (COLS. 19-24) IS BLANK OR      -
CN              ZERO, THE REGION LABEL IS ASSIGNED TO THE WHOLE RING.   -
CN                                                                      -
CN              IF THE FINAL POSITION (COLS. 25-30) IS BLANK OR ZERO,   -
CN              THE REGION LABEL IS ASSIGNED TO THE POSITION IN 19-24   -
CN              OF THE RING IN 13-18.                                   -
CN                                                                      -
CN              DATA ON THIS CARD MAY BE OVERLAYED. THAT IS, REGION     -
CN              ASSIGNMENTS DEFINED ON LATER TYPE 30 CARDS SUPERCEDE    -
CN              DATA FOR RINGS AND POSITIONS PREVIOUSLY SPECIFIED.      -
CN                                                                      -
CN              THE REGION LOWER AND UPPER Z BOUNDARIES MUST COINCIDE   -
CN              WITH MESH LINES, WHICH BOUND MESH INTERVALS.            -
CN                                                                      -
CN              THE FIGURE BELOW ILLUSTRATES THE ORDER OF NAMING        -
CN              RINGS AND HEXAGONS IN THE RINGS.  THE FIRST NUMBER OF   -
CN              EACH NUMBERED PAIR IS THE RING NUMBER, AND THE SECOND   -
CN              NUMBER IS THE HEXAGON NUMBER IN THAT RING.              -
CN              THE REGION OF SOLUTION DEPENDS ON THE VALUE IN COLS.    -
CN              13-18 ON CARD TYPE 03 AS FOLLOWS.                       -
CN                                                                      -
CN        COLS. 13-18 ON CARD TYPE 03      REGION OF SOLUTION           -
CN        ===========================      ==========================   -
CN                  80                     ENTIRE FIGURE AS SHOWN BELOW -
CN                  72                     IN THE 180 DEGREE SECTOR A-B -
CN                  78                     IN THE 90 DEGREE SECTOR A-C  -
CN                  70                     IN THE 60 DEGREE SECTOR A-D  -
CN                  74                     IN THE 120 DEGREE SECTOR A-E -
CN                 110                     ENTIRE FIGURE AS SHOWN BELOW -
CN                 114                     IN THE 60 DEGREE SECTOR F-C  -
CN                 116                     IN THE 120 DEGREE SECTOR F-G -
```

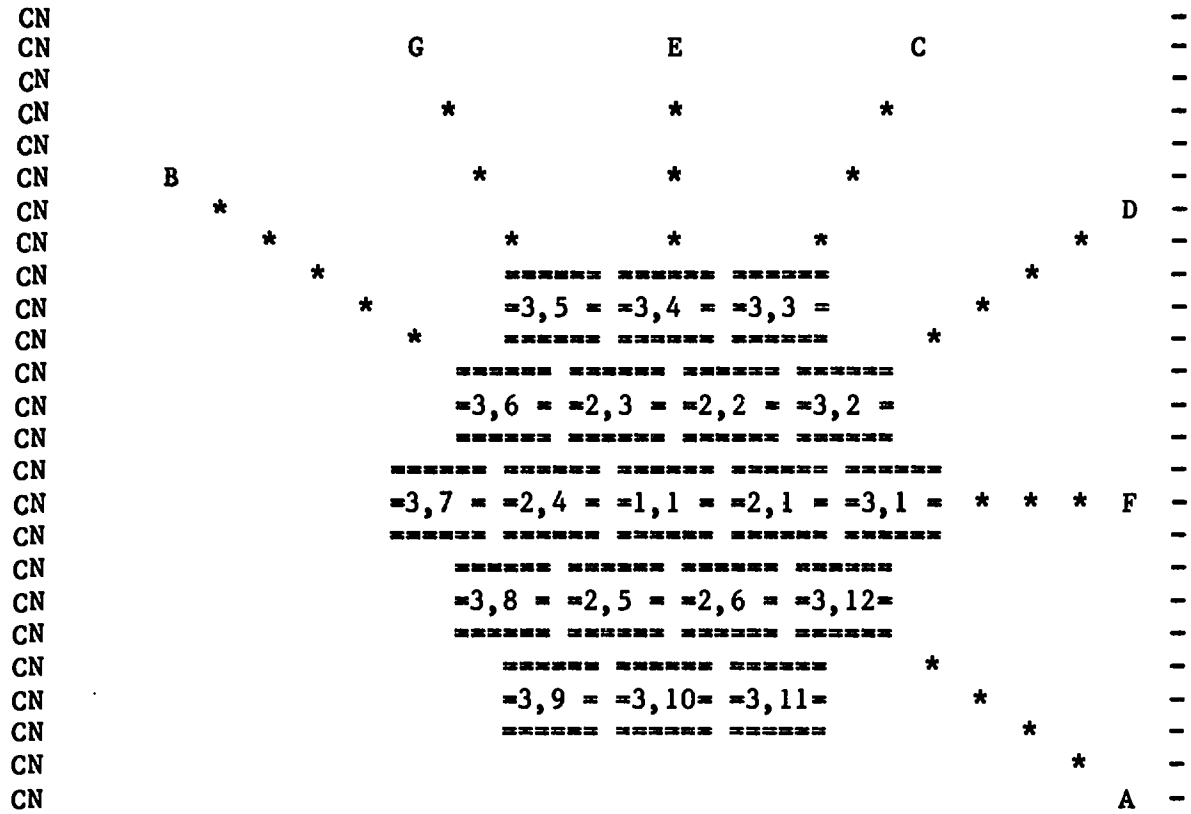

CN ALTHOUGH THE REGIONS OF SOLUTION DIFFER FOR THE TRIANGULAR AND HEXAGONAL GEOMETRY MODELS, TYPE 30 CARDS COMPOSED FOR TRIANGULAR GEOMETRY MODELS CAN ALSO BE USED FOR HEXAGONAL GEOMETRY MODELS.

C

C----------

C----------

CR BACKGROUND REGION NAME FOR TRIANGULAR, TRIANGULAR-Z, HEXAGONAL, AND HEXAGONAL-Z GEOMETRIES (TYPE 31)

C

CL FORMAT-----(I2,4X,A6)

C

CD	COLUMNS	CONTENTS...IMPLICATIONS, IF ANY
CD	1-2	31
CD	7-12	BACKGROUND REGION NAME.

C

CN ANY PORTION OF THE REACTOR NOT SPECIFIED ON THE TYPE 30 CARDS WILL BE IN THE BACKGROUND REGION.

CN

CN IF THE BACKGROUND REGION NAME (COLS. 7-12) IS BLANK,

```
CN              OR IF THERE IS NO TYPE 31 CARD, THE BACKGROUND REGION  -
CN              WILL BE ASSIGNED A REGION NUMBER 0 (ZERO).  NOTE THAT  -
CN              SOME CCCC CODES EXCLUDE SUCH A REGION FROM THE REGION  -
CN              OF SOLUTION, WHILE OTHER CCCC CODES MAY NOT ALLOW       -
CN              ZERO REGION NUMBERS.                                   -
C                                                                      -
C-----------------------------------------------------------------------
```

Distribution for ANL-83-1

Internal:

P. B. Abramson
C. H. Adams
P. I. Amundson
C. L. Beck
E. S. Beckjord
J. C. Beitel
S. K. Bhattacharyya
R. N. Blomquist
M. M. Bretscher
H. Bigelow
S. B. Brumbach
R. G. Bucher
J. E. Cahalan
S. G. Carpenter
B. R. Chandler
Y. I. Chang
P. J. Collins
R. J. Cornella
D. C. Cutforth
T. A. Daly
J. R. Deen
K. L. Derstine
D. R. Ferguson
K. E. Freese
E. K. Fujita
P. J. Garner
J. M. Gasidlo
E. M. Gelbard
G. M. Greenman
G. L. Grasseschi
H. Henryson
H. H. Hummel
R. N. Hwang
R. E. Kaiser
Kalimullah
H. Khalil
R. D. Lawrence (5)
W. K. Lehto
R. M. Lell
L. G. LeSage
J. R. Liaw
M. J. Lineberry
D. J. Malloy
J. E. Matos
H. F. McFarlane
R. D. McKnight
D. Meneghetti
A. Olson
Y. Orechwa
E. M. Pennington
P. J. Persiani
P. A. Pizzica
R. B. Pond
J. R. Ross
R. R. Rudolph
G. K. Rusch
R. W. Schaefer
D. M. Smith
K. S. Smith
J. L. Snelgrove
C. G. Stenberg
W. J. Sturm
S. F. Su
C. E. Till
B. J. Toppel
A. Travelli
R. B. Turski
A. J. Ulrich
R. Vilim
D. C. Wade
D. P. Weber
T. Y. Wei
W. L. Woodruff
S. T. Yang
B. S. Yarlagadda
ANL Patent Dept.
ANL Contract File
ANL Libraries (2)
TIS Files (6)
AP Division Files (10)

External:

DOE-TIC, for distribution per UC-79d (122)
Manager, Chicago Operations Office, DOE
Director, Technology Management, DOE-CH
Director, DOE-RRT (2)
Applied Physics Division Review Committee:
- P. W. Dickson, Jr., Clinch River Breeder Reactor Project, Oak Ridge
- K. D. Lathrop, Los Alamos National Laboratory
- D. A. Meneley, Ontario Hydro
- J. E. Meyer, Massachusetts Inst. Technology
- R. Sher, Stanford U.
- D. B. Wehmeyer, Detroit Edison
- A. E. Wilson, Idaho State U.

H. Alter, Office of Breeder Technology, DOE
Advanced Reactor Library, Westinghouse Electric Co., Madison, Pa
M. Becker, Rensselaer Polytechnic Inst.
R. A. Bennett, Westinghouse Hanford Co.

C. Cowan, General Electric Co., Sunnyvale
Fast Breeder Dept. Library, General Electric Co., Sunnyvale
H. L. Dodds, Technology for Energy Corp., Knoxville
R. Doncals, Westinghouse Electric Corp., Madison, Pa
J. J. Dorning, University of Illinois, Urbana
M. J. Driscoll, MIT
C. Durston, Combustion Engineering, Windsor
R. Ehrlich, General Electric Co., San Jose
H. Farrar IV, Atomics International, Canoga Park
G. F. Flanagan, Oak Ridge National Laboratory
N. M. Greene, Oak Ridge National Laboratory
D. R. Harris, Rensselaer Polytechnic Inst.
P. B. Hemmig, Reactor Research and Development, DOE
A. F. Henry, MIT
J. Kallfelz, Georgia Institute of Technology
R. Karam, Georgia Institute of Technology
W. Y. Kato, Brookhaven National Laboratory
R. J. LaBauve, Los Alamos National Laboratory
J. Lewellen, Reactor Research and Development, DOE
E. Lewis, Northwestern University
M. D. Libby, NUSCO, Hartford, CT
D. R. McCoy, Los Alamos National Laboratory
F. C. Maienschein, Oak Ridge National Laboratory
D. R. Mathews, GA Technologies, San Diego
R. MacFarlane, Los Alamos National Laboratory
H. A. Morowitz, Tarzana, CA
J. Naser, Electric Power Research Inst., Palo Alto
National Energy Software Center, ANL (10)
R. J. Neuhold, Reactor Research and Development, DOE
R. D. O'Dell, Los Alamos National Laboratory
D. Okrent, University of California, Los Angeles
K. Ott, Purdue University
O. Ozer, Electric Power Research Inst., Palo Alto
A. M. Perry, Oak Ridge National Laboratory
J. Prabulos, Combustion Engineering, Windsor
Radiation Shielding Information Center, ORNL (10)
A. B. Reynolds, University of Virginia
P. Rose, Brookhaven National Laboratory
D. H. Roy, Babcock and Wilcox Co., Lynchburg, Va
R. Schenter, Westinghouse Hanford Co.
P. Soran, Los Alamos National Laboratory
E. R. Specht, Atomics International, Canoga Park
S. Stewart, General Electric, Co., Sunnyvale
L. E. Strawbridge, Westinghouse Electric Corp., Madison, Pa
R. J. Tuttle, Atomics International, Canoga Park
D. R. Vondy, Oak Ridge National Laboratory
C. Weisben, Oak Ridge National Laboratory